Monte Carlo study of the dosimetry of small-photon beams using CMOS active pixel sensors

Francisco Jiménez Spang

A Thesis submitted to University College London

for the degree of

Doctor of Philosophy

Department of Medical Physics and Bioengineering

University College London, UCL

2011

I, Francisco Jiménez Spang, confirm that the work presented in this thesis is my own. Where information has been derived from other sources, I confirm that this has been indicated in the thesis.

_____

Abstract

Stereotactic radiosurgery is an increasingly common treatment modality that uses very small photon fields. This technique imposes high dosimetric standards and complexities that remain unsolved. In this work the dosimetric performance of CMOS active pixel sensors is presented for the measurement of small-photons beams. A novel CMOS active pixel sensor called Vanilla developed for scientific applications was used. The detector is an array of 520×520 pixels on a 25 μm pitch which allows up to six dynamically reconfigurable regions of interest (ROI) down to 6×6 pixels. Full frame readout of over 100 frame/s and a ROI frame rate of over 20000 frame/s are available. Dosimetric parameters measured with this sensor were compared with data collected with ionization chambers, film detectors and GEANT4 Monte Carlo simulations. The sensor performance for the measurement of cross-beam profiles was evaluated for field sizes of 0.5×0.5 cm^2. The high spatial resolution achieved with this sensor allowed the accurate measurement of profiles from one single row of pixels. The problem of volume averaging is solved by the high spatial resolution provided by the sensor allowing for accurate measurements of beam penumbrae and field size under lateral electronic disequilibrium. Film width and penumbrae agreed within 2.1% and 1.8%, respectively, with film measurement and better than 1.0% with Monte Carlo calculations. Agreements with ionization chambers better than 1.0% were obtained when measuring tissue-phantom ratios. The data obtained from this imaging sensor can be easily analyzed to extract dosimetric information. The results presented in this work are promising for the development and implementation of CMOS active pixel sensors for dosimetry applications.

Contents

Acknowledgements

List of Figures

List of Tables

Chapter 1

Introduction

1.1 Background and Motivation

State-of-the-art dosimetry techniques in radiation therapy have made it possible the treatment of tumours and diseases with high precision. Such techniques have allowed physicists the possibility to irradiate irregular-shaped tumours tightly while limiting the amount of radiation given to adjacent organs. The trade-off between the maximum dose delivered to a tumour without compromising surrounding organs and the outcome of a treatment can be understood from dose-response relationships in radiobiology, which is closely related to accurate dose delivery and consequently dose measurement (Brahme 1984).

According to the IAEA (2000) the combined standard uncertainty in the determination of absorbed dose to water under reference conditions is estimated to be typically about 1.5% (1 SD). This uncertainty is the result of the calibration of the dosimeter at the standards laboratory (combined uncertainty of 0.6%) and the uncertainty introduced by a measurement procedure carried out in the user's beam (uncertainty of 1.4%). This indicates that the overall accuracy to determine the absorbed dose could be significantly improved if the uncertainty of dose measurements carried out in the user's beam could be reduced. An accurate estimation of the absorbed dose distribution in the target volume is necessary to establish the dose-response relationship for malignant and normal tissues for a given radiation modality (Brahme 1984) and its uniform and precise dose delivery is of paramount importance for accurate radiation therapy.

Radiation therapy treatments with small photon fields were first developed for

treating small intracranial lesions in the late 1940. This development gave rise to what today is known as stereotactic radiosurgery (SRS) and radiotherapy (SRT). SRS was originally thought of as a means of minimally invasive brain surgery and was later expanded with the aid of digital imaging to include extracerebral and intracranial targets. SRS aims at the radionecrosis of the target by delivering a precise high radiation dose in a single fraction. SRT in contrast (an extension of SRS to treat small tumours in other anatomical locations) is based on dose fractionation to preserve the function of normal cells and reduce toxicity. In both procedures, the target size is very small (< 4 cm) in comparison to those treated in conventional radiotherapy.
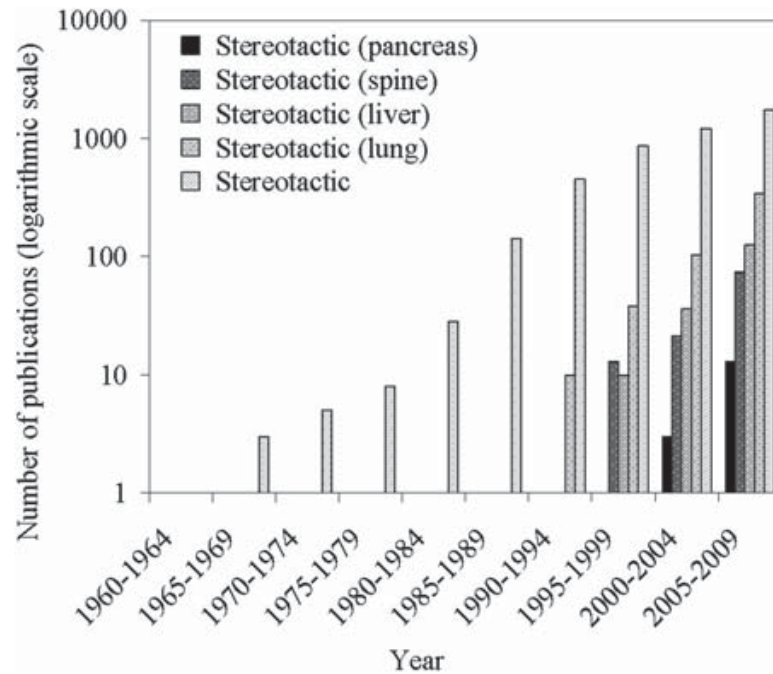
Figure 1.1: An indication (based on a PubMed search of published literature) of the increasing implementation of both intra- and extra-cranial stereotactic radiotherapy. Note the logarithmic scale (Taylor *et al.* 2010).

SRS was primarily developed for the treatment of benign lesions as inoperable arteriovenous malformations (AVMs), acoustic tumours, pituitary adenomas (Pike *et al.* 1987, Podgorsak *et al.* 1988, Chan 1996) and then extended to metastatic tumours and other intracranial lesions by employing stereotactic apparatus and multiple small beams delivered through noncoplanar isocentric arcs. Figure 1.1 shows the exponential increase of published papers in this field, which provides evidence of the increasing number of small-field treatments worldwide.

As treatment techniques SRS and SRT rely on a high degree of precision localization and dose measurement accuracy to allow for the delivery of a high target dose with significantly lower dose to brain tissue. As a consequence of the high amount of energy that requires to be concentrated in a small volume steep dose gradients are created in the radiation field. As a result, positioning accuracy and beam delivery have to be considered carefully. To achieve maximal spatial accuracy in radiosurgical planning, advanced imaging techniques are required. Accuracy better than 1 mm is required (Khan 2003). This imposes stringent limits to the spatial resolution of any detector used for the dosimetry of the small fields involved in SRS and SRT. This dosimetry is commonly known as small-field dosimetry.

1.1.1   Accuracy in SRS and SRT

SRS and SRT involve two steps: (1) the first step requires head immobilization as well as the accurate localization and delineation of the shape of the lesion and the neuroanatomy in the reference frame of a stereotactic frame system with available imaging modalities as CT, MRI, angiography, PET; and (2) the delivery of the planned dose. The aim of the treatment is the production of a concentrated dose in the lesion and a steep dose gradient in the surrounding tissue. The dose fall-off from the edge of the treatment volume provides a dramatic sparing of healthy tissue.

Geometric accuracy of target localization is determined by the imaging modality. CT provides an accuracy of 1.3 ± 0.5 mm, while the localization accuracy achieved with MRI is lower (Khan 2003). Linear accelerator set-up uncertainty is usually 1.0 mm. The achievable uncertainty in SRS for a 1-mm CT slice thickness is 2.4 mm (TG-42 1995).

Dose calculation in treatment planning is also limited by the accuracy with which doses are measured during commissioning. Accurate knowledge of the dosimetry of the small fields involved in SRS and SRT treatments is extremely necessary. In particular, there are three quantities of interest in SRS which limit the use of detectors for small-field dosimetry, which are discussed in the next section.

17

1.1.2 The difficulty of small field measurements

The delivery of accurate treatments using small fields requires precise and accurate measurements of dose profiles, percent depth dose curves (tissue phantom ratios, TPR, or tissue maximum ratio, TMR) and output factors. These parameters are necessary for input into the clinical planning systems. The measurement of these quantities poses difficulties due to:

1. a lack of lateral electronic equilibrium which introduces perturbations in the electron fluence in the medium of measurement;

2. uncertainties when measuring the field width and the penumbra of cross-beam profiles;

3. detector volume averaging.

Ionization chambers are not suitable for small beam profiles (Das *et al.* 2000) and their use requires corrections to account for detector size effect through convolution kernels (García-Vicente *et al.* 2000). Volume averaging occurs when the sensitive volume of the detector is either not completely covered by the radiation beam or because the detector is so large that a significant dose variation across the detector is produced. This results in an underestimation of dose (Duggan and Coffey 1998, Johns and Darby 1950, Sibata *et al.* 1991, Metcalfe *et al.* 1992, Chang *et al.* 1996, García-Vicente *et al.* 2000 and Laub and Wong 2003). The algorithms used to compute dose in radiation therapy treatment plans often assume electronic equilibrium. This assumption can result in severe miscalculations of dose distributions, particularly in the vicinity of inhomogeneities in small fields (Fu *et al.* 2004).

To overcome these difficulties dosimeters with high spatial resolution, small sensitive volumes, tissue equivalence, high sensitivity, dose rate and energy independence and fast acquisition readout are required. Even though ionization chambers are the gold standard for radiation dosimetry, they do not meet all these requirements and present practical difficulties for small fields (Alfonso *et al.* 2008). The dosimetry of small photon fields is therefore performed with a combination of detectors and methods to fulfill the requirements of each application (Allison *et al.* 2006). Some authors have used Monte Carlo calculations

to validate dosimetric data measured using different techniques in radiosurgery (Al-Najjar *et al.* 1998). These authors found that even measurements performed using small ionization chambers of 0.02 cm^3 were affected by lateral electronic disequilibrium and steep dose gradients.

An extensive review of the literature relevant to the use of small-photon beams in radiation therapy shows that:

(a) There is a potential risk for detriment and radiation toxicity dependent on dose and the irradiated volume (Blomgren *et al.* 1995).

(b) Treatments with small fields as SRS/SRT are associated to potential side-effects as neurological impairment to death (Flickinger *et al.* 1995, Jensen *et al.* 2005), children experience cognitive decline after radiotherapy of brain tumours (Roman and Sperduto 1995).

(c) Dose delivery margins are of the order of millimetres (Khan 2003).

(d) Small-field measurements present difficulties and therefore the implementation of small-field treatments is limited, volume averaging effect and lateral electronic disequilibrium introduces significant errors in dose measurement.

(e) The dosimetry of small fields is not fully implemented mainly because the reference conditions recommended by conventional codes of practice cannot be established in some treatment machines and because absorbed dose to water is not standardized for such fields (Alfonso *et al.* 2008).

(f) Ionization chamber dosimetry of small fields is limited due to a volume averaging effect (Laub and Wong 2003).

(g) Additionally, detectors such as diodes present significant limitations which cause absorbed dose perturbation (Beddar *et al.* 1994).

It is evident that the dosimetry of small fields imposes complexities that are well understood for conventional treatments. The accuracy of dose delivery is limited by the available dosimeters which have potential limitations when measuring small fields. Conventional methods cannot be accurately applied to the

characterization of such fields, which can lead to complications for the patient. Therefore, the objective of the present work is to investigate the potential of the performance of CMOS active pixel sensors for dosimetric measurements of small fields through experimental and Monte Carlo methods. This is investigated in detail by characterizing the detector for the measurement of dosimetric parameters and by using the Monte Carlo modelled detector to validate this data and calculate the sensor response.

1.1.3 Hypothesis of this work

The aim of this thesis is to prove the following hypothesis:

CMOS active pixel sensors have the potential to overcome the limitations of current detectors to measure dosimetric parameters of small-photon beams accurately.

1.1.4 Justification of the hypothesis

Previous works by Perucha *et al.* (2003) which aimed to use Monte Carlo simulations to support dosimetric data showed that for small fields the photon energy variation across the radiation field is negligible. This was also suggested by others (Kubsad *et al.* 1990, Robar *et al.* 1999). From these works it is deduced that the perturbation introduced by a thin silicon detector in the photon and electron spectra in the radiation field could be considered small.

Despite diode detectors being made of silicon it has been demonstrated that they are useful dosimeters, when calibrated properly, for small-field measurements. Their high sensitivity compared to ionization chambers, their small size and high spatial resolution make them suitable detectors for beam data measurements in stereotactic radiosurgery (McKerracher and Thwaites 1999). CMOS active pixel sensors have the advantage of small size as diodes have, but with the additional capability to image a beam in two dimensions. Their small sensitive volume and pixelated architecture provide single elements sensitive to ionizing radiation. Additionally, they offer interesting capabilities to integrate signal processing within the pixel, enabling data processing during image acquisition, which sets one of the most significant differences with other imaging technologies (e.g. CCDs). Radiation tolerance of deep-submicron CMOS process, high spatial resolution,

high-speed imaging and region of interest capabilities (ROI) make CMOS sensors attractive detectors for dosimetry in which high performance is required.

There is an increasing interest in developing CMOS APS for scientific applications. CMOS APS sensors have recently attracted interest in medical physics, particularly for medical imaging applications (Bohndiek *et al.* 2008, Allinson *et al.* 2009, Cabello *et al.* 2007) as well as for charged particles tracking (Kleinfelder *et al.* 2006). This has motivated the present work to investigate the clinical application of CMOS APS for the dosimetry of small-photons fields, a still incomplete problem in radiation dosimetry. The advantages of the high spatial resolution achieved with imaging sensors for the measurement of cross-beam profiles of 0.5 $\times$ 0.5 cm^2 is investigated. The application of this sensor is extended to the measurement of output factors and tissue-phantom ratios.

The search for a suitable dosimeter for small field measurements is becoming increasingly difficult and dependent on the recent improvements to deliver the dose with higher accuracy. New challenges are arising from the application of radiation therapy at smaller fields: IMRT, Gamma Knife and CyberKnife are only some techniques that challenge the current state-of-the-art dosimetry (Das *et al.* 2007). While these new techniques are demanding the use of complex and advanced dosimetry systems, the selection of a suitable dosimeter is given by the requirements associated to the delivery technique and the current technology. Therefore, new developments in dosimetry should be based on a technology with increasing improvement in terms of performance, functional capability and flexibility.

1.2 Structure of this thesis

In this chapter, the motivation for this work has been stated as well as the hypothesis to be proven and its justifications. The rest of the thesis is structured as follows:

(i) Chapter 2 explains in depth the challenges in small field dosimetry and presents a review of the state of the art of detector systems available for the measurement of small photon beam.

(ii) Chapter 3 describes the main features and characteristics of CMOS APS and how to evaluate their performance.

(iii) Chapter 4 gives a short introduction of the Monte Carlo method, the main features of the GEANT4 code and issues present in the simulation of radiation transport. The Monte Carlos simulation of the CMOS sensor used in this work is carried out.

(iv) Chapter 5 presents the investigation of the energy response of CMOS sensors to MV and kV energies experimentally and by using the Monte Carlo method.

(v) Chapter 6 presents results of the experimental and Monte Carlo validation of the phase-space files used as input beams for the Monte Carlo simulations in this work.

(vi) Chapter 7 presents the results of the performance of the CMOS sensor to measure the dosimetric parameters required in small-field dosimetry.

(vii) Chapter 8 summarizes the contribution of this work as well as the future research.

Chapter 2

State-of-the-art small field dosimetry

2.1 Overview of chapter

In this chapter a brief overview of state-of-the-art small field dosimetry is presented. The approach followed in this chapter consisted of describing some of the most relevant detectors currently used for the dosimetry of small fields. The main features and drawbacks of each detector system is described in detail within the context of small fields as well as the major ideas underlying their applications. Critical analysis is not considered in the present chapter, this is treated in further chapters.

2.2 Radiation dosimeters

A radiation dosimeter is a device that measures either directly or indirectly dosimetric quantities such as exposure, kerma and absorbed dose. These quantities arise from the interaction of a radiation field in a medium (e.g. particle fluence, energy fluence, etc.).

The fundamental quantity of radiation dosimetry is the energy imparted (ICRU 1980) which is defined in a given volume and is a stochastic quantity. The absorbed dose is a nonstochastic quantity defined as the expected value of the energy imparted per unit mass of the medium for infinitesimal volumes (Carlsson 1981). In a more formal language, the absorbed dose is defined from

$$D = \frac{1}{\rho} \lim_{V \to 0} \frac{\bar{\epsilon}}{V} = \frac{1}{\rho} \lim_{V \to 0} \frac{(\bar{R}_{in} - \bar{R}_{out} + \overline{\Sigma Q})}{V}, \qquad (2.1)$$

where ρ is the density of the medium, $\bar{\epsilon}$ is the imparted energy in a infinitesimal volume V, $\bar{R}_{in}$ and $\bar{R}_{out}$ are the expectation values of the radiant energies incident on and emerging from V, respectively, and the term $\overline{\Sigma Q}$ is the net release of rest mass energy of nuclei and elementary particles occurring within V.

This formal definition of absorbed dose, which can also be derived from a more rigorous formalism using transport theory (Carlsson 1985) has practical difficulties in its implications. It follows from this definition that to measure dose experimentally the volume of a detector should, in principle, be considered as infinitesimally small, but because the number of interactions and the mass in a small volume are also stochastic quantities it is possible and completely valid to extend the limit in equation 4.1 to zero as long as expectation values are taken (Carlsson 1981). Therefore, in practical situations the volume to calculate the absorbed dose in equation 4.1 is small relative to changes of the radiation field and sufficiently large to make negligible the statistical uncertainties arising from a finite number of interactions taking place in the volume.

2.3 Detector requirements in radiation therapy

When a detector is exposed to a radiation field the signal produced in its sensitive volume can be correlated to the energy imparted in it (hereafter energy imparted will be called energy deposited which is a term of more common use in the literature). This signal may take different forms, for instance, temperature rise in a calorimeter or number of electrons created in an ionization chamber or solid state detector. The detector is then calibrated and its readings are valid for a particular radiation field and range of energies.

External radiation therapy dosimetry mainly requires two tasks: beam characterization and the determination of the dose in the patient. Both are highly important and require instruments capable of accurately measuring and characterizing the radiation beam. Exact knowledge of both the absorbed dose to water at a point and its spatial distribution, as well as the possibility of deriving the dose

to an organ in the patient are the main requirements in dosimetry (Chen 2007). In addition, it is desirable for a detector to have a composition equivalent to the medium where the absorbed dose is intended to be measured. When a detector material is not equivalent to that of the medium it is said that a perturbation is introduced in the medium. Such perturbation is associated to the radiation field in the medium, namely, the photon or electron fluence (Nahum 1996).

External radiation therapy demands basic requirements for dosimetry. This encompasses type of radiation, and the energy range in which the dosimeter will be applied. The list presented below gives different application domains in which dosimetry is of interest (Barthe 2001):

- Good knowledge of radiation nature and beam quality.

- Dose rate: a few gray per minute. Total integrated dose: < 60 Gy.

- Contact therapy: X-rays: 50 kV to 300 kV.

- Cobalt therapy: γ rays ≈ 1.25 MeV.

- X-ray therapy: X-rays from 4 MV to 25 MV (Bremsstrahlung spectrum).

- Electron therapy: electrons: 6 MeV to 20 MeV.

- Neutron therapy: neutrons: 20 MeV to 60 MeV.

- Boron neutron capture therapy (BNCT): thermal and epithermal neutrons: 25 MeV to a few keV.

- Proton therapy: protons: 30 to 200 MeV.

Specific requirements regarding the performance of a dosimeter have to be evaluated to study its feasibility for a particular implementation. For radiation therapy, and particularly in small-field dosimetry, dosimeters require high levels of accuracy and precision as well as the following characteristics:

- Dose-rate response independence.

- Energy response independence.

- Angular independence.

- High spatial resolution.

- High dynamic range.

- Linearity.

- Tissue equivalence.

- Good sensitivity.

Most detectors do not meet all these requirements. Nevertheless, in practice, this limitation is tackled by finding the most suitable detector for a particular application.

2.4 Challenges in small field dosimetry

In addition to the requirements mentioned in section 2.3, small-field dosimetry imposes dosimetric challenges which are not present in treatment fields from 4 $\times$ 4 cm^2 up to 40 $\times$ 40 cm^2. Larger treatment errors than those present in conventional treatments (larger field sizes) have been reported (Alfonso *et al.* 2008). These errors arise because the physical conditions established in radiation therapy dosimetry with conventional fields are not met when the treatment fields are smaller than 4 $\times$ 4 cm^2. Ionization chambers, which are the gold standard in radiation therapy dosimetry are not suitable for dosimetric measurements at these small fields. High dose gradients, volume averaging, lack of charged particle equilibrium, perturbation of the particle fluence and the effect of the radiation source size are some of the problems to be overcome when small fields are used. These issues will be discussed in the following sections.

2.4.1 Steep gradient of the radiation field

Treatment techniques such as intensity-modulated radiation therapy (IMRT) and stereotactic radiotherapy and radiosurgery (SRT/SRS) use very small beams. In particular SRT and SRS are specific techniques used to treat intracranial targets which are inaccessible with surgeries (Lutz *et al.* 1988, Bellerive *et al.* 1998 and Sims *et al.* 1999). Well collimated beams allow the delivery of high dose to a tumour in a single fraction (SRS). To achieve high conformation of the planned dose to the planning target volume (PTV) it is necessary to produce steep dose gradients to kill cancerous cells and preserve as much as possible the surrounding healthy tissue. Close to the edge of the field or within the penumbral region the

dose gradient is very high. The accuracy with which the absorbed dose has to be known in this region is crucial. Accurate dose profile measurement is, therefore, of great importance to accomplish the aim of the treatment. This challenge puts a limit on the accuracy of a detector and demands high spatial resolution.

2.4.2 Volume averaging

Volume averaging occurs when the dimensions of a detector are too large in comparison to the radiation field. If the dose changes significantly over the detector's sensitive volume the measurement of cross-beam profiles is artificially flattened (Dugan and Coffey 1998). Broadening of the penumbra of beam profiles is also a reported issue (Pappas *et al.* 2008, Sibata *et al.* 1990, and Metcalfe *et al.* 1993). When this happens the reading of a detector is averaged over its entire sensitive volume while only part of it is irradiated (García-Vicente *et al.* 2000). Beam modelling in treatment planning systems (TPS) requires accurate beam profile measurements for the calculation of treatment dose (Bedford *et al.* 2003, Laub and Wong 2002, Duggan and Coffey 1998 and Al-Najjar *et al.* 1998). One of the common approaches to tackle this problem is the modelling of the convolution kernel of the detector which allows the correction of the detector response (García-Vicente *et al.* 2000 and García-Vicente *et al.* 1997). However, the availability of small detectors with high spatial resolution is desirable. The clinical consequence is a larger margin of irradiation of healthy tissue close to the target volume and miscalculation of dose volume histograms and tumour control and normal tissue complication probabilities (García-Vicente *et al.* 2005).

2.4.3 Lack of charged particle equilibrium

When charged particle equilibrium (CPE) exists in a volume, the calculation of absorbed dose is significantly simplified. Its importance in radiation dosimetry lies in the fact that under CPE the dose may be related to the collision part of kerma in any medium (Attix 1983). Lack of lateral charged particle equilibrium is an issue in small-field dosimetry. Its effect on dose measurement has been widely discussed in the literature (Nizin and Chang 1991, Heydarian *et al.* 1996, Duggan and Coffey 1998, Verhaegen *et al.* 1998, Carrasco *et al.* 2004, Alfonso *et al.* 2008, Mesbahi 2008 and Das *et al.* 2008). Lateral electronic disequilibrium

arises when the lateral range of secondary particles (electrons) is comparable or greater to the radius of the field size. When a detector is placed in a radiation field, it is found that the dose deposited in its sensitive volume is not the result of an equally balanced dose by electrons from opposite sides in the lateral direction. Under this situation perturbation factors calculated at reference conditions are not accurate for the conversion from ionization to dose to water based on cavity theory (Sánchez-Doblado *et al.* 2003). The clinical implications of a lack of LCPE is that the predictions of delivered dose to the PTV are unreliable, which is significantly pronounced in low density media such as lung (Fu *et al.* 2004).

2.4.4 Beam alignment

Stereotactic radiosurgery is used to irradiate intracanial lesions as small as 2 mm in diameter. The dose delivered for such treatments can reach 80 Gy (Urgošík *et al.* 2000). TPS relies on measured beam data either for beam calculation or beam modelling (Paskalev *et al.* 2003). The accuracy of this data depends upon the correct beam alignment achieved at the linac's isocentre. Misalignments in linear-accelerator-based radiosurgery can arise due to focal spot displacement, asymmetry of collimator jaws and displacement in the collimator rotation axis or in the gantry rotation axis (Khan 2009). The spatial accuracy required is said to be better than 1 mm for stereotactic treatments. Although, accuracy as good as 0.2 ± 0.1 has been achieved (Gibbs *et al.* 1991). The consequences of a small misalignment can cause severe errors in dose calculation. Paskalev *et al.* (2003) found that a 0.2 mm misalignment caused a 5% variation in measured dose. Therefore, dosimeters with high spatial resolution are required when small fields are involved.

2.4.5 Partial occlusion of the radiation source

Partial occlusion of the radiation source occurs when the collimator aperture of a linear accelerator decreases to a size close or smaller than the focal spot as seen from the point of measurement. From the point of measurement at the isocentre position only a part of the source is seen. The radiation output of the linear accelerator will then be lower than that at larger fields. As a consequence, the output factor will drop abruptly for very small field sizes. This is produced

because as the field becomes smaller and partially blocked, the primary beam coming from the target is reduced and less in proportion to larger fields (Das *et al.* 2008). Focal spot sizes are difficult to measure accurately, but Monte Carlo phase-space files modelling where the focal spot FWHM is assumed between 1 to 1.5 mm usually produces accurate results for percentage depth dose (PDD) and beam profiles in water (Wang and Leszczynski 2007). To avoid dose calculation errors when modelling linear accelerators an accurate simulation of the extended source (focal spot) is of great importance (Sauer and Wilbert 2007, Sham *et al.* 2008 and Scot *et al.* 2009).

2.5   Current approaches in small field dosimetry

The difficulties in the implementation of treatments using small fields arise mainly from the little knowledge about the characteristics of the radiation field and the limited accuracy achievable with current detectors. Therefore, over the last few years research has been focused on advances in detectors, beam modelling and Monte Carlo simulations (Taylor *et al.* 2011, Eklund and Ahnesjö 2010, and Das *et al.* 2008). This section will review the current dosimeters and techniques used for the measurement of small-photon fields and the different approaches to overcome the limitations described above.

2.5.1   Ionization chambers

Although the use of ionization chambers is well established in radiation therapy dosimetry due to their excellent dose response, dose rate and energy independence and the extensive research behind them, their application in small-field dosimetry is limited and should be carefully examined.

Ionization chambers are sometimes limited for small-field measurements. Lack of LCPE is a concern when measuring cross-beam profiles in the penumbra region. This has been studied by Sibata *et al.* (1991). Their work concluded that detector size effect and lack of lateral electronic equilibrium affect profiles measured with ionization chambers, which is more significant in the presence of small fields where the stopping power ratio changes with depth (Andreo and Brahme 1986, Heydarian *et al.* 1996, Verhaegen *et al.* 1998, Sánchez-Doblado *et*

al. 2003). Metcalfe *et al.* (1992) also studied detector size effect in the penumbra region. They found that lack of LCPE broadens the beam penumbra. This effect is more pronounced when there are media with different densities such as air, in which the electron range is larger than the range in water. González-Castaño *et al.* (2007) studied the response of three ionization chambers with active volumes between 0.6 and 0.015 cm^3. Their work showed that even the smallest chamber used presented under-response at very small fields (1.16 cm square field size) and that this under-response increases with the active volume. A broader penumbra has implications in treatment plans resulting in unnecessary irradiation of healthy tissues close to the planning target volume (García-Vicente *et al.* 2005). An earlier study by McKerracher and Thwaites (1999) revealed that although PDD curves could be accurately measured with Markus, Farmer and PinPoint ionization chambers, profile measurements were not accurate in the penumbra region using the PinPoint chamber. Therefore, they recommended the use of three or more small detectors and their comparisons for accurate measurements in small fields. Another study showed that PinPoint ionization chambers are limited to fields greater than 2 cm and over respond to low energy Compton scattered photons (Martens *et al.* 2000). All these investigations suggested that ionization chambers are not well suited for small-field measurements.

2.5.2 Thermoluminescent dosimeters

Thermoluminescent dosimeters (TLDs) are widely used for the dosimetry of ionizing radiation. In radiation therapy TLDs are used for dose measurement in total skin irradiation (Weaver *et al.* 1995), in total body irradiation (Hussein *et al.* 1996), as well as in verification of dose delivery (Fergional *et al.* 1997). Due to their small size TLDs can be used to measure dose directly inserted into tissues and body cavities (Engström *et al.* 2005). A detailed clinical application of TLDs is given by Kron (1999). A theoretical review of the basis of TL dosimetry has been presented by Horowitz (1981).

Although TL dosimetry has some advantage in radiation therapy dosimetry due to the small size and nearly water equivalence, TL dosimetry is time consuming. The reading of TL detectors may be affected if nitrogen is present during

thermal reading, especially for radiation doses below 10 cGy (Meigooni *et al.* 1995). Sensitivity depends upon the characteristics of the TLD and the reader system (Yu and Luxton 1999). LiF over responds to low energy photons by about 40% (Muench *et al.* 1991). Reproducibility is considered poor, typically $\pm$ 2% (Ruden and Bengtsson 1977), although Yu and Luxton (1999) have reported a mean standard deviation from a batch of TLD rods equal to 1.1%. These factors may limit the use of TLD in small-field dosimetry.

2.5.3 Radiographic and radiochromic film

Film dosimetry is a well established technique to measure dose distribution in phantoms, dose characterization and verification. Film dosimetry for megavoltage photon-beam dosimetry is a challenge because film sensitivity varies with spectral variation in phantom as a function of field size and depth. Film response also depends on beam direction (Dutreix and Dutreix 1969), processing conditions, and densitometer used (Haus 2001, Pai *et al.* 2007). X-OMAT V and the EDR2 films (Kodak, Rochester, NY) are widely used in clinical applications. X-OMAT V has been used for relative dose distribution measurements for IMRT (Tsai, J.-S. *et al.* 1998). Its main limitation is energy dependence response and the limited dose range for IMRT application (Zhu *et al.* 2002). Kodak EDR2 film shows less sensitivity with depth and field size in comparison to X-OMAT film (Zhu *et al.* 2002), but reproducibility has been reported within $\pm$ 3 to 5%. The agreement obtained between these two types of film and ionization chambers to measured PDDs suggests no significant energy dependence for a 6 MV beam and field size 5×5 cm^2 (up to about 20 cm deep). In stereotactic radiosurgery film has been recommended for profile measurements (TG-42 1995). Paskalev *et al.* (2003) used the EDR2 film to measure dose distribution for 1.5 and 3 mm collimators. They found good agreement with Monte Carlo simulation of profiles. Sibata *et al.* (1991) also found good agreement between profile measurements with film and other detectors, which contradicts works suggesting film are not well suited for profile measurements because of changes in photon spectra (Williamson *et al.* 1981). However, the use of silver-halide radiographic film remains difficult for accurate dosimetry because of large differences in sensitivity to photon energies

in the l0-200 keV region (Niroomand-Rad *et al.* 1998). Another disadvantage of radiographic film is their sensitivity to light and requiring chemical processing. Perucha *et al.* (2003) pointed out the difficulty to control physical and chemical processes that take place from the irradiation of the field to the optical density analysis as a limitation for the use of film in radiosurgical beams. Radiochromic films, in contrast, are insensitive to light and nearly tissue equivalent ($Z_{eff} = 6.98$). The process of image formation involves the coloration of a material by the absorption of ionizing radiation. The material consist of double-layer radiochromic sensors dispersion coated on both sides of a polyester base (GafChromic MD-55-2 film). GafChromic is a self-developing film and relatively energy and dose rate independent (Niroomand-Rad *et al.* 1998). A recent work by Wong *et al.* (2009) suggested GafChromic film as the gold standard dosimeter for fields as small as 3 $\times$ 3 cm^2 against measurements with gel and TLD dosimeters. García-Garduño *et al.* (2010) performed a detailed study of small field dosimetry using GafChromic film against Monte Carlo simulations. Their results also showed radiochromic films provide accurate dosimetry and excellent agreement with Monte Carlo simulations. Although GafChromic film are better suited than radiographic films to characterize small fields, have high spatial resolution and can be immerse in water, readout process is still a limitation. It is necessary to wait up to 48 hours after irradiation to ensure full colour growth (García-Garduño *et al.* 2010). Nonlinearity of the response for doses in the clinical range is also a limitation (Ramani *et al.* 1994).

2.5.4   Diode detector

Diodes have been widely used as ionizing radiation detectors. Their high sensitivity and real-time readout make diodes attractive as radiation therapy dosimeters where small size is necessary. Only 3.6 eV is required to create an electron-hole pair compared to a value of 33.85 eV required in air; therefore silicon detectors have some advantage when small-size detectors are required. The physics and operation of diodes are well understood. Detailed reviews can be found in the Report of Task Group 62 (2005) and Rosenfeld (2007). The sensitive structure in silicon diodes is the pn junction formed by N- and P-type doped silicon. In this pn junc-

tion charge carriers from each side diffuse to the opposite side creating a strong electric field establishing a situation of equilibrium. The electric field across the junction makes charge collection feasible without an external bias. Due to defects and impurities in the semiconductor structure, recombination-generation (RG) centres are created. The electron-hole pairs created in the semiconductor due to the incident radiation may recombine with the RG centres. This recombination rate is the cause of the variation of diode sensitivity and dose rate dependence (Wilkins *et al.* 1997) observed in silicon detectors used in radiation dosimetry.

Silicon diodes have the advantage of small size which satisfies Bragg-Gray cavity theory (Wang and Rogers 2007). The mass collision stopping power ratio is almost energy independent in the MV energy range. Some of the disadvantage of silicon detectors is the over-response to low and medium energy photons compared to water (smaller than 150 keV). Therefore, shielded diodes have been designed to partially absorb backscatter low-energy photons (Grusell and Rikner 1986). However, when the scatter is insignificant an under-response can arise due to over absorption (McKerracher and Thwaites 1999). Other significant problems with diode detectors are temperature dependence (Grusell and Rikner 1986) and directional dependence (Higgins *et al.* 2003).

Diode dosimeters have been used for in vivo measurements of entrance and exit doses and for checking the correct beam setting. Because of their small size and high spatial resolution diodes are useful for beam data measurements in stereotactic radiosurgery. McKerracher and Thwaites (1999) used diodes to measure PDD curves, OFs, and beam profiles. They found good agreements between diodes and film for profiles measurements. Their study revealed no changes in energy response from low-energy photons at depth with small field sizes. PDD curves have been accurately measured using diodes; although OFs measurements still remain to be a challenge and the use of silicon detectors alone is not recommended by these authors. However, they recommended the use of unshielded diodes for these measurements. Sauer and Wilbert (2007) measured OFs for small photon beams. They verified that silicon detectors sensitivity increases with increasing field size, which can be attributed to the higher low-energy photon component of the spectrum with field size. This was also reported by McKerracher and Thwaites

(1999). However, these authors claimed that because the sensitivity variation of silicon diodes is linear with field size, corrections can be easily performed. In conclusion, diode detectors are well suited for accurate measurements where high spatial resolution is required, but corrections have to be taken into account to overcome the mentioned limitations (Laub *et al.* 1999).

2.5.5 Diamond detectors

Diamond detectors consist of a piece of natural diamond as the sensitive volume (Rosenfeld 2007). They are attractive as dosimeters in radiation therapy due to the near tissue equivalence of carbon's atomic number to tissue. They present mechanical stability, and high radiation hardness (Hoban *et al.* 1994). They are water resistant, and their response is relatively independent of temperature. Some studies have demonstrated that the diamond response is independent of the beam energy (Angelis *et al.* 2002). These characteristics have made diamond detectors useful detector for the characterization of small fields. Heydarian *et al.* (1995) presented a detailed comparison of several detectors and Monte Carlo simulations. They found good agreement between Monte Carlo and diamond profiles, OFs and PDD curves measurements. Das *et al.* (2000) also used diamond detectors for beam dosimetry in stereotactic radiosurgery. Their work showed a good agreement between diamond and film for dose profile measurements. Pappas *et al.* (2008) pointed out that diamond dosimeters can be considered as suitable detectors for small field dosimetry provided accurate positioning is overcome. However, diamond dosimeters have some drawbacks. De Angelis *et al.* (2002) studied the performance of diamond detectors in photon and electron beams. They found that diamond detectors of the same type might have different behaviour. Sauer and Wilbert (2007) found that diamond detectors can have a significant energy dependence which is due to their construction. They need to be pre-irradiated before daily use to stabilize their response (De Angelis *et al.* 2002). Another problem is dose rate dependence, which needs to be corrected for with the use of correction factors.

2.5.6 Gel dosimetry

Gel dosimetry is one of the most attractive techniques for small fields. This is due to the equivalence of gel materials and soft-tissue. Gel dosimeters comprise both, detectors and phantoms. There are two common gel materials: Fricke, and polymer-based gels. Of these, polymer-based gels showed better performance in dosimetry. Polymer gel dosimeters are fabricated from radiation sensitive chemicals (polyacrylamide gel, PAG) which, upon irradiation, polymerize as a function of the absorbed radiation dose. They present advantages over conventional dosimeters because it is possible to measure real three-dimensional (3D) dose distributions. This is particularly useful in small-field dosimetry where steep dose gradients are encountered. The relevance of gel dosimetry in modern radiation therapy has been well documented recently in two extensive reviews (Baldock *et al.* 2010, Taylor *et al.* 2011).

Gel dosimetry consists of an anthropomorphically shaped container into which the gel material is poured. After accurate calibration, gel dosimetry can even provide absolute dosimetry (Baldock *et al.* 1999). The irradiation of a gel material induces a chemical reaction or polymerization. Polymer gel dosimeters becomes visibly opaque with absorbed dose. There is a change in absorption coefficient which is related to an associated change in mass density. Viscosity also changes upon irradiation. All these chemical changes favour different read-out techniques. Among them, magnetic resonance imaging MRI, optical computerized tomography (optical-CT) and X-ray computerized tomography (X-ray CT) are the most-extensively used imaging techniques. Optical-CT exploits the changes in opacity of gel dosimeters after irradiation (Gore *et al.* 1996), and X-ray CT is based on the changes in the absorption coefficient of the irradiated polymer gel. Several authors have applied gel dosimetry to small-field measurements. Pappas etal (2006) used polymer gel dosimeters to study the relationship between detector size and profiles of a 5 mm field. Even with the high spatial resolution achieved with gel dosimeters (0.25 mm pixel pitch in this work), these authors had to recourse to zero detector size extrapolation to estimate the true profile. In this study it was noticed that gel dosimeters overestimated the tail region of the stereotactic profiles. Pappas *et al.* (2008) suggested that this overestimation is

due to a possible nonlinearity response at low doses. Wong *et al.* (2009) studied small-field profiles using gel dosimeters. They found penumbra widths measured with gel slightly larger than the penumbra measured with gafchromic films, and recommended the use of gel only if a high Tesla MRI is available.

Although gel dosimetry is becoming well established as an accurate technique, there are some difficulties that have to be taken into consideration for its clinical implementation. The approximate time for a typical 3D gel dosimetry procedure may last more than 24 hours (Baldock *et al.* 2010). This time encompasses fabrication, storage, irradiation, stabilization, scanning (MRI, X-ray CT or optical-CT), and imaging processing. There are imaging artefacts associated to MRI scanning that cause spatial deformation of the images (De Deene 2004). Low levels of oxygen or chemical impurities affect gel samples and may introduce nonlinearities (De Deene *et al.* 2000). This has been minimized by keeping the gels in an oxygen-free atmosphere (argon-filled flask) (Wong *et al.* 2009). Gel dosimetry can be an accurate dosimetric technique capable of 3D dosimetry which is not achieved using ionization chambers and conventional dosimeters. However, it requires a considerable experienced personnel to deal with all steps involved from fabrication of the gel material to the correct interpretation of the selected imaging technique.

2.5.7   Monte Carlo simulations

Monte Carlo simulation is established as a useful tool in radiation therapy dosimetry and more recently for the study of small-photon fields (Verhaegen *et al.* 1998). MC simulation has proven to be a reliable tool when dosimetric information is not available or possible. The use of MC simulations in the study of small-field dosimetry is usually directed to: (a) the comprehensive simulation of stereotactic treatment units (linear accelerators) for the prediction of detector response, variations of photon and electron spectra in water, and the calculation of dosimetric parameters (OFs, PDD curves, and beam profiles), and (b) the calculation of dosimeter correction factors for small fields.

Heydarian *et al.* (1995) used MC simulations to compare the dosimetric performance of several detectors with a well validated MC-generated photon spec-

trum. Through the developed MC model they were able to identify the parameters affecting each detector for dosimetric measurements (OFs, PDD curves and beam profiles) to predict treatment planning requirements. It was also shown how changes in photon and electron spectra with field size and depths affect stopping power ratios. Verhaegen *et al.* (1998) simulated a 6 MV stereotactic radiosurgery unit. They demonstrated that Monte Carlo simulation of small photon fields was possible through the code BEAM/EGS4 (Rogers *et al.* 1995). However, the simulation of stereotactic units is not straightforward and pose stringent steps: an accurate simulation of the treatment unit to produce a realistic beam; this beam is used as an input for a MC simulation; the beam model has to be tuned and commissioned by validating it against measured data (usually beam profiles an PDD curves). Shan *et al.* (2008) presented a detailed study of the influence of focal spot size on characteristics of small fields. They found that the size of the focal spot source affects significantly PDD curves for fields equal or smaller than 5 mm. Similarly, they showed that Monte Carlo-calculated beam profiles present a significant dependence on the focal spot size for field sizes from about 1.5 mm in diameter to standard square fields of the order of 10×10 cm^2. These findings demonstrated the importance of an accurate description of the source in stereotactic units. Accurate Monte Carlo simulations also help predict dosimetric properties of small fields where detector response are unreliable due to lack of lateral electronic equilibrium. Scott *et al.* (2008) showed that an accurate Monte Carlo model for a linear accelerator matched to large fields can be reliably used to describe smaller fields. This was verified from the good agreement obtained for measured and calculated output factors.

After a Monte Carlo beam model is accurately tuned to describe small fields, it is possible to use it to study the behaviour of detectors under different conditions (Heydarian *et al.* 1995, González-Castaño *et al.* 2008, Scott *et al.* 2008). When experimental measurements are not possible Monte Carlo simulations have demonstrated to be a powerful tool. Perturbation factors for ionization chambers can be accurately calculated for nonstandard conditions (Crop *et al.* 2009). Sánchez-Doblado *et al.* (2003) calculated stopping-power ratios. However, relying solely on the use of Monte Carlo simulation for dosimetric calculations is

impractical. This is because Monte Carlo techniques require extensive computing time to give acceptable levels of uncertainties in clinical practice. Monte Carlo codes are not free from systematic errors due to cross section inaccuracies and approximation. Therefore, Monte Carlo results should always be accompanied by experimental validations.

2.6 Summary

In this chapter the main requirements for detectors in radiation therapy and the limitations encountered when small fields are used were discussed. A brief review of the state-of-the-art small-field dosimetry was presented. The main conclusions drawn from this chapter are:

- Currently no detectors meet all requirements for radiation therapy dosimetry.

- No single detector has been found to meet all requirements in small field dosimetry, instead a combination of detectors is used.

- Ionization chambers, the gold standard in radiation therapy dosimetry, present severe limitations when measuring dosimetric parameters for small fields.

- The most accurate detectors in terms of tissue equivalence and real three-dimensional (3D) dose distribution measurement present drawbacks that need to be considered very carefully before their clinical implementation (e.g. gel dosimetry).

- Diode detectors are well suited for accurate measurements where high spatial resolution is required, corrections of their response can be performed easily.

- Film dosimetry continues to give accurate results, in particular where a two-dimensional dose distribution is required, however reliability, nonlinearity and development time remain to be an issue.

- A detector with a spatial resolution similar or better to/than that offered by diode detectors, with the capability of providing, at least, two-dimensional

dose distribution measurement and fast electronic readout to allow for an efficient interpretation of dose would be a major contribution in the dosimetry of small fields.

Chapter 3

Performance and characteristics of CMOS APS

3.1 Overview of chapter

This chapter describes CMOS active pixel sensors, the features of the technology and how CMOS sensors work. CMOS sensors consists of light sensitive elements or pixels that are capable of producing an electrical signal proportional to the incident amount of light or radiation. This is an attractive feature for dosimetry applications. CMOS sensors operations share essentially the same characteristics with CCD sensors, but with significant differences that can improve imaging performance. Some of these advantages are analyzed as well as the main sources of noise that limit CMOS APS performance. The optical characterization of the sensor is also presented through the photon transfer analysis to determine sensor parameters.

3.2 General description of CMOS imagers

3.2.1 Active pixel sensor

CMOS active pixel sensors (CMOS APS) receive their name due to the implementation of a buffer/amplifier (transistor) in the pixel (Fossum 1997). This amplifier is only active during readout, producing low power consumption (50–100 mW). The usual architecture of a 3-T APS (3T stands for 3 transistors) is shown on the right side of figure 3.1.

Three transistors are inside the pixel. The transistor **MRST** is used to reset
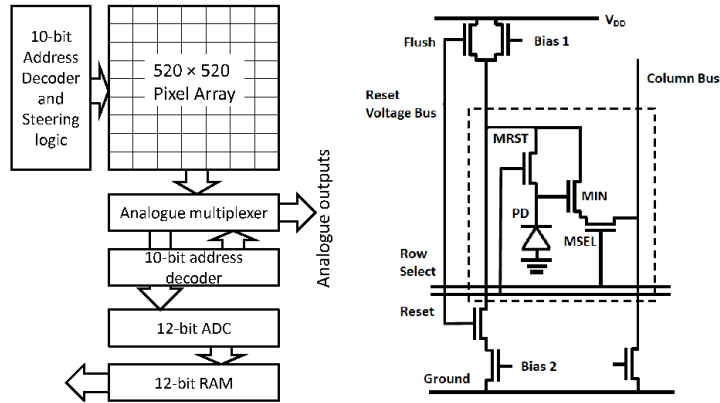
Figure 3.1: Schematic of pixel architecture of the Vanilla sensor (3-T APS).

the pixel, **MIN** is the buffer and **MSEL** is used to select the readout of the pixel. Charge to voltage conversion is performed inside the pixel, which allows operations in the voltage domain. Pixels can be randomly accessed. In this sense, each pixel is considered as an active detector element. This characteristic offers an advantage (unlike CCD) because it avoids charge transfer over long distances. Another advantage that makes CMOS APS performance promising is that they are based on CMOS technology, which is characterized by low power consumption and a high density of logic functions on a chip. Radiation hardness is an important property of radiation detectors for medical applications. CMOS deep-submicron technology has been demonstrated to be radiation resistant (Rao *et al.* 2008). The main advantages of CMOS sensors are high-speed imaging, random access readout, on-chip functionality and compatibility with standard CMOS technology. For a review of CMOS image sensors we refer to Bigas *et al.* (2006).

3.2.2 Digital pixel sensor

Digital pixel sensors (DPS) employs an analog-to-digital converter (ADC) in the pixel in order to produce digital data at the output of the image sensor array. This technology results in an increase in the frame rate of the sensor. The DPS architecture offers several advantages such as better scaling with CMOS technology due to reduced analog circuit performance demands, the elimination of

column fixed-pattern noise (FPN) and column readout noise, simplicity, on-chip processing, low power consumption, wide dynamic range and lower cost. This is achieved by employing an ADC and memory at each pixel which enables parallel operation to allow high-speed imaging applications. However, some drawbacks of DPS architecture are the use of more transistors per pixel and that DPS are still in the development stage. Nevertheless, DPS architecture is promising in high-speed applications (Kleinfelder *et al.* 2001).

3.3   Radiation detection principle

CMOS sensors have shown good properties as ionizing radiation detectors due to the mechanism to collect the generated electrons over their sensitive volume. In modern CMOS process, n- and p-wells are fabricated on top of a thin p-doped epitaxial layer. In each pixel diodes are formed by the doped interfaces. A potential well confines the generated electrons or minority carriers in the field-free epitaxial layer (which is usually up to 20 μm) until they diffuse towards one or more diodes where they are collected (Kleinfelder *et al.* 2002). The epitaxial layer is slightly doped in contrast to a higher doped p-substrate whose function is for mechanical support. Charge collection in CMOS sensors is purely the result of diffusion produced by the difference in doping concentration over the pixel volume and direct collection of electrons in the depletion region (Turchetta *et al.* 2002). The process has demonstrated to be highly efficient for incident charged particles (100% fill factor) and it has been used for electron microscopy (Kleinfelder *et al.* 2007). Figure 3.2 depicts charge collection after the generation of electron-hole pairs by ionizing radiation.

3.4   Operation of CMOS sensors

3.4.1   Signal formation

A CMOS active pixel sensor consists of an array of pixels. Each pixel has a photodiode and three transistors. The diode is reverse biased by connecting it to a VDD voltage through the reset switch. The photodiode acts as a collector of the charge generated by ionizing particles. Before the integration of this charge, the capacitor in each pixel is charged to a reference voltage. When the integration
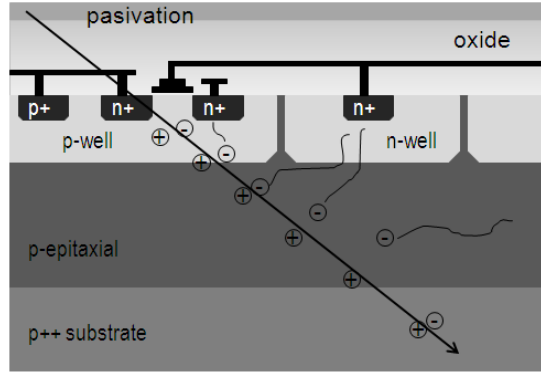
Figure 3.2: Cross section of a CMOS active pixel sensor.

starts (figure 3.3), the capacitor is discharged through the photodiode. This lowers the voltage on the diode. The rate of discharge of the capacitor is proportional to the level of incident ionizing radiation. At the end of the integration period, the charge that remains in the capacitor is read out and digitized.

Charge generation is described by a parameter called quantum efficiency (QE) which describes the ability of a semiconductor to generate electrons from incident photons. For visible light QE depends upon the wavelengths of the incident radiation. CMOS active pixel sensor design aims to reduce losses due to absorption, reflection, and transmission which limit significantly the response of CMOS imagers. However, for incident X-ray energies encountered in radiation therapy losses due to reflection and absorption do not limit CMOS imagers performance. Absorption loss is associated to the metal layers which prevent the light being absorbed in the diode, limiting QE of CMOS sensors. CMOS process requires several metal layers to interconnect MOSFETs. This, however, would not significantly limit X-ray interactions in the epitaxial layer and the subsequent absorption of the electrons generated. Reflection is not significant as it depends upon the wavelengths of the incident light. However, transmission loss which takes place when the incoming X-ray passes through the sensor without interacting is relatively high at certain energies. For a 6 MV linear accelerator photon spectrum, 0.0013% photons will interact via photoelectric absorption, 0.018% via Compton absorption and 0.00032% via pair production absorption; the rest will pass through the silicon layers without interacting. This accounts only for 0.02% of the incident photons of the spectrum. Figure 3.4 shows Compton and photoelectric interac-
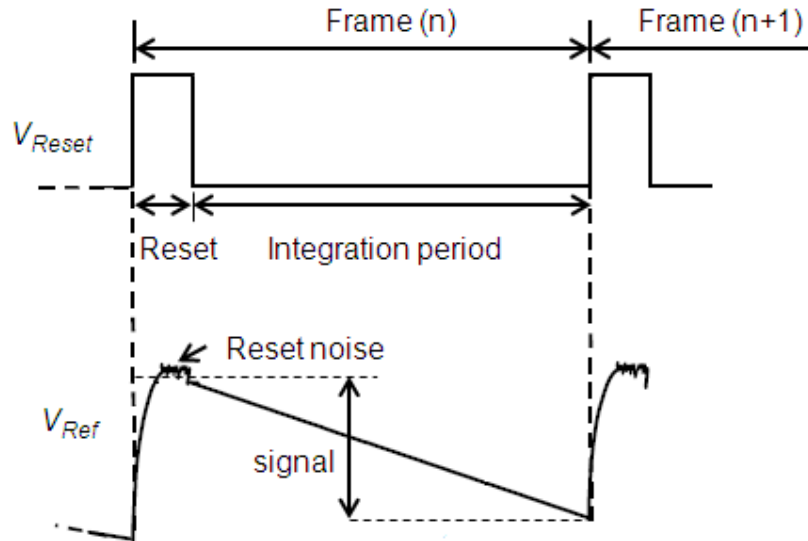
Figure 3.3: Signals in a CMOS sensor: when the integration starts, the capacitor is discharged through the photodiode. This lowers the voltage on the diode. Adapted from Magnan 2003.

tions in 14 μm of silicon as a function of the incident photon energies. The signal electrons produced by a CMOS sensor for radiation therapy applications will then be determined by photoelectric, Compton and pair production processes whose interaction probabilities depend on the physical properties of silicon, the incident X-ray energy and the thickness of the silicon layer.

3.4.2 Charge collection

Charge collection refers to the ability of the sensor to accurately reproduce an image after electrons are generated in the silicon layer. The introduction of p- and n-wells creates p-n junctions that can be used as detecting elements to increase charge collection efficiency (Turchetta *et al.* 2003). These small structures are shown just below the metal layer in figure 3.2. Charge collection in CMOS imagers depends mainly upon diffusion of electrons generated in the epitaxial layer. The potential well that confines electrons in the photodiode volume is proportional to kT/q, where k is the Boltzmann's constant, T is the operating temperature (in kelvin) and q is the charge of an electron, and the doping concentration in the layers (Turchetta *et al.* 2003). This has shown CMOS sensors to be excellent electron detectors in terms of detection efficiency (Deptuch *et al.* 2002). Charge collection is, however, limited by charge spreading which increases with the epi-
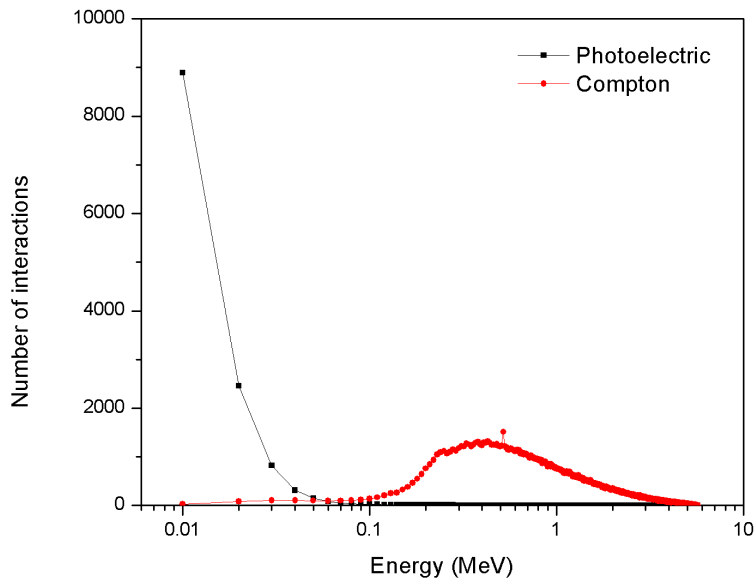
Figure 3.4: Compton and photoelectric interactions in 14 μm of silicon.

taxial layer thickness. The spreading to neighbouring pixels will cause a reduction of the charge collected by a pixel, which worsens image quality. Charge collection and therefore image quality are also determined by the number of charges that pixels can hold (full well capacity), the pixel to pixel nonuniformity and the charge collection efficiency.

3.4.3 Readout process

After integration, readout is performed by turning on the selector transistor. The charge in each pixel in a row is transfered to the column output through the charge amplifier. This is possible by clocking the row selectors sequentially, which in turn allows the full image to be progressively read out from the pixels. The column output is then serially transferred by a readout register to an analogue to digital converter. When a limited number of row selectors is clocked and pixels from the beginning and end of the rows are discarded, a specific region from the array can be read out. This technique is known as windowing. By sampling pixels in this way the readout speed is significantly increased allowing high frame rates. Frame rates of 1000 frame s^{-1} have been reported (Salama and El Gammal 2003). Readout speed is proportional to the type of analogue-to-digital conversion scheme used. The current technology allows in-pixel conversion, single-chip and column-

parallel solutions. Each of these solutions requires a different ADC architecture which is in general demanded by the application.

3.5   Sources of noise

Noise in CMOS sensors is, in general, much larger than in CCDs. One of the reasons is the read noise, which is limited by the source follower MOSFET. Within read noise, reset noise is entirely removed by CDS (correlated double sampling) signal processing in CCDs; however, this is more difficult to do for some CMOS pixel architectures. This has marked a fundamental difference between both technologies and continues to be a limiting factor for CMOS sensors in terms of image quality.

Noise in CMOS sensors can be categorized as temporal and spatial noise. Temporal noise refers to the time-dependent fluctuation in the signal generated in the sensor and it sets the fundamental limit on image sensor performance (Tian *et al.* 2001). It comprises signal shot noise, sense node reset noise, pixel source follower noise, column amplifier and dark shot noise. All sources, but signal shot noise, are independent of signal level and contribute to read noise.

Shot noise arises from the stochastic nature of photon and electron interaction in the sensor. The created photoelectrons contribute to the signal shot noise while the dark current shot noise appears when the dark current electrons are generated. The generation of these electrons is not related to the incoming radiation. The amplitude of the dark current is proportional to the integration time and the square root of the amount of dark electrons generated in a pixel. Pixel source follower noise limits the read noise floor and can be reduced down to approximately one electron noise rms (Janesick 2007). Reset noise is the dominant temporal noise in CMOS sensors (Turchetta *et al.* 2003). This noise is thermally generated by the channel resistance associated with the reset MOSFET induced on the sense node capacitor (Janesick 2007). The reset noise in terms of noise electrons is

$$\sigma_{reset} = \left(\frac{kTC}{q}\right)^{1/2} \tag{3.1}$$

where C is the sense node capacitance after reset, k is Boltzmann's constant and

T is the temperature. Reset noise can be entirely removed by CDS technique in CCDs. This technique requires sampling the voltage on the diode after reset and image acquisition. The first sample is determined by the reset noise, while the second one is the sum of the reset noise and the actual signal. Differential readout of the two samples gives the signal without the reset noise (Turchetta *et al.* 2003). Therefore, reset noise will increase by $2^{1/2}$ because two samples are subtracted in quadrature.

Pattern noise is a spatial source of noise. It can be subdivided into two sources: Fixed Pattern Noise (FPN) and Photo Response Non-Uniformity (PRNU). The former is produced by the pixel-to-pixel dark current variation and the variations in column amplifier offsets and gains (El Gammal *et al.* 1998). The PRNU is the variation in pixel responsivity. FPN is not a random noise and it is spatially the same pattern from image to image. This noise is proportional to the signal level and will dominate signal shot noise, which is proportional to the square root of signal over the sensor's dynamic range.

3.6   The Vanilla sensor

Vanilla is a CMOS active pixel sensor developed by a UK consortium (MI[3]) whose aim was the development of CMOS image sensors for scientific applications. The sensor was originally designed to be tested by scientists working on different fields and not optimized for dosimetry applications. It consists of an array of 520×520 pixels on a 25 μm pitch.

The sensor architecture is shown on the left-hand side of figure 3.1. It allows up to six dynamically reconfigurable regions of interest (ROI) down to 6×6 pixels. Full frame readout of over 100 frame s^{-1} and a ROI frame rate of over 20000 frame s^{-1} are available. The sensor has two operation modes. In the digital mode, the analog to digital conversion of the voltage inside the pixel is performed by the on-chip ADCs. There are 130 ADCs on-chip to perform a 12-bit successive approximation conversion. In the analog mode the voltage signal in the pixel is converted using a 12-bit ADC on an expansion board.

3.7 Sensor characterization

Imaging sensors performance parameters estimation is useful in the design, application, characterization and calibration of CMOS and CCD sensors. This is achieved through the Photon Transfer (PT) analysis. PT is considered as a measurement standard for the characterization of imaging sensors (Janesick 2007).
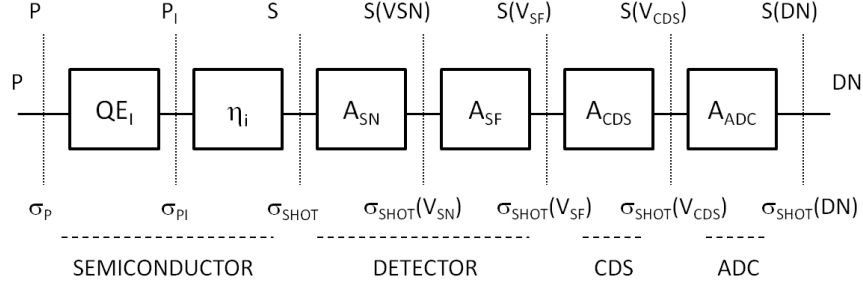
Figure 3.5: Internal gain functions and noise parameters for a semiconductor detector (Janesick 2007).

Photon transfer theory applied to CMOS sensors characterization can be understood by considering the sensor as described by transfer functions related to the semiconductor, pixel detector and electronics. The sensor input consists of a signal expressed in units of the average number of incident photons per pixel (P). Only shot noise is present at the input. The output signal is given in digital numbers (DN). The relation between the input and output signals is given by

$$\frac{S(DN)}{P} = QE_I \eta_i A_{SN} A_{SF} A_{CSD} A_{ADC},$$ (3.2)

where QE_I is the quantum efficiency, η_i is the quantum yield gain and A_{SN} the sense node gain, A_{SF} the source follower gain, A_{CSD} the correlated double sampler gain and A_{ADC} the analog-to-digital converter gain. As these gains are difficult to measure individually PT is applied. The most general description considers an input signal A characterized by a shot noise component σ_A entering the sensor. An output signal B exhibits a noise σ_B. A sensitivity constant relates and transfers output signal and noise to the input. This constant is defined as

$$K(A/B) = \frac{B}{\sigma_B^2}.$$ (3.3)

Equation 3.3 is the fundamental PT relation and it is valid only statistically. K represents the overall sensitivity of the sensor and it takes into account the internal sensitivities (i.e. sense node, interacting photon, and incident photon sensitivities). In this work sense node to ADC sensitivity $K_{ADC}(e^-/DN)$ is calculated to convert output signal in DN into e^-. The sense node is a region in the pixel where the created signal charge is converted to a voltage and buffered by the source follower amplifier.

Table 3.1: CMOS sensors signal and noise parameters (Janesick 2007).

Parameter	Average signal	Noise (rms)
Incident photons	P	$\sigma_{SHOT}(P)$
Interacting photons	P_I	$\sigma_{SHOT}(P_I)$
Sense node electrons	S	σ_{SHOT}
Sense node voltage	$S(V_{SN})$	$\sigma_{SHOT}(V_{SN})$
Source follower voltage	$S(V_{SF})$	$\sigma_{SHOT}(V_{SF})$
CDS voltage	$S(V_{CDS})$	$\sigma_{SHOT}(V_{CDS})$
ADC signal	$S(V_{DN})$	$\sigma_{SHOT}(DN)$

Four different noise regimes are found through the PT analysis: read noise, shot noise, fixed pattern noise and full well noise. Figure 3.6 shows an ideal photon transfer curve and the four noise regimes plotted on a Log-Log scale. RMS noise is plotted against the average signal output in DN. This curve is obtained by illuminating the sensor with an increasing intensity light source. The only noise introduced at the input is the shot noise, which is inherent to the photon interaction nature. This noise can be predicted easily from

$$\sigma_{SHOT} = (\eta_i S)^{1/2}. \tag{3.4}$$

The shot noise becomes a straight line with slope 1/2 when it is plotted on a Log-Log scale.

The difference between the noise at the input (shot noise) and the noise at the output is introduced by the sensor. Therefore, the PT analysis compares the differences between shot noise at the input and RMS output noise showed in figure 3.6. In the absence of a stimulus input signal the noise at the output is purely random, this noise is called read noise and is independent of signal. When the

illumination increases, shot noise is dominant, and when the input signal increases even more, fixed pattern noise (FPN) becomes more significant. This noise results from differences in sensitivity from pixel to pixel. Full well noise is achieved when pixels cannot hold more charges. Output noise drops abruptly because charge sharing between adjacent pixels averages the signal and suppresses random noise.
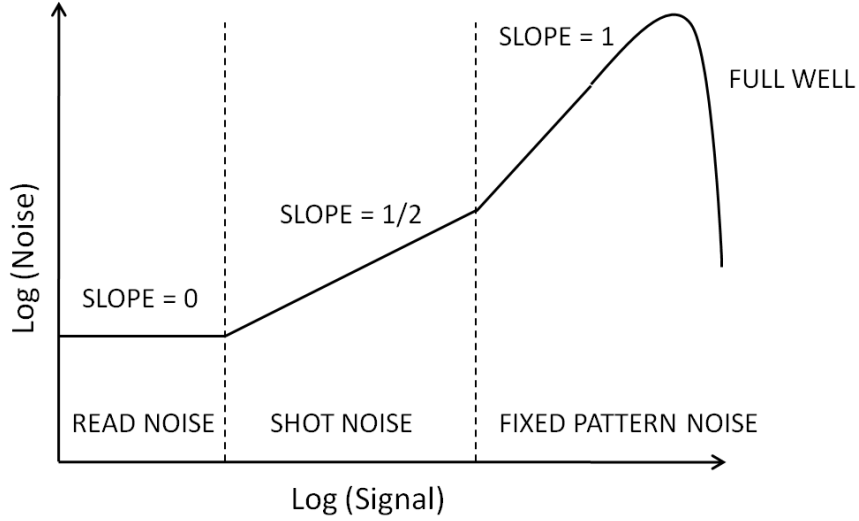
Figure 3.6: Ideal Photon Transfer Curve showing noise regimes in CMOS sensors.

The sensitivity $K(e^-/DN)$ can be obtained from figure 3.6 and is given by

$$K(e^-/DN) = \frac{S(DN)}{\sigma_S(DN)^2 - \sigma_R(DN)^2} \qquad (3.5)$$

where $\sigma_R(DN)^2$ is the read noise, and $\sigma_S(DN)^2$ is the total noise. P_N is the quality factor and can be estimated from the intercept of a linear fit on the FPN curve on the x-axis. The difference $\sigma_S(DN)^2 - \sigma_R(DN)^2$ is the shot noise.

The total noise in figure 3.6 is found from

$$\sigma_S(DN) = \left\{ \sigma_R(DN)^2 + \frac{S(DN)}{K(e^-/DN)} + [P_N S(DN)^2] \right\}^{1/2} \qquad (3.6)$$

where the last term is the FPN which follows the expression $\sigma_{FPN} = 0.011 \times S(DN)$. For equation 3.6 to be useful, shot noise must be isolated. By subtracting two consecutive frames at the same illumination level the FPN is removed. Read noise is found from the intercept in the PT curve and subtracted from the remaining term in equation 3.6. Once shot noise is isolated, the sensor parameters

can be determined.

To determine the conversion gain from the photon-transfer curve, the fixed pattern noise has to be removed by using the following relations

$$\bar{S}_k = \frac{1}{LM} \sum_{i,j} S_{i,j}^k. \tag{3.7}$$

$$\bar{S} = \frac{1}{2}(\bar{S}_A + \bar{S}_B) - \bar{S}_D. \tag{3.8}$$

$$\sigma_S^2 = \frac{1}{2(N-1)} \sum_{i,j} [(S_{i,j}^A - \bar{S}_A) - (S_{i,j}^B - \bar{S}_B)]^2. \tag{3.9}$$

where $\bar{S}_k$ is the mean frame and $\bar{S}_A$ and $\bar{S}_B$ are two consecutive frames that must be subtracted to remove fixed pattern noise, and σ_S^2 is the signal variance. Read noise can also be calculated by applying equations 3.5 to 3.9 to the dark frames.

The method presented above assume that the sensor response is linear, thus a constant sensor sensitivity is obtained over the sensor dynamic range. This could lead to inaccurate values for the sensor sensitivity as the signal output increases. Nonlinearity can be seen from PT analysis when the slope of the shot noise regime deviates from 1/2.

There are two types of gain nonlinearities that limit CMOS and CCD performance: V/V and V/e^- nonlinearities. V/V nonlinearity is produced by the source follower amplifier in each pixel. V/e- nonlinearity is related to sense node diode capacitance; therefore it is dominant as signal increases.

Nonlinear compensation analysis (NLC) accounts for nonlinearity by decomposing $K(e^-/DN)$ into a signal gain $S(e^-/DN)$ and noise gain $N(e^-/DN)$. The signal gain represents the sensor sensitivity from the first illumination level up to full well capacity. Noise gain is used to calculate the signal electrons in the absence of signal (read noise). At low illumination levels $K(e^-/DN)$ obtained by PT analysis is used to calculate signal electrons for the first illumination level. This first signal is taken to produce output signal electrons up to full well capacity condition. An accurate determination of the number of incident photons per pixel during integration time for all illumination levels gives a proportionality ratio to generate the signal electrons. Once this signal is determined, the signal

gain $S(e^-/DN)$ is produced by the quotient between the signal in electrons and the signal in DN.

3.8   Photon transfer measurements

The sensor was optically characterized to obtain the ADC sensitivities $K_{ADC}(e^-/DN)$ and $S_{ADC}(e^-/DN)$ through the photon transfer technique and the nonlinear compensation method (NLC). This characterization was necessary to express ADC outputs in absolute units (e^-) rather than relative units like digital numbers (DN). By characterizing the sensor signal in terms of electron units a direct connection with dosimetry can be achieved. In addition, a full determination and quantification of sources of noise is obtained from the same analysis.
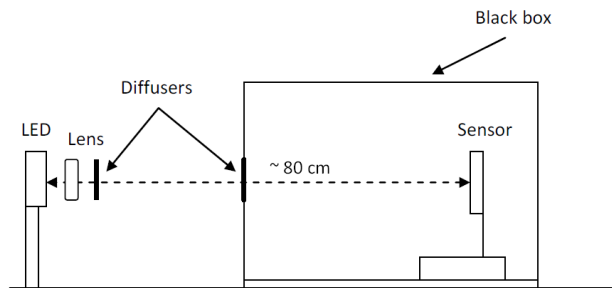
Figure 3.7: Setup used for sensor characterization.

The sensor was operated under very low illumination level and placed inside a metallic black box (figure 3.7). The sensor was illuminated by a narrow-band light emitter diode (LumiLED) at 520 nm coupled with two white diffusion sheets (Lee Filters, white 129) with 87% attenuation. A lens was placed in front of the LED to focus light intensity across the sensor surface. Light intensity was varied by changing the voltage across the LED to cover the dynamic range of the sensor. The voltage was uniformly varied from 2.16 V up to 19.68 V to achieve sensor saturation using steps of 0.08 V.

For NLC analysis photon flux measurements had to be accurately determined. A calibrated photodiode (Hamamatsu S1336-5BQ) was placed at the same position of the sensor after completion of image acquisition. The output current proportional to the photon flux input signal was measured using a Keithley 237 High

Voltage Source-Measure Unit (SMU). Over a hundred measures were averaged to obtain the output current that corresponded to each illumination level to calculate the total number of incident photons per pixel during the sensor integration time.

Image acquisition and control of the sensor were performed through the MI^3 OptoDAq system. This system was based on a Memec Virtex-II Pro^{TM} 20FF1152 FPGA development board which generated the required control signal for the sensor. Data was transferred to a PC by an optical transceiver at gigabits per second. The sensor was operated in digital mode at 4 frames per second. A hard reset was used to operate the sensor. Hard reset refers to the reset transistor in strong inversion and the photodiode and reset drain in thermal equilibrium during the reset period (Fossum 2003). This choice has been reported to give a good compromise between performance of the linear and nonlinear analysis (Bohndiek 2008).

3.8.1 Photon Transfer Curve

Figure 3.8 shows the PT curve derived from measurements with the Vanilla sensor. All sources of noise are shown independently. The read noise found from the PTC intercept on the rms noise axis was 2.7 DN. Read noise was also calculated by applying equations 3.5 to 3.9 to the dark frames. This analysis was performed 25 times from different regions of interest (ROIs) over the dark frames. The estimated read noise was $\sigma_{READ} = 2.63 \pm 0.02$ DN.

The fixed pattern noise was calculated from a linear fit on the FPN data at higher signal levels in figure 3.8. The inverse of the intercept on the horizontal axis gave a quality factor $P_N = 1/86 = 0.011$ (1.2%). This is a typical value reported for CMOS and CCD sensors (Janesick 2007).

Figure 3.9 shows ADC signal and noise sensitivities. $K(e^-/DN)$ is shown for comparison. The overestimation introduced is clearly seen if $K(e^-/DN)$ is used instead of $S(e^-/DN)$. This is produced by the nonlinearity inherent in CMOS sensors discussed in section 3.7. Using the ADC signal and noise sensitivities the read noise can be expressed in units of electrons, this is $\sigma_{READ} = 47 \pm 1$ e^-. Full well capacity was found from the highest signal achieved before saturation,
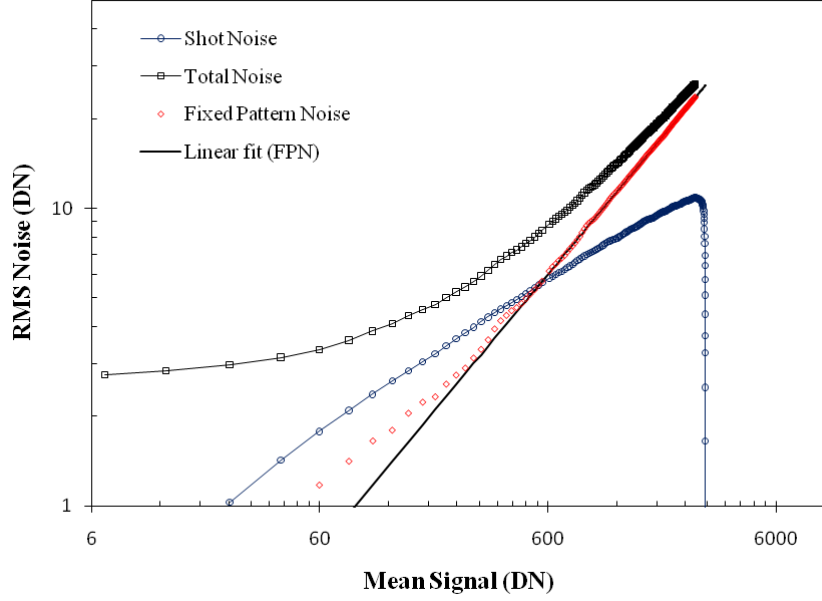
Figure 3.8: Photon Transfer Curve derived from measurements with the Vanilla sensor.

this was obtained from figure 3.8 by multiplying this signal by the interpolated $S(e^-/DN)$. Full well capacity was found to be 47200 e^-. This value also depends on the sensor internal parameters that can be adjusted to increase the dynamic range of the sensor. From these results the dynamic range (DR) of the sensor can be estimated. The dynamic range in decibels is $DR(db) = 20 \times \log_{10}(DR)$, where DR is the ratio between the signal at full well and the read noise in units of electrons. From these values a dynamic range of 60 db was estimated.

3.8.2 Signal-to-noise performance

Signal-to-noise performance is a very important parameter of imaging sensors. Signal-to-noise for X-ray imaging applications is severely limited by shot noise. This can be seen from the equation given by

$$SNR = \frac{S}{\sigma_{TOTAL}} \tag{3.10}$$

$$= \frac{S}{[\sigma_{READ}^2 + \eta_i S + (P_N S)^2]^{1/2}}. \tag{3.11}$$

From the equations above it can be seen that SNR within the shot noise regime is proportional to the square root of the signal. Shot noise limits the signal-to-
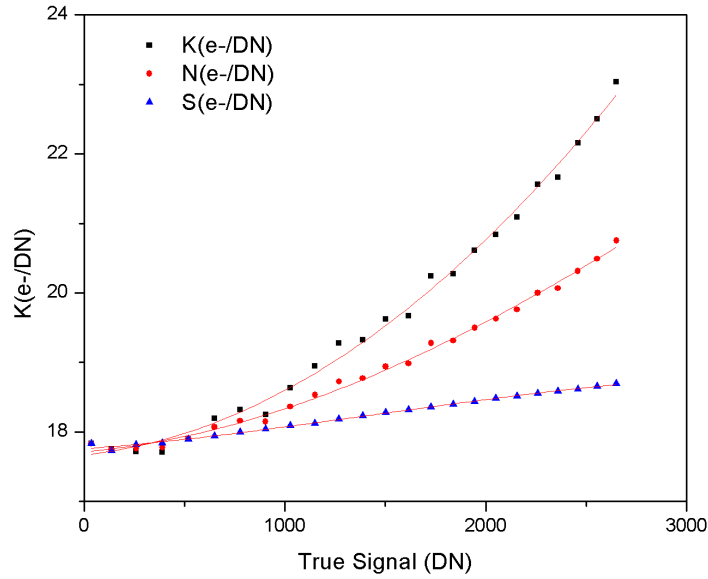
Figure 3.9: ADC sensitivities.

noise performance when detected signals are large. This represents a fundamental limit for imaging sensors which can only be improved by increasing the full well capacity of the sensor.

Signal-to-noise performance was derived from PT analysis. By dividing the signal and the total noise given in equation 3.6 signal-to-noise performance was determined. Figure 3.10 plots S/N against signal in units of electrons.

Over this graph the three noise regimes seen on PT curves are also present: SNR for the read noise regime with slope 1 which is proportional to signal, the SNR within the shot noise regime characterized by a slope 1/2, and the SNR within FPN regime is independent of signal and produces a slope approaching 0 (ideally 0). The sudden increase in signal is a full well saturation artefact where pixel crosstalk reduces noise modulation.

3.9 Dark current

Dark current in CMOS active pixel sensors is an unwanted source of charge generated by all pixels in the photodiode node in the absence of stimulus input signal. Although many kinds of dark current sources exist, thermally generated dark current is the most common source. Dark current magnitude is proportional to the
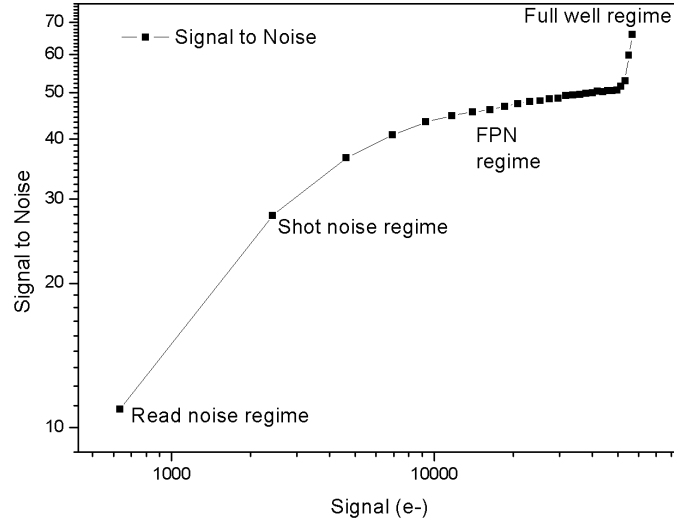
Figure 3.10: Signal to noise as a function of signal in units of electrons.

temperature (doubling approximately every 5-8 °C) and it depends on the photo-diode geometry, the transistors, and the interconnectivity in the pixel (Shcherback *et al.* 2002). This thermally generated current combines with the photocurrent to be directly integrated over the diode capacitance, which sets a lower limit on the detectable signal (read noise floor). Dark current creates a spatially-random and temporally-fixed noise pattern that limits the ultimate sensitivity of an imaging system (shot noise and Fixed Pattern Noise). Dark current is, therefore, an important parameter for characterizing the performance of an image sensor. This is because any decrease of the dark current will significantly improve the dynamic range due to a further reduction of the dark current shot noise and the fixed pattern noise (Loukianova *et al.* 2003).

Dark current can, however, be removed from the captured images by subtracting pixel by pixel an average frame taken in the absence of stimulus input. Figure 3.11 shows a graph of the mean signal in the absence of stimulus input as a function of integration time for one of the CMOS sensors used in this work. It is evident that the mean signal of the average frame increases with the integration time in a nonlinear way. In fact, the shot noise component of the dark current is given by

$$\sigma_{D_S HOT} = \sqrt{2.55 \times 10^{15} t P_A D_{FM} T^{1.5} \exp(-E_g/2kT)} \tag{3.12}$$

56

where P_A is the pixel area in cm^{-2}, D_{FM} is the dark current figure-of-merit at 300 K (nA/cm^2), which depends on the sensor manufacturer, k is the Boltzmann's constant (8.62×10^{-5} eV/K), and E_g is the silicon bandgap energy. From equation 3.12 it is observed that the dark current is a square-root function of the integration time if the temperature is considered to be fixed. This functional relation is slightly seen in figure 3.11. This figure also illustrates how dark current significantly limits the dynamic range of the sensor when large integration times are used. For instance, integrating for about 1.2 s reduces the dynamic range of the sensor by about 1000 digital numbers; for a 12-bit ADC this would mean a reduction of 24% which is quite significant. This simple example gives an idea of the importance of dark current reduction in CMOS sensors and its effect on sensor performance. Dark current characterization is, therefore, an important parameter to take into account when an imaging sensor is intended to be used in dosimetry.
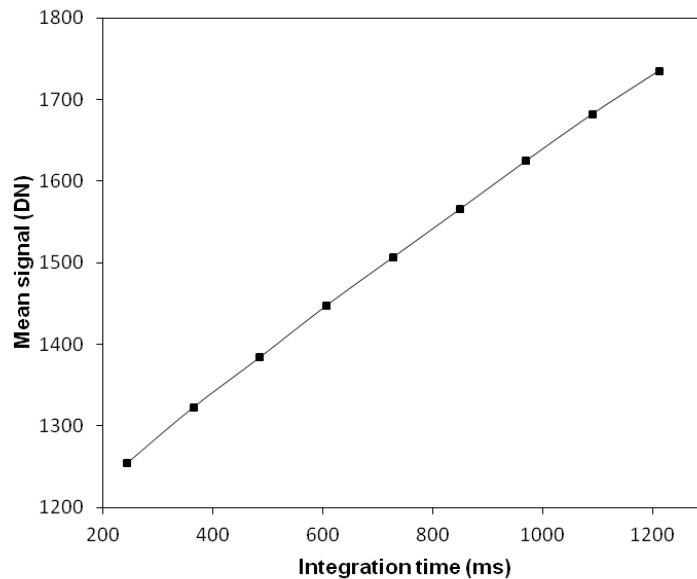
Figure 3.11: Dark signal as a function of integration time.

3.10   Discussion

In this chapter the main features and characteristics of CMOS image sensor have been presented. CMOS active pixel sensors have matured as robust and strong competitors of CCDs. The main contribution of CMOS APS is the combination inside the pixel of the detector, the charge-to-voltage conversion and transistors to provide buffering and addressing capabilities. This architecture, in contrast to CCD's, provides random access to pixel and direct windowing at a very high frame rate. CCD, in contrast, transfers charge over long distances, which is very sensitive to radiation degradation.

CMOS image sensors are well suited to work under high level of ionizing radiation. Methods have been devised to predict the radiation hardness of CMOS sensors. Deep sub-micron technology has been demonstrated to be a good candidate for fabricating CMOS image sensors for applications as medical imaging (Rao *et al.* 2008, Eid *et al.* 2001). The evolution of the technology to deeper sub-micron CMOS process guarantees the potential improvements of the radiation tolerance of the devices when exposed to high radiation energies and doses.

Regarding noise, CMOS sensors performance are still below CCDs; although the technology has demonstrated that noise, quantum efficiency, and dynamic range performance can be comparable to CCDs (Bigas *et al.* 2006). The transistors in the pixel create additional sources of noise and reduces Fill-Factor, which in turn determines sensor sensitivity.

CMOS APS suffer from a high level of fixed pattern noise (FPN), in contrast to CCD sensors, due to differences in the transistor thresholds and gain characteristics. Figure 3.8 shows FPN isolated from PTC and plotted independently. At higher signal level FPN is quite dominant, its contribution to the total noise is 1.2% of the signal, which is quite high compared with ionization chambers where the total noise is in the order of about 0.1%. The reduction of FPN has to be taken into account because shot noise is the fundamental limit on image sensor performance.

Readout noise dominates at low illumination levels and limits the low level performance of a CMOS sensor. Readout noise may be significantly high. For instance, in chapter 7 the signal measured by the sensor at 5 cm deep in Solid

Water was 9216 e^-, a readout noise level of 47 e^- represents about 5% of this signal. However, readout noise have been reported as small as 2.8 e^- (Bai *et al.* 2008), which means readout noise is no longer a limitation for high performance CMOS sensors.

Chapter 4

Monte Carlo simulation of CMOS active pixel sensors

4.1 Overview of chapter

The aim of this chapter is to outline the Monte Carlo simulation of the CMOS active pixel sensor used in this work (the Vanilla sensor). First a general overview of the Monte Carlo method and its importance in medical physics is presented. A brief description of the general-purpose Monte Carlo code GEANT4 is also given. We focus then on a discussion of the main issues involved in the accurate simulation of electron transport which is an important part of dose calculation. Before the simulation of the Vanilla sensor the effect on dose deposition in thin detectors as a function of the cut-off parameter is investigated. This was motivated because the selection of cut-offs is known to influence CPU performance as well as energy deposition accuracy. The performance of the two models available for the simulation of electron transport, namely, the multiple scattering (MSC) and Coulomb scattering are also compared to establish a simulation methodology in thin layers. Finally, the accuracy of electromagnetic cross section data is studied through experimental results.

4.2 Brief description of Monte Carlo methods

As a significant part of this thesis is based on the application of the Monte Carlo method to radiation transport a short description of its fundamentals will be given in this chapter.

A Monte Carlo method is a general method used to solve stochastic (or sometimes non-stochastic) problems by random sampling. These problems are usually determined by processes whose evolution is governed by random events (Kalos and Whitlock 2008). Radiation transport is a classical example of a stochastic process where the interaction, creation, scattering and transport of particles are determined by probability distribution functions. It relies primarily on random sampling techniques and sophisticated implementations of physical models of particle interactions and transport in complex geometries. The Monte Carlo solution to radiation transport problems intends to solve the equation (Larsen 1992)

$$
\frac{1}{v}\frac{\partial \psi}{\partial t}(r,\Omega,E,t) + \Omega \cdot \nabla \psi(r,\Omega,E,t) + \sigma_s(E)\psi(r,\Omega,E,t)
$$
$$
= \int \sigma_s(\Omega \cdot \Omega',E)\psi(r,\Omega',E,t)d\Omega' + \frac{\partial}{\partial E}\beta(E)\psi(r,\Omega,E,t), \quad (4.1)
$$

where r is the position, Ω is a unit vector denoting the direction of electron flight, E is energy and t the time. The term $\sigma_s(\Omega \cdot \Omega',E)$ is the differential scattering cross section, $\beta(E)$ is the stopping power, v is the electron speed, and $\psi(r,\Omega,E,t)d^3r\,d\Omega\,dE$ is the probable number of electrons in d^3r about r, in $d\Omega$ about Ω, and in dE about E at time t.

The Monte Carlo method solves equation 4.1 by approximating any average quantities by their expected values. As expected values can be expressed as integrals, it is easy to show that any integral can be evaluated by sampling from appropriate distribution functions. This is the essence of Monte Carlo methods.

At the present time the Monte Carlo method is widely accepted as a reliable tool in medical physics and regarded as the most accurate technique for dosimetric calculations (Andreo 1991, Rogers 2006). Its limitation is the inherent stochastic nature, which can be considered as a drawback, and consequently the large computing time required to obtain accurate results, however in some cases Monte Carlo simulation is the only option. As computational power and modern variance reduction techniques advance Monte Carlo techniques promise to be the method of choice to many applications in medical physics.

4.3 Description of the Monte Carlo code: GEANT4

GEANT4 is a C++ toolkit for the simulation of the passage of particle through matter (Agostinelli 2003). It was originally developed at CERN and released in 1999 as an effort to improve an earlier version called GEANT3 used in high energy physics simulations (based on Fortran). Its key features are a complete range of functionality to track particles through complex geometries (not offered by other codes) and a comprehensive range of physical processes. Its constant development by a large scientific collaboration makes it a powerful Monte Carlo tool in many fields.

4.3.1 Basic elements of GEANT4 simulation

- Geometry: An important concept in GEANT4 and any Monte Carlo code is a detector geometry. Detector geometry in GEANT4 is made of one or more volumes. Volumes can be any geometrical shape and/or the union of these. As GEANT4 follows an object-oriented programming approach a volume placed inside another one may inherit some properties of the container volume. The placed volume is called the daughter and the container the mother. The daughter volume inherits the coordinate system of the mother volume. These volumes are then associated to solids (geometrical objects) and materials.

- Particles: Unlike other Monte Carlo codes used for medical physics, GEANT4 provides a large range of particles. Particles are organized in lepton, meson, baryon, boson, and other particles as ions. GEANT4 defines properties, such as, name, mass, charge, spin, etc., to characterize individual particles. These particles are organized in classes which are represented by C++ objects.

- Physics processes: To describe how particles interact with materials GEANT4 defines physics processes. The seven categories are electromagnetic (EM), hadronic, transportation, decay, optical, photolepton-hadron and parameterization. GEANT4's design allows the creation of processes

and their association to specific particles by the user. This is a key feature behind the design philosophy of GEANT4. In medical physics, however, electromagnetic and hadronic processes are of interest. A large set of EM processes are provided and it is possible to combine them according to user requirements.

- Cross sections: Cross sections are the core of any Monte Carlo code. Their accurate implementation is very important and it is one of the main causes of systematic errors on any Monte Carlo result. Currently GEANT4 provides three packages for the simulation of EM processes of importance in medical physics applications.

  The Standard package's energy range is valid from 1 keV up to 100 TeV. It is mainly optimized for high energy physics applications. Cross sections are parameterized and its application in medical physics is more limited.

  The low energy package is provided to handle low energy processes which is required for medical physics applications. Its energy range goes from 250 eV up to 1 GeV. This implementation makes direct use of shell cross section data. Cross section data are taken from publicly distributed evaluated data libraries: EPDL97 (Evaluated Photons Data Library), EEDL (Evaluated Electrons Data Library), EADL (Evaluated Atomic Data Library) and binding energy values based on data of Scofield.

  An additional package available for the simulation of photons, electrons and positrons is **PENELOPE** (Salvat *et al.* 2006, Sempau *et al.* 1997) which is used in this thesis. The physics underlying this code was completely translated to the C++ language and implemented into GEANT4 as an alternative to the low energy package. The main features of this implementation is the availability of sophisticated models and the possibility to simulate down to energies of some hundreds of electron volts. On average, **PENELOPE** and EGSnrc, the gold standard in dose calculation in medical physics (Kawrakow 2000), agreed with measurement within 1 standard deviation experimental uncertainty when comparing simulated fluence profiles with experiments (Faddegon *et al.* 2009).

4.4 Issues in the implementation of electron transport

The correct implementation of radiation transport in medical physics is a challenge due to a trade off between accuracy and computing time. Accuracy is determined by the correct implementation of the different physics processes that occur in nature which are simulated using Monte Carlo methods. However, a general purpose Monte Carlo code has to deal with the solution of a radiation transport problem in an efficient way without recourse to inaccurate simplifications. This represented a major issue until Berger's introduction of the condensed history technique (Berger 1963). Due to the large number of collisions undergone by electrons while slowing down the simulation of every single interaction is time consuming for thick geometries and relatively high kinetic energies. However, it is noted that for most fast-electron interactions with atoms and orbital electrons the electrons' directions and energies are only slightly changed. In the condensed history technique the path of the electrons is broken down in small steps. As a result, it is possible to approximate the physical electron transport process by the accumulation of the global effect of many interactions in one single step. The net displacement of the particle as well as the energy loss and the change of direction at the end of the step are evaluated using multiple scattering theories (Lewis 1950).

GEANT4 deals with electron transport by considering the simulation of inelastic collisions separately. A cut-off energy value is introduced as a threshold between hard and soft collisions. Hard collisions (where large energy losses occur above the cut-off) are simulated one by one and sampled from a differential cross section thus generating secondary particles. Energy loss is accounted for by explicitly generating these delta rays. Soft collisions, on the contrary, are simulated in a condensed way. These energy losses are deposited continuously along the track of the primary particle and calculated from the restricted stopping power.

Larsen (1992) derived theoretically the Condensed History Algorithm and demonstrated that in the limit of small steps this algorithm can be considered as a Monte Carlo simulation of the Boltzmann's transport equation and that the ac-

curacy of the method depends only on the strategy taken for the simulation of the transport process, angular scattering, energy loss and the number of particles necessary for a negligible statistical error (Larsen 1992). Therefore, these strategies represent the real limitation of any Monte Carlo code in medical physics and have been subject of intensive research. We shall discuss briefly the strategies assumed for the implementation of electron transport in GEANT4. This approach differs from EGSnrc in which the remaining energy of the electron (when it reaches the cut-off) is deposited locally.

4.4.1 Energy loss models

Energy loss in GEANT4 is simulated by considering a range threshold given by the user. This value is then internally converted into energy. Below the threshold the energy loss is assumed to be continuous while an explicit production of secondary particles accounts for energy loss above the cut-off. Continuous energy loss is calculated from the Berger-Seltzer formula integrated from 0 to T_{cut} (where T_{cut} is the cut-off energy). The calculation is carried out from

$$dE_{soft}(E, T_{cut}) = n_{at} \int_0^{T_{cut}} \frac{d\sigma(Z, E, T)}{dT} T dT, \qquad (4.2)$$

where n_{at} is the number of atoms.

For energy losses above the energy cut-off the simulation of delta-rays is given from the differential cross section per atom. This is

$$\sigma(Z, E, T_{cut}) = \int_{T_{cut}}^{T_{max}} \frac{d\sigma(Z, E, T)}{dT} dT. \qquad (4.3)$$

The energy of the delta rays is sampled from the Möller and Bhabha scattering cross sections.

For continuous energy losses dE/dx tables are pre-calculated during initialization time. With this information the ranges of the particles in a given material are calculated and stored in the *Range* table. This table is inverted to obtain the *InverseRange* table. This information is used at run time to calculate values of the particle's continuous energy loss and range. Full details of this can be found in the Geant4 Physics Reference Manual available at http://geant4.org/.

When the energy loss of a particle is less than an allowed limit, ξT_0, of its kinetic energy, the dE/dx table is used. ξ is a parameter called *linearLosslimit* whose default value is 0.001. The *linearLosslimit* parameter allows users to decide the energy below which direct calculation of energy loss (as a product of step length by dE/dx) is done. In this case the energy loss is calculated from

$$\Delta T = \frac{dE}{dx}\Delta s, \tag{4.4}$$

where ΔT is the energy loss and Δs is the step length. When the energy losses are larger, the calculation is based on the following equation

$$\Delta T = T_0 - f_T(r_0 - step), \tag{4.5}$$

where T_0 is the kinetic energy, r_0 the range at the beginning of the step, $f_T(r)$ is the *InverseRange* table and *step* is the step length. After this mean energy loss is calculated, GEANT4 calculates the actual energy loss with fluctuations (using a straggling function) for thick and thin absorbers separately.

4.4.2 Step-size limitation

Continuous energy losses can be considered more difficult to implement accurately. For energy losses above a user energy threshold the Möller and Bhabha scattering cross sections are used, but for energy losses below this threshold the approximations discussed above can give wrong results. Moreover, the Berger-Seltzer formula breaks down at energies below 10 keV. Because the cross section is energy dependent it is necessary to use small step sizes to avoid large variations of the cross section during a step. However, too small steps increase considerably the computing time. The solution to this problem is to introduce a lower limit to the step size. In the current GEANT4 implementation (Geant4 Collaboration 2010) a lower limit is imposed to the step size: the step size cannot be smaller than the range cut parameter set by the programme. This is controlled by a smooth *StepFunction*. At high kinetic energies the maximum step size is defined by *Step/Range* and is approximately equal to a user defined parameter called *dRoverRange*. A value *dRoverRange* = 0.1 means that the step size is not allowed

to decrease by more than 10% of the range. As the particle travels the maximum step size decreases gradually until the range at the beginning of the step is smaller than a user parameter called *finalRange*. Figure 4.3 illustrates this situation.

E_0 = 100 keV
E_{cut} = 254 eV
range = 7.8 mm
step max = 0.78 mm

E_k = 254 eV
range = 0.5 μm
final range = 1 μm
step max decreases
down to this point
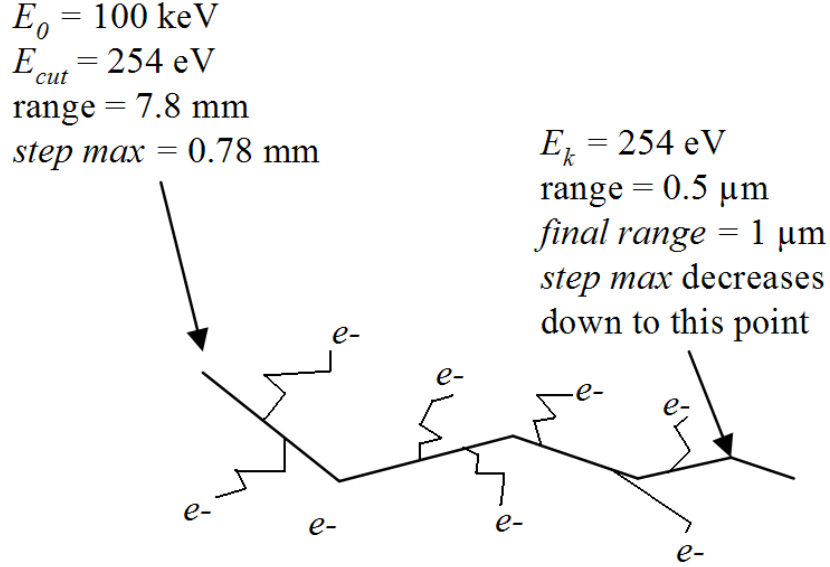
Figure 4.1: Secondary particle production in Geant4.

The step size gradually decreases while the primary particle slows down. Slowing down is achieved by the production of secondary electrons above the E_{cut} = 254 eV. A *dRoverRange* = 0.1 limits the maximum step size to 10% of the range of the particle and a value *finalRange* = 1 μm forces the maximum step to decrease according to (for ranges grater than *finalRange*)

$$\Delta S_{lim} = \alpha_R \, R + \rho_R \, (1 - \alpha_R) \left(2 - \frac{\rho_R}{R} \right), \qquad (4.6)$$

where α_R is *dRoverRange* and ρ_R the *finalRange*. When the kinetic energy of the particle finally reaches the user cut-off, the remaining energy is continuously deposited along the track.

4.4.3 Multiple scattering

The use of multiple scattering theories (Lewis 1950) in the Monte Carlo simulation of electron transport is mainly motivated due to the introduction of the Condensed History Algorithm (Berger 1963, Larsen 1992). As described in Section 4.4 at the end of a particle step the global effect of many collisions is calcu-

67

lated from multiple scattering theories. The correct implementation of multiple scattering in GEANT4 was an issue of interest after the publication by Poon *et al.* (2005). This publication reported inconsistency of the condensed history algorithm implemented in GEANT4, mainly, due to a poor simulation of electron transport and step size artefacts. It was noticed that GEANT4 was not optimized for medical physics simulations. Step size dependence, energy loss and multiple scattering models were revised and an improvement was recently reported (Elles *et al.* 2008).

An interesting discussion about the importance of an accurate Monte Carlo simulation of electron transport is given by Rogers (2006) and Rogers and Kawrakow (2003).

One of the most stringent tests to investigate the correct implementation of the electron transport algorithm in any Monte Carlo code is the simulation of an ionization chamber (Rogers 2006). The Fano theorem, which states the uniformity of the flux of secondary radiation in a medium, produced by a uniform flux of primary radiation, as independent of the density of the medium and its variation from point to point, is artificially used to force the equality of the stopping power in the wall and the cavity of an ionization chamber. This is achieved by ignoring the variation of the density correction in the stopping power. Charged particle equilibrium is established in the wall of the chamber, and the wall and cavity are made of the same material, but with different densities (usually 1000 times) to meet the requirements of the Fano theorem. Under these conditions, the ratio of simulated to theoretical (using the same data cross sections in the MC code) dose deposition in the cavity should be equal to unity. Any deviation from a unit ratio between these two quantities is attributed to the condensed history implementation of electron transport in the Monte Carlo code.

As stated by Rogers (2006) "the Fano cavity test is the most severe test applied to a Monte Carlo code because to obtain an accuracy similar to that achieved by EGSnrc the code must be capable to handle boundary crossing, backscattering and transport between interfaces of different media correctly".

The EGSnrc code was demonstrated to be consistent to its own cross section and independent of electron transport parameters within 0.1% (Kawrakow 2000).

The latest test performed on GEANT4 showed a consistency within 1.5%. This means that the accuracy of the GEANT4 implementation of the condensed history algorithm is accurate within 1.5%. In other words, GEANT4 results deviate from theoretically expected ones by 1.5%. A series of updated parameters were reported and recommended for accurate simulations in medical physics. Table 4.1 shows those parameters which were used in all Monte Carlo results presented in this thesis.

Table 4.1: Geant4 electron transport parameters.

Parameter	Default	Optimized
f_r	0.02	0.02
f_g	2.5	3.0
$skin$	0	2
α_R	0.2	0.01
ρ_R	1 mm	0.001 mm
ξ	0.01	10^{-6}

The correct simulation of particles crossing a boundary is handled by setting a parameter called *RangeFactor* (f_r). This parameter limits the maximum size of the step to a fraction of the particle mean free path or range according to $Step = f_r \times max(range, \lambda)$. This parameter is important to control the step size for very thin layers and is applicable while the particle is crossing a boundary.

When a particle is crossing an interface between two different media, the simulation of particle transport turns extremely complicated. This was discovered from investigations of ionization chamber response errors in the works by Nath and Schulz (1981) and discussed by Rogers (2006). The reasons behind these difficulties is now well understood and mainly because the multiple scattering theories used for condensed simulations were developed assuming an infinite medium. If a particle step from medium 1 (figure 4.2) traverses the interface in just one step the calculation of energy loss, lateral displacement and angular scattering would give incorrect results for the medium 2. To prevent a particle crossing a boundary in just one step, the parameter *GeomFactor* (f_g) was introduced. The step size is limited by $1/GeomFactor$ of the linear distance to the next geometrical boundary. This parameter is applied to ensure that a minimum number of steps are

computed in any volume independently of its thickness (important for very thin layers). Its counterpart in EGS4 is called the PRESTA algorithm developed by Bielajew and Rogers (2006).
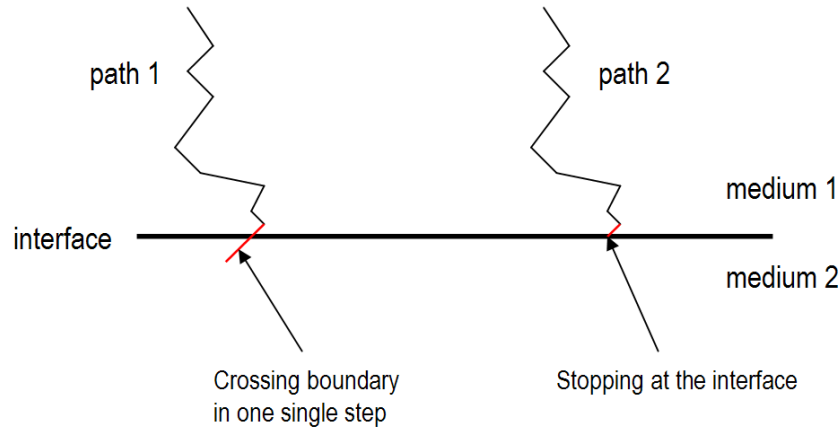
Figure 4.2: Boundary crossing in GEANT4: when a particle crosses an interface between two media in one step, the multiple scattering theory breaks down. This is illustrated by the path 1. A correct implementation does not allow a particle to cross a boundary in one single step. In path 2, the step ends just at the interface in medium 1. The MC code then starts a new step in medium 2 from where it samples lateral displacement, angular scattering and energy loss.

The parameter *skin* switches from multiple scattering to single Coulomb scattering when crossing a boundary in order to refine the calculation of the electron trajectory. The thickness of the layer in which single Coulomb scattering is applied is defined by ($\lambda \times skin$). It is supposed that the use of this parameter does not require further step-size limitation.

In the case of small steps, this computation can become unstable so it is replaced by a linear approximation in which the stopping power is assumed constant, the limit of this approximation is controlled by the parameter *linLossLimit* (it avoids the computation of energy loss to become unstable for small steps). Variations of stopping power along the step are taken into account from range and inverse range tables as discussed earlier. The approximation is $StepRange < linLossLimit$.

4.4.4 Energy cut-off

The selection of electron cut-offs is complex and depends on the simulation geometry, energy, type of particle and other factors (Rogers 1984). Unlike EGSnrc, GEANT4 tracks particle down to zero kinetic energy or until the particle leaves the simulation geometry. This approach is more accurate than discarding electrons with energy below the threshold because the latter could increase significantly uncertainties for dose calculation in voxels, mainly, in low density media (Li and Ma 2008).

GEANT4 defines production cut-offs, this is, secondary particles are produced above certain user-defined threshold. For therapy beams, the selection of electron cut-offs can be quite high since low-energy electrons contribute little to dose deposition in phantom. An established value in EGSnrc is 0.700 MeV ($\sim$ 3 mm). This allows an acceptable accuracy in dose calculation and sensible computing times. However, it is observed that computing time increases as the energy cut-off value decreases. This happens because more secondary electrons have to be produced and their energy sampled from the corresponding scattering cross sections.

A rule of thumb defined for calculations of dose distributions using EGSnrc is to choose the electron energy cut-off so that when expressed in terms of electron's range it is less than about 1/3 of the smallest dimension in a dose scoring region. These scoring regions are usually voxels in a water phantom of dimensions 1 mm^3. Therefore, a cut-off of 0.3 mm is required in voxelated geometries.

For thin layers the choice of the electron cut-off may not follow this simple rule. This is because in thin and very thin layers, energy deposition may be an issue. When the Monte Carlo code stops the production of secondary particle, the energy loss below the cut-off is either accounted for by assuming a continuous slowing down of the primary particle or deposited on the spot. This may result in overestimations as all the remaining energy which would have been carried away by producing secondary particles is deposited in a sensitive region of a detector. In general, energy cut-off selection is an issue that needs special attention.

4.5 Multiple scattering versus Coulomb scattering

4.5.1 Simulation methodology

To study the variations of energy deposition in thin layers when multiple scattering is used instead of a more accurate description given by the single Coulomb scattering process (Apostolakis *et al.* 2008), simulations consisting of 10^5 mono-energetic electrons normally incident on two layers of 14 μm and 1 mm were performed. These two thicknesses were chosen because the former is the actual thickness of the sensitive layer of the sensor while the 1 mm thick layer was chosen for comparison and to verify convergence between both processes for thick layers. Pencil beams of energies 0.1, 1 and 10 MeV were chosen. The total energy deposited in the layers resulting from simulations with the multiple and single Coulomb scattering processes were compared. In addition, we investigated the CPU performance since the simulation of every single interaction takes considerable time (Fernández-Varea *et al.* 1992).

4.5.2 Results

The results of energy deposited are shown in Table 4.2. The percentage difference of energy depositions were calculated with respect to the Coulomb scattering process.

Table 4.2: Comparison of energy deposited in a layer of 14 μm of silicon using multiple scattering (E_{ms}) and Coulomb scattering (E_{cs}) processes. The mean values are expressed with their corresponding standard errors. Percentage differences were calculated with respect to Coulomb scattering results using $(E_{cs} - E_{msc}/E_{cs}) \times 100$.

E (MeV)	Cut-off (MeV)	Energy deposited		Diff. (%)
		E_{msc} (MeV)	E_{cs} (MeV)	
0.1	0.000254	$181.1 \pm 3.1\%$	$175.1 \pm 3.0\%$	-3.4
	0.038390	$178.6 \pm 3.0\%$	$175.9 \pm 2.8\%$	-1.5
1.0	0.000254	$435.6 \pm 0.3\%$	$435.4 \pm 0.3\%$	0.0
	0.038390	$441.2 \pm 0.3\%$	$439.4 \pm 0.3\%$	-0.2
10.0	0.000254	$433.5 \pm 0.3\%$	$430.0 \pm 0.3\%$	-0.8
	0.038390	$434.2 \pm 0.3\%$	$433.9 \pm 0.3\%$	-0.1

Table 4.2 also shows that for a layer of 14 μm the energy deposited using multiple scattering is comparable to that obtained by setting the Coulomb scattering process. The percentage difference is below 1% for all energies except for 0.1 MeV where multiple scattering produces a higher result. This suggests that multiple scattering overestimates energy deposition at lower electron energies. However, it is necessary to keep the standard errors below 1% to suggest this. Nevertheless, both processes show larger fluctuations in energy deposition at lower energies. On the other hand, it was observed that the computing time increases by less than a factor 1.5 when Coulomb scattering was used. This was not observed at 0.1 MeV, in this case the computing time was larger by about a factor 3 when the simulations were performed using Coulomb scattering.

The situation was slightly different for the thicker layer. The percentage difference was below 1.5% for all energies, but the time increased significantly by a factor 7 at 0.1 MeV and by 15 at 1.0 MeV. These results are shown in Table 4.3 where electron transport was performed in the continuous slowing down approximation (CSDA) by setting a large cut-off value in energy.

Table 4.3: Comparison of energy deposited in a layer of 1 mm of silicon using multiple scattering (E_{ms}) and Coulomb scattering (E_{cs}) processes. The mean values are expressed with their corresponding standard errors. Percentage differences were calculated with respect to Coulomb scattering results using $(E_{cs} - E_{msc}/E_{cs}) \times 100$.

		Energy deposited		
E (MeV)	Cut-off (MeV)	E_{msc} (MeV)	E_{cs} (MeV)	Diff. (%)
0.1	0.000254	$9215.0 \pm 0.1\%$	$9141.0 \pm 0.1\%$	0.8
	CSDA	$9255.0 \pm 0.1\%$	$9160.0 \pm 0.1\%$	1.0
1.0	0.000254	$67820.0 \pm 0.1\%$	$67940.0 \pm 0.1\%$	-0.2
	CSDA	$69900.0 \pm 0.1\%$	$68810.0 \pm 0.1\%$	1.5

4.6 Influence of cut-off selection

4.6.1 Simulation methodology

To estimate the uncertainty introduced by using large cut-offs in comparison to the smallest one, simulations were performed with 10^4 mono-energetic electrons. The initial energy of the electrons was 0.350 MeV.

Four different cut-offs were selected, 0.1 μm (0.000100 MeV), 0.5 μm (0.000254 MeV), 1.0 μm (0.000853 MeV) and 568 μm (0.352 MeV). The largest cut-off ensured that no secondary particles were produced, therefore the energies of primary electrons were deposited continuously along the track.

The simulations were carried out by setting the electron transport parameters in Table 4.1. The initial seed of the random number generator was left to vary and 10 simulations were run to estimate the standard errors. By using these parameters the maximum step size is limited to 1% of the range of the particle (in contrast to the default value 20%). This maximum step size decreases gradually until the range is smaller than *finalRange* which is either 0.1 μm or 1 μm.

In addition, a similar simulation was carried out, but increasing the sensitive layer of the sensor by 10 (140 μm) for comparison. This aimed to investigate whether or not the cut-off dependence, if any, would be present in thicker layers.

4.6.2 Results

Table 4.4 shows the results of the energy deposited in the sensitive layer of the sensor (14 μm of silicon) as a function of the electron cut-off and the *finalRange*. A schematic representation is shown in figure 4.3.

Table 4.4: Comparison of energy deposited in a layer of 14 μm of silicon as a function of the electron cut-off and the *finalRange*. Results on the left side were obtained using *finalRange* = 1.0 μm while a value 0.1 μm was used for results showed on the right. The mean values are expressed with their corresponding standard error. The percentage differences were calculated with respect to the smallest cut-off using $[E(i) - E(0.0001)/E(i)] \times 100$ where $E(i)$ is the energy deposited at a cut-off i.

	Energy deposited			
Cut-off (MeV)	E (MeV)	Diff. (%)	E (MeV)	Diff. (%)
0.000100	98.1 $\pm$ 0.6%	–	98.6 $\pm$ 0.4%	–
0.000254	96.8 $\pm$ 0.3%	-1.4	96.7 $\pm$ 0.4%	-1.9
0.000853	94.7 $\pm$ 0.3%	-3.5	94.4 $\pm$ 0.4%	-4.3
0.352000	93.4 $\pm$ 0.6%	-4.8	92.9 $\pm$ 0.5%	-5.8

Two different analyses were carried out on these results. Firstly, it was investigated whether a reduction of *finalRange* from 1 μm to 0.1 μm would change the mean values of energy deposited. A Student's t test was performed. A Student's

t test allows the comparison of two samples when just an estimate of their standard deviations is known and enables one to say whether the average difference between these two samples is really significant or if it is merely due to random fluctuations.

The null hypothesis was that *finalRange* did not have any effect on the means obtained. Table 4.5 shows the results of this test. It is seen that all calculated critical values are smaller than the tabulated ones at a confidence level of 95%; therefore the null hypothesis cannot be rejected at this confidence levels. This is equivalent to saying that the differences observed in the means on Table 4.4 arose from statistical fluctuations.

After this verification, a second test was also performed to investigate the variation of energy deposited with cut-off.

Table 4.5: Student's *t* test results for the means of energy deposited shown on Table 4.4 for two different values of *finalRange*. The calculated *t* values originated after comparing both values of *finalRange* at the cut-off specified. The test was performed with 18 degrees of freedom; the significance of the test was at the 0.05 level.

	CSDA	853 eV	254 eV	100 eV
Confidence level (%)	95	95	95	95
Tabulated *t* value	2.101	2.101	2.101	2.101
Calculated *t* value	0.674	0.515	0.166	0.667
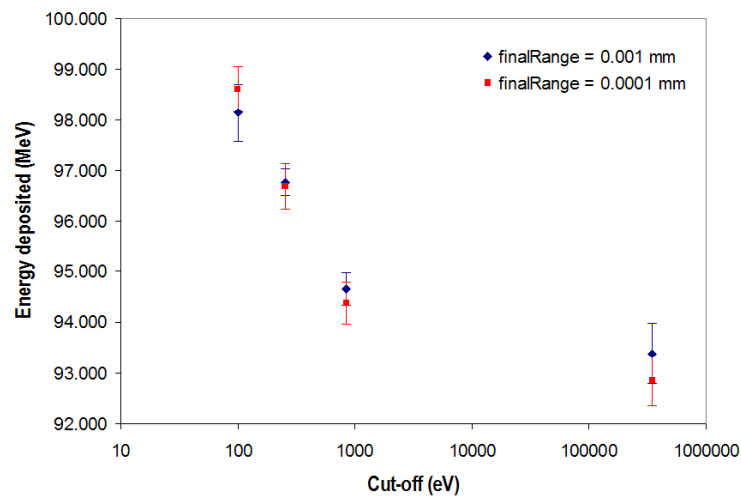
Figure 4.3: Schematic representation of the variation of energy deposited in silicon as a function of cut-off.

In this case the null hypothesis was that the differences observed did not depend on cut-off values.

Table 4.6: Student's *t* test results for the means of energy deposited shown on Table 4.4. The test was performed comparing the means of energy deposited at cut-offs 254 eV, 853 eV and CSDA with the smallest one (100 eV). The significance of the test was at the 0.05 level and 18 degrees of freedom.

	CSDA	853 eV	254 eV	100 eV
Confidence level (%)	95	95	95	–
Means (MeV)	93.389	94.660	96.772	98.132
SD (MeV)	1.856	1.007	0.819	1.768
SE(MeV)	0.587	0.318	0.259	0.559
Tabulated *t* value	2.101	2.101	2.101	–
Calculated *t* value	5.851	5.396	2.207	–
Null hypothesis	Rejected	Rejected	Rejected	–

Table 4.6 shows the results of the test. Because the calculated *t* values exceeded the tabulated ones the means are significantly different at the level specified by p = 0.05. Higher levels of significance (p = 0.01) also showed that there is a 99% probability of the means, for cut-offs 853 eV and CSDA, to be significantly different.

The next step was the investigation of cut-off artefacts on thicker layers to rule out the possibility of the effect occurring only on thin layers. The null hypothesis was the same as for the 14 μm silicon layer.

Table 4.7: Student's *t* test results for the means of energy deposited (not shown) in a layer of 140 μm of silicon as a function of cut-offs. The test was performed comparing the means of energy deposited at cut-offs 254 eV, 853 eV and CSDA with the smallest one (100 eV). The significance of the test was at the 0.05 level and 18 degrees of freedom.

	CSDA	853 eV	254 eV	100 eV
Confidence level (%)	95	95	95	–
Means (MeV)	1367.0	1392.3	1387.5	1389.5
SD (MeV)	3.8	2.7	2.7	2.8
SE(MeV)	1.2	0.8	0.8	0.9
Tabulated *t* value	2.101	2.101	2.101	–
Calculated *t* value	15.074	2.276	1.623	–
Null hypothesis	Rejected	Rejected	Accepted	–
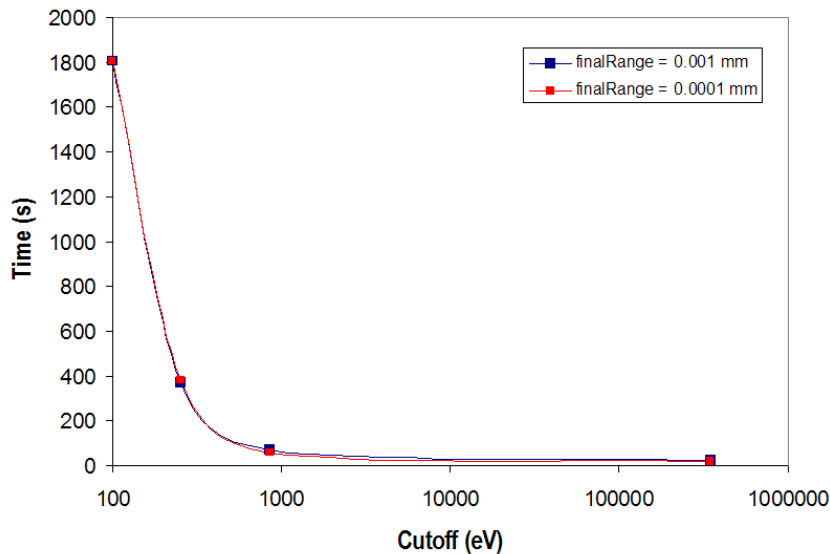
Figure 4.4: Schematic representation.

Table 4.7 shows the same test as presented in Table 4.6, but for a silicon layer 140 μm thick. At a cut-off of 254 eV the null hypothesis was not rejected because the calculated t value was smaller than the tabulated one, but for higher cut-offs the test is rejected. Results in Table 4.6 as well as 4.7 indicate that there is a strong dependence on cut-off which increases with higher values and thinner layers. Therefore, a cut-off of 100 eV is used for all simulations in this work.

Figure 4.4 illustrates how the computing time increases when the cut-off becomes smaller. The increase is significantly higher. Even a difference between a range of 0.1 μm and 0.5 μm increases the computing time by more than 4 times for both *finalRange* values. It is clearly seen that *finalRange* does not increase the simulation time.

4.7 Verification of cross sections data accuracy

4.7.1 Simulation and experimental methodology

It is well known that PENELOPE gives results comparable to those obtained with EGSnrc (Faddegon *et al.* 2009). This code uses numerical databases with analytical cross-section models for the different interaction mechanisms. In particular, low energy physics has been an important part of the development of this code. Therefore, PENELOPE has become an accurate and standard Monte Carlo tool

for medical physics applications. Consequently, all simulations presented in this work have been performed turning on the GEANT4 implementation of PENELOPE to allow for improved accuracy at low energies.

To quantify the degree to which this GEANT4 implementation can be considered reliable for this work comparisons of measured gamma-ray spectra with simulations were performed. Spectra from two low activity radionuclides were measured with an ORTEC high Purity Germanium (HPGe) detector and then simulated using GEANT4. Because of their availability and their gamma energy range ^{137}Cs and ^{60}Co were chosen. The simulation of the germanium detector consisted of a cylinder with a diameter of 36.0 mm and a height of 10.0 mm.

The incident spectra used in the simulations were generated according to the photon yield per energy (Knoll 1989) shown in Table 4.8.

Table 4.8: Data of simulated nuclides. I is the gamma ray photon yield per disintegration.

Nuclide	E (keV)	I (%)	Relative error (%)
^{137}Cs	31.8/32.2	5.64	2.0
	661.6	85.3	0.4
^{60}Co	1173.2	99.88	0
	1332.5	99.98	0

The interaction position was randomly selected using a GEANT4 random number generator engine while the particle direction was set up perpendicularly to the crystal surface. The number of particles per energy beam was chosen to produce enough interactions for the purposes of comparison with experimental measurements with the germanium detector and to give a relative error not greater than 2%. A cut-off of 250 eV was used for all simulations to obtain good accuracy. For each simulated radionuclide, an output file with the total energy deposited per photon interaction was obtained. With this information the histograms of energy deposition in the germanium crystal were plotted.

The Monte Carlo results were verified by calculating the maximum energy transferred to the electron using

$$E = h\nu \left(\frac{2h\nu/m_0c^2}{1 + 2h\nu/m_0c^2} \right).$$ (4.7)

The energy difference between the maximum Compton recoil electron energy and the incident gamma-ray energy was also verified and calculated from

$$E = h\nu - E_{e-}|_{\theta=\pi} = \frac{h\nu}{1 + 2h\nu/m_0 c^2}. \tag{4.8}$$

4.7.2 Results
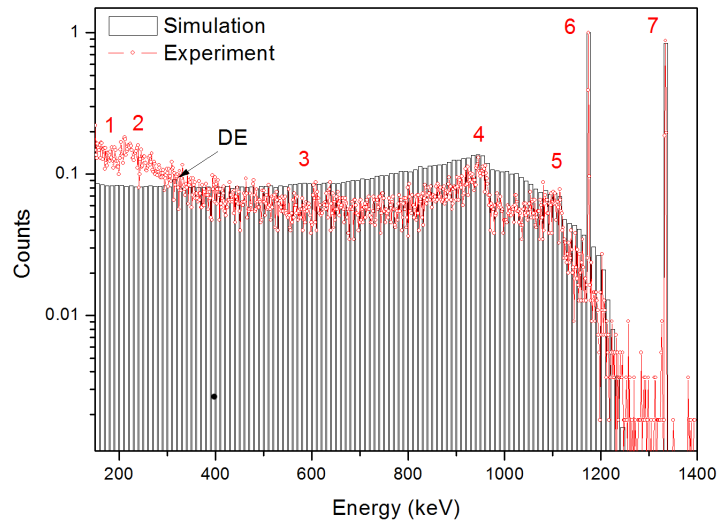
Figure 4.5: Comparison of simulated and experimental ^{60}Co spectra.

The measured and simulated ^{60}Co spectra are shown in figure 4.5 (the logarithmic scale in the vertical axis was used for clarity). The simulation shows an excellent agreement of the photopeaks that are located in the expected energy bins, the Compton edges were also reproduced from the simulation at both energies. Some typical characteristics of the measured ^{60}Co spectrum are described below:

1. Characteristic X-ray photopeak from shielding material: the photoelectric absorption in the shielding material creates characteristics X-rays that can reach the detector provided the atomic number of the shielding material is high enough to produce energetic X-rays.

2. Photopeak from the backscatter of gamma rays in lead shielding (mostly between 0.20-0.25 MeV): this photopeak is caused by gamma rays undergoing Compton interactions in the surrounding materials.

79

3. Compton continuum from the crystal and surrounding materials: a photon undergoing a Compton interaction can scatter at any angle, thus transferring to the electron energies between zero and a maximun energy when the scatter angle is $\theta = \pi$, which is known as the Compton edge. The energy distribution of the electrons is given by the Klein Nishina cross section.

4. Compton edges from the 1.17 peaks.

5. Compton edge from the 1.33 MeV peaks.

6. Photopeaks at 1.17 MeV.

7. Photopeak at 1.33 MeV.

The Monte Carlo results reproduced all these characteristics except the ones depending on the surrounding materials. Due to the noise associated to the measured spectrum it is difficult to make a comparison; however, a close observation of the spectra indicates that the energy gaps between the photopeaks and Compton edges are the same.

The contribution of Compton continuum is evident towards lower energies. A small peak at 311 keV (hidden by the experimental spectrum) in the simulated spectrum is the double escape (DE) peak due to annihilation radiation which is equal to the difference between 1.33 MeV and 1.02 MeV. The maximum energy transferred from a Comptom interaction when an 1173 keV gamma-ray arrives at the germanium crystal given by equation 4.7 is equal to 963 keV. The position of the Compton edge obtained from the simulation is located almost at the same value. For the 1332 keV gamma ray the predicted value of 1118 keV was exactly obtained from the simulation, as can be seen from figure 4.5.

Results for ^{137}Cs are shown in figure 4.6. A good agreement was observed for the location of the full energy peak, the Compton continuum and the Compton edge. The backscatter peak observed in the measured spectrum was produced by photon backscattering from the surrounding lead used to shield the detector. Multiple Compton scattering is observed between the photopeak and the Compton edge. This is not present in the simulation due to the small number of photon histories simulated and the logarithmic scale, but it can be seen from the original
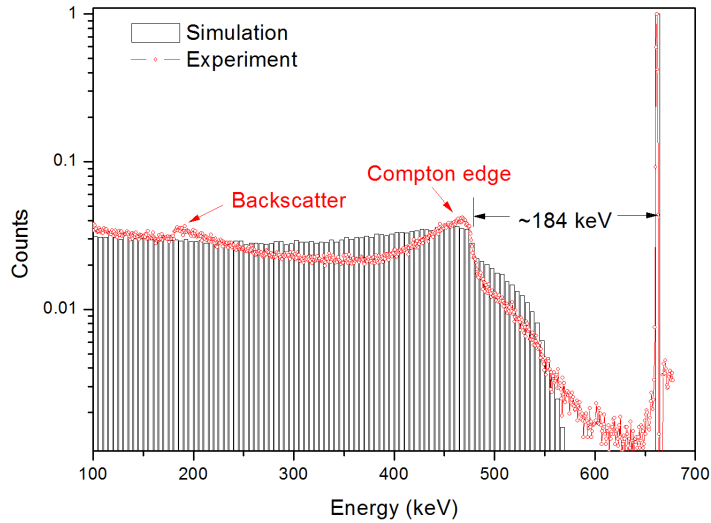
Figure 4.6: Comparison of simulated and experimental ^{137}Cs spectra.

data. Equations 4.7 and 4.8 were used to calculate the maximum energy transferred to the electron as well as the difference between the maximum Compton recoil electron energy and the full-energy peak, the theoretical values 478 keV for the maximum energy and 184 keV for the energy gap were exactly reproduced from the simulation as seen in the figure.

These results show that the PENELOPE electromagnetic models implemented in GEANT4 are reliable and in agreement with earlier validation studies of electromagnetic models (Amako *et al.* 2004). In the aforementioned investigation it was shown that the electromagnetic physics models developed for GEANT4 agree with NIST and ICRU cross section data within a 95% confidence limit. It is evident from this comparison that all energy peaks, the Compton edges and double escape peak agree between theory and experiment within 1%. However, these results are not a comprehensive validation of GEANT4 cross section data, but a verification of the model.

4.8   Simulation of the Vanilla sensor

The detector was defined from simple cubic volumes and surrounded by a mother volume of the same geometry. It was constructed by instantiating a GEANT4 C++ class called *DetectorConstruction*. Physics processes take place inside this

volume and it defines the system of coordinates for the simulation. Particles were only tracked in the mother volume and not when leaving it. As for any volume a material must be associated, the mother volume was filled with vacuum to stop the tracking process and therefore save CPU time. Once the detector was placed inside the mother volume, the origin of coordinates was inherited by the detector.

The kinematics of the simulation were carried out in the class *PrimaryGeneratorAction.* In this class, types of particles, energy, direction and interaction point of the primary particles can be specified. However, two different classes were used instead of the Geant4 class *PrimaryGeneratorAction.* *G4GeneralParticleSource* is a class developed and supported by QinetiQ and available free for download from http://reat.space.qinetiq.com. This class is useful because it readily allows the specification of the spectral, spatial and angular distribution of the primary source particles by using simple commands from macro files, thus avoiding multiple compilations of the source code. To read linear accelerators phase-space files the class *G4IAEAphspReader* was also instantiated. This class was developed and is supported by the IAEA NAPC Nuclear Data Section and can be downloaded from http://www-nds.iaea.org/phsp/Geant4/.

Physics processes were defined in a class called *PhysicsList.* In this class all particles were defined; primary and any secondary particles produced by interactions. Physics processes were included in this class. For electromagnetic processes particular models were defined for gamma interactions (e.g. Comptom, photoelectric effect, etc.) and electrons and positrons (ionization, bremsstrahlung, multiple scattering, etc.).

All simulations were performed using GEANT4 9.2. Physics models were based on the GEANT4 implementation of PENELOPE.

The sensor was modelled as a layered detector consisting of six different layers and the PCB material. A diagram of the detector is depicted in figure 4.7. Table 4.9 shows the composition and thicknesses of the layers used in the Monte Carlo model according to information provided by the developers of the sensor. The substrate differs from the epitaxial layer in that the former is a low-resistivity silicon layer which is the standard silicon starting wafer. The sensitive layer of the detector was divided in voxels of area $25 \times 25\ \mu m^2$ and height $14\ \mu m$ to resemble
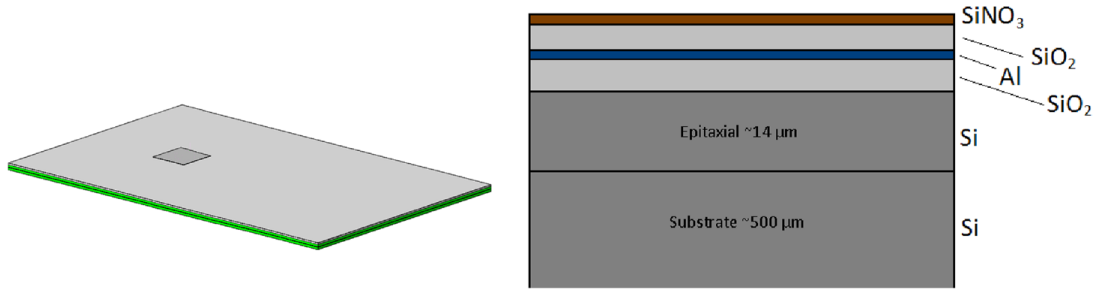
Figure 4.7: Monte Carlo model of the CMOS sensor. The sensor is the square shown in dark gray, while the other structure depicts the PCB (a). Illustration of the different layers comprising the sensor (b).

Table 4.9: Composition and thickness of the layers simulated in the model of the sensor.

Layer	Composition	Thickness (μm)
Pasivation	SiNO$_3$	1
Silicon dioxide	SiO$_2$	4
Aluminum	Al	1
Epitaxial	Si	14
Substrate	Si	500
PCB	SiO$_2$ (70%)	1664
	C$_{15}$O$_2$H$_{16}$ (23%)	
	C$_3$H$_6$O (7%)	
Copper in PCB	Cu	35

the pixel pitch of the real sensor. Energy deposited was scored in 270400 voxels in the sensitive layer of the detector.

4.9 Interpretation of Monte Carlo estimates

As mentioned earlier in this chapter the Monte Carlo method is a numerical stochastic procedure. The stochastic nature of the method itself comes, sometimes, from the problem to be solved. Therefore, a Monte Carlo result will tell us nothing if it is not quoted along with an uncertainty.

The law of large numbers of probability theory is a strong mathematical theorem that ensures convergence of the mean of a random variable to its expected value as the number of identically distributed, randomly generated variables increases, $N \to \infty$. In addition, a much stronger mathematical statement is the central limit theorem which states that as $N \to \infty$ the expected value of a ran-

dom variable follows a Gaussian distribution. This suggests that it is possible to make the uncertainty on the mean of a quantity as small as we wish by increasing N asymptotically. The efficiency of a Monte Carlo calculation is, therefore, proportional to $1/N$. As N increases, the computing time also increases. In general, this efficiency, ϵ, is defined as

$$\epsilon = \frac{1}{\sigma^2 T}, \qquad (4.9)$$

where T is the CPU time required to obtain a variance σ^2. The efficiency can be improved by decreasing the simulation time. This is however, difficult to accomplished. Conversely, a reduction of variance would require a large simulation time.

Calculation of dose in radiation therapy requires a large amount of computing time or the use of variance reduction techniques due to the low uncertainties required. For the simulation of thin-layer detectors, however, the probability of interaction is small and considerable CPU time is required. Under this situation it is important to establish a desired level of accuracy to estimate the CPU time required to obtain it.

Due to the low efficiency involved to estimate Monte Carlo quantities when simulating thin detectors, all Monte Carlo results presented in this work are calculated along with their corresponding standard errors which were found by repeating simulations N times. However, alternative methods have been developed to overcome this limitation (Sempau and Bielajew (2000)). The following formula has been used to calculate Monte Carlo uncertainties:

$$s(x) = \frac{\sigma(x)}{\sqrt{N}} = \sqrt{\frac{1}{N(N-1)} \sum_i (x_i - \bar{x})^2} \qquad (4.10)$$

in which x_i is the nth random variable, σ is the standard deviation and N is the number of simulations.

4.10 Discussion

The GEANT4 Monte Carlo code extension for medical physics can be considered as relatively new, however a significant effort has been made through the GEANT4

Collaboration and users worldwide to improve its accuracy. At the moment the accuracy of GEANT4 is still improving and lower than EGSnrc which is regarded as a gold standard code for medical physics applications. As reviewed in this chapter GEANT4 shows a consistency with its cross section data within 1.5%, which is significantly lower than that achieved with EGSnrc. Nevertheless, all the published works in many different fields, including medical physics, suggest that this will not be a major limitation in forthcoming releases.

In section 4.4 the GEANT4 electron transport algorithm was reviewed. A significant improvement has been made compared with previous versions. However, this algorithm is complex and tuning all the parameters to obtain an acceptable accuracy for medical applications is required.

The effect of cut-off selection on energy deposition in GEANT4 simulations has not been reported in the literature. The results presented in this work showed that even for a cut-off as small as 0.853 keV the discrepancy with the smallest cut-off is as high as 3.5%. For MV energies a cut-off dependence is likely to be less significant because the photon and electron mean energies at depths greater than the depth at dose maximum for MV energy spectra increase (and also with smaller field sizes) (Heydarian *et al.* 1996); therefore, for small fields where there is a reduced scatter with depths as well as a smaller low-energy photon contribution, GEANT4 cut-off dependence may be less significant.

GEANT4 cross section data for electromagnetic processes (photoelectric, Compton, gamma conversion) have been widely validated against reference data such as NIST and ICRU showing that the cross sections of all GEANT4 photon models are in statistical agreement (Cirrone *et al.* 2010). This was indirectly verified in figures 4.6 and 4.5 where MC simulations were compared against experimental spectra, giving results with agreement better than 1%.

Chapter 5

Energy response of CMOS APS: experimental and Monte Carlo investigation

5.1   Overview of chapter

In the present chapter the response of the CMOS sensor to MV energies is investigated with the Monte Carlo method. The spatial response of the sensor is computed by generating kernels that describe the deposition of energy across the pixel array from an interaction point. The description here follows the work by Keller *et al.* (1998). The generation of these kernels is a valuable method for understanding how energy is distributed across the sensor array.

The second investigation presented in this chapter is the Monte Carlo simulation of the response of the sensor as a function of depth in Perspex compared with the response in the medium without detector at the same depths. These comparisons are made through percentage depth curves (PDDs). Finally the response of the sensor to kilovoltage energies is measured experimentally with a X-ray machine.

5.2 Investigation of the response of the Vanilla sensor to MV energies

5.2.1 Spatial response of sensor

The effect of a detector size when measuring dose profiles of small fields is an issue because the dose may be underestimated. As a result, there is an impact on the dose delivered to organs at risk. Some investigators have calculated detector response functions or extrapolated detector size to zero to correct for detector response. Convolution methods are then applied.

Dose profile measurement is highly important for small-field dosimetry and therefore stereotactic radiosurgery (SRS) because high doses delivered in one fraction put strict limits on the geometric accuracy of dose delivery (Pappas *et al.* 2008). Detector volume averaging and loss of charged particle equilibrium introduce dosimetric uncertainties that affect the overall clinical treatment (Das *et al.* 2007, Fu *et al.* 2004). Laub and Wong (2002) found local discrepancies of more than 10% between calculated cross-profiles of intensity modulated beams and intensity modulated profiles measured with film. Experimental and theoretical techniques have been devised to correct the response of detectors; one of them, the kernel superposition approach.

A kernel, in dose calculation, represents the energy transport and dose deposition of secondary particles from an interaction point, where the point is the origin of coordinates of the kernel. The approach follows the concepts of image formation. García-Vicente *et al.* (1998) presented an experimental method for the determination of the spatial convolution kernel of detectors to describe the effect of the finite size of any detector as the convolution of this kernel with a dose profile. Zhu (2010) has reviewed the application of convolution kernels in small-field dosimetry.

Because of the presence of electron disequilibrium due to large dose gradients that exist in a radiation field, the dosimetry in small fields can result in significant uncertainties. Further complications arise from the introduction of radiation detectors in the medium of measurement, which usually perturbs the electron fluence. CMOS imaging sensor are not tissue equivalent and their volume may

introduce uncertainties that need to be corrected for. A detector's kernel can be generated using Monte Carlo techniques, and a sum of monoenergetic kernels weighted according to the incident photon spectrum can be used to derive polyenergetic kernels (Ahnesjö 1989).

Depending on the formulation of the dose equation (and the kernel) the dose in a detector can be considered as the convolution of an incident photon energy fluence with an appropriate kernel. From the detector's point of view the dose in a pixel j at $\mathbf{r}$ is given by the following convolution equation

$$D(\mathbf{r}) = \int_E \iiint_V \Psi(E, \mathbf{s}) h(E, \mathbf{r} - \mathbf{s}) d^3\mathbf{s} \, dE. \tag{5.1}$$

This is a different definition from that involving terma (total energy released per mass from the primary photon fluence $\Psi(E, \mathbf{s})$ in a differential volume $d^3\mathbf{s}$) and is valid provided the kernel is appropriately normalized. In equation 5.1 it is assumed that the kernel is spatially invariant and that the kernel axis is parallel to the central axis of the incident photon beam, therefore we are implicitly ignoring any effect that can arise due to the fact that the kernel axis may be tilted.

The interaction of the incident photon fluence can take place anywhere along the central axis of the sensor in the sensitive layer as well as in the silicon dioxide and substrate layers. Therefore, for the validity of this formulation it is assumed that the interaction occurs at an entrance plane with coordinates given by a vector $\mathbf{s}$ and that the energy is deposited at $\mathbf{r}$ in the sensitive volume, thus the kernel represents the absorbed dose per energy unit at $\mathbf{r}$ per incident photon in $\mathbf{s}$ with energy E . From these assumptions the integral in equation 5.1 can be expressed as a surface integral (Keller *et al.* 1998)

$$D(\mathbf{r}) = \int_E \iint_S \Psi(E, \mathbf{s}) h(E, \mathbf{r} - \mathbf{s}) d^2\mathbf{s} \, dE. \tag{5.2}$$

When the photon beam consists of a spectral distribution of n monoenergetic beams with energy E_i and weights w_i, satisfying $\sum w_i = 1$, equation 5.2 becomes a sum of n convolution operations of each energy fluence element incident on a pixel $\Psi(E_i, \mathbf{s})$ with the corresponding monoenergetic kernel $h(E_i, \mathbf{r} - \mathbf{s})$. This

procedure is repeated for all pixels to produce a final image. This leads to an equation of the form

$$D(\mathbf{r}) = \sum_{i=1}^{n} D(E_i, \mathbf{r}). \tag{5.3}$$

For a detector array the deconvolution of an image would require a considerable amount of time. By assuming a polyenergetic kernel the time per iteration can be significantly reduced.

To derive an expression for the polyenergetic kernel the detector is considered to be in air and that an energy fluence is incident in its central axis.

We first rewrite equations 5.2 and 5.3 for the ith monoenergetic beam as

$$D(E_i, \mathbf{r}) = \int_S \Psi(E_i, \mathbf{s}) h(E_i, \mathbf{r} - \mathbf{s}) d^2\mathbf{s}, \tag{5.4}$$

where $\Psi(E_i, \mathbf{s})$ is the energy fluence of the monoenergetic beam with energy E_i and $h(E_i, \mathbf{r} - \mathbf{s})$ is the monoenergetic kernel.

The monoenergetic kernel can be expressed as

$$\int_S h(E_i, \mathbf{r}) d^2\mathbf{s} = \frac{D(E_i)_{tot}}{\Psi(E_i)}. \tag{5.5}$$

For the validity of the kernels in 5.5 it is assumed that the kernels were produced by considering a large number of incident monoenergetic beams such that the quotient in 5.5 tends to its expected value, then it follows

$$h(E_i, \mathbf{r}) = \frac{D(E_i)_{tot}}{\Psi(E_i)} \tilde{h}(E_i, \mathbf{r}), \tag{5.6}$$

where $D(E_i)_{tot} = \sum D(E_i, \mathbf{r})$ is the total dose deposited in the array by the i-th monoenergetic beam and $\tilde{h}(E_i, \mathbf{r})$ is the normalized kernel which, as discussed by Keller *et al.* (1998), contains the scattering information of the medium represented by its lateral dose distribution. This kernel follows the normalization condition $\sum \tilde{h}(E_i, \mathbf{r}) = 1$.

By considering a weighted sum of all monoenergetic kernels we can derive an

expression for the polyenergetic kernel:

$$h_{poly}(\mathbf{r}) = \sum_{i=1}^{N} w_i \frac{D(E_i, \mathbf{r})}{\Psi(E_i)}, \tag{5.7}$$

where $w_i = \Psi(E_i) / \sum \Psi(E_i)$. The convolution equation with the polyenergetic kernel can now be written as

$$D_{poly}(\mathbf{r}) = \sum_{i=1}^{N} \Psi(E_i) \left(\sum_{i=1}^{N} w_i \frac{D(E_i, \mathbf{r})}{\Psi(E_i)} \right). \tag{5.8}$$

5.2.2 Monte Carlo generation of kernels

The polyenergetic kernels following equation 5.7 were generated from a 6 MV photon spectrum of a Varian Clinac iX (Hedin *et al.* 2010) normalized to 1×10^9 particles. Two kernels were computed, one assuming the sensor in air and another one in a Solid Water phantom as in the simulation set-up shown in figure 5.1 in which the sensor is embedded in a Perspex slab. Two Solid Water slabs were used as buildup (5 cm) and to provide scatter radiation (10 cm) respectively.

Because of the low interaction probability in the sensitive layer of the sensor due to its thickness (14 μm) the simulation to generate the kernel in air was repeated 10 times and then averaged. This simulation was performed on the UCL Legion cluster where n jobs were submitted as energy bins in the spectrum. The Penelope package implemented in GEANT4 was used for the simulations. Electron transport parameters were set as described in Table 4.1. The kernel was generated from an output file containing energy deposited and the corresponding coordinates of the pixels in the array. The files were processed to obtain two kernels in the form of matrices of 520 $\times$ 520 pixels using Matlab.

For each energy bin from the incident spectrum (figure 5.2) the energy deposited in each pixel was converted to dose in silicon by dividing it by the mass of the pixel. To obtain the polyenergetic kernel in units of dose per energy fluence [Gy MeV^{-1} cm^2], the dose in each pixel was divided by the incident photon fluence.
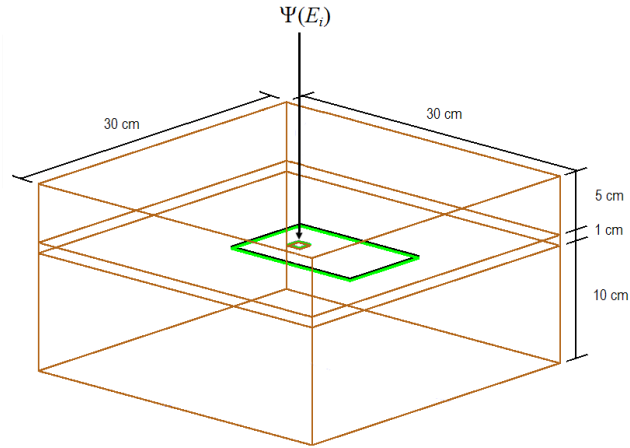
Figure 5.1: Schematic representation of the experimental setup used for the Monte Carlo generation of the polyenergetic kernel. The sensor is placed at a fixed depth of 5 cm aligned with the beam axis. Solid Water slabs of 5 and 10 cm were used as buildup and scatter material.

5.2.3 Results

Figure 5.3 shows the one-dimensional profile plotted across the central axis of the pixel array.

The kernels look very noisy because of the limited number of particles used for the simulations, the low interaction probability in 14 μm of silicon and the fact that the kernels were taken from the average of four rows of pixels. From figure 5.3 it is seen that at a lateral distance equal to 10 pixels from the central axis (250 μm) the energy deposited drops 400 times when the sensor is at 5 cm depth in the phantom. When the sensor is in air most incident photons deposit energy in the central pixel, this is seen because the energy drops by more than 10000 times from that deposited in the central pixel. This is due to the low photon and electron scattering probability in the lateral direction.

Figures 5.4 shows the dose deposited in the sensor per unit photon and energy fluence from the spectrum in figure 5.2 respectively. There is a high probability of energy deposition for low-energy photons because of the photoelectric absorption. The dose per photon fluence graph in figure 5.4 shows that higher energy photons deposit dose more efficiently in the sensor array. Dose deposition per unit of energy fluence does not change significantly with the incident spectrum.

To investigate how the energy is deposited across the sensor array the fraction
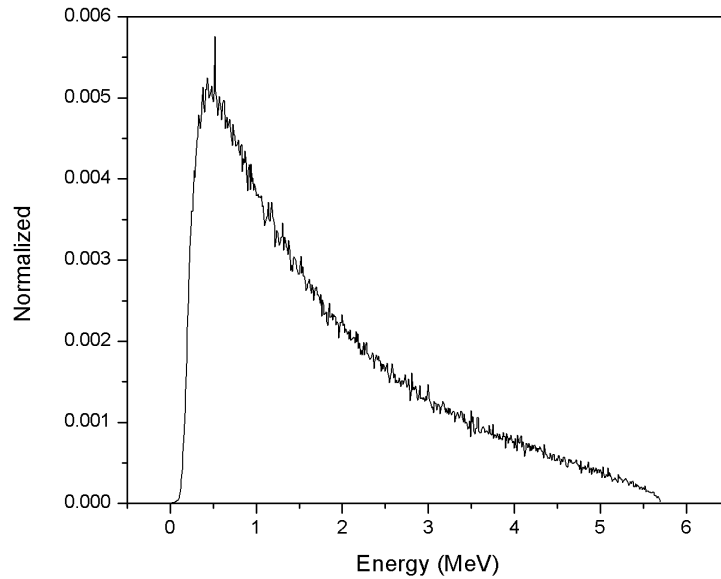
Figure 5.2: 6MV photon spectrum used for the generation of the kernels.

of energy deposited was calculated for concentric circular clusters. Figure 5.5 shows the fraction of energy deposited as a function of the cluster diameter. This energy fraction represents the fraction of the total incident energy collected in a region surrounding the central pixel normalized to the total energy deposited in the array. About 94% of the total energy deposited in the whole array is concentrated in a cluster of 1 mm of diameter when the sensor is placed in air. This fraction is reduced to 38% when the sensor is inside the water phantom. This additional energy spread is due to the scattering produced in the phantom.

5.3 Response of sensor in Perspex: Monte Carlo investigation

The response of the silicon detector was investigated in a Perspex phantom and compared with dose values in the medium at the same positions. For this simulation a Monte Carlo-generated 6 MV spectrum of a Varian Clinac iX was used (more details are given in chapter 6). At the moment of this simulation the GEANT4 phase-space file reader was not correctly integrated in GEANT4; therefore an alternative method was used to obtain the spectrum data in a histogram form. This histogram (energy bins and counts) was used as an input beam in the
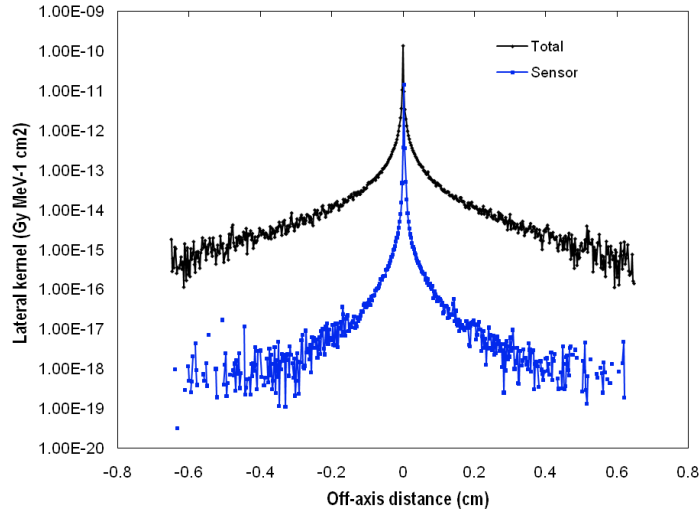
Figure 5.3: Lateral profiles across one row of pixels in the centre of the polyenergetic kernels.
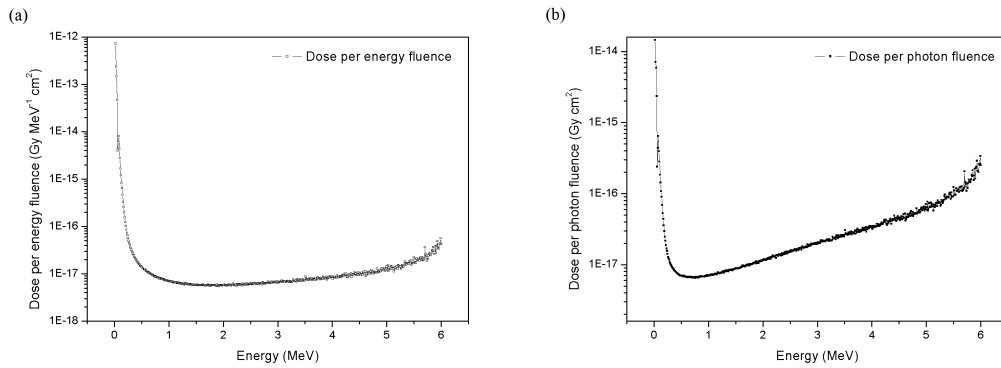
Figure 5.4: Dose per energy fluence and dose per photon fluence across the sensor array.

Monte Carlo simulation. The G4GeneralParticleSource C++ class (GPS) was used to specify the input beam. A 10 cm square field and a uniform spatial distribution were set (unidirectional angular distribution and 2D spatial sampling). The dose was scored in the sensitive layer of the sensor to obtain dose in silicon. A cylinder was used to score the dose in the medium. These dose values produce percentage depth dose curves (PDD) which were compared.

5.3.1 Results

Figure 5.6 shows the results of PDD curves simulated in the sensor and the Perspex phantom. The PDD curves comparison shows differences between 5 and 6%. However, the normalized curves are in good agreement. The agreement is equal
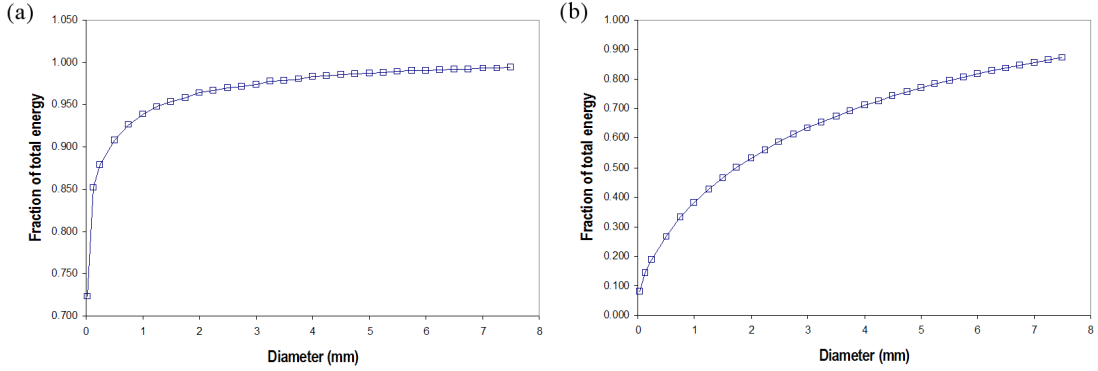
Figure 5.5: Fraction of energy deposited in circular clusters surrounding the interaction pixel. Graph (a) is due to the sensor. Response of sensor in the Solid Water phantom (b).

or better than 1% except for the PDD value at the surface, which is dependent on how well GEANT4 deals with backscatter. It is observed that the dose maximum occurs at about 1.8 cm deep in both silicon and Perspex, which is slightly greater than the depth of dose maximum in water. These results show that the silicon sensor can be used for reliable PDD measurements because its dose response with depth is proportional to that in the medium. In chapter 7 this investigation is extended to Monte Carlo simulations of TPR, where the Monte Carlo spectrum has the actual machine spatial and angular distribution from the phase-space file.
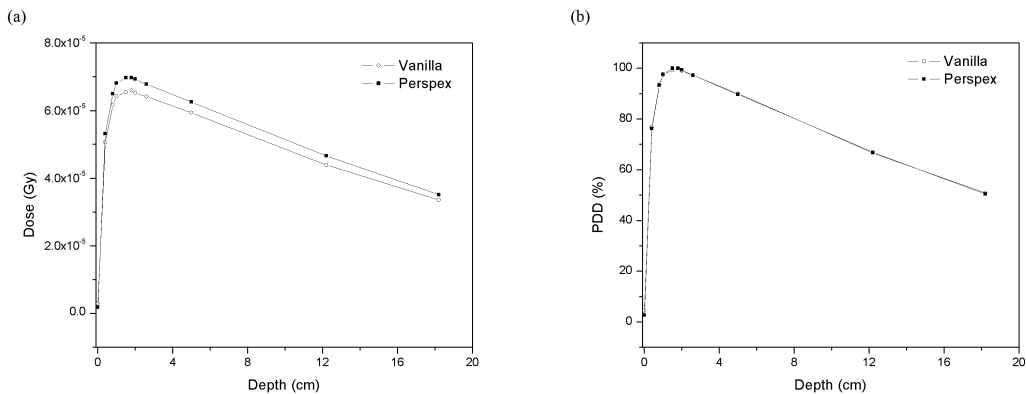
Figure 5.6: PDD curves simulation, with the Vanilla sensor and in the medium.

5.4 Investigation of the response of the Vanilla sensor to kV energies

The response of the Vanilla sensor to kilovoltage energies was investigated by irradiating the Vanilla sensor with an AGO HS-MP1 industrial X-ray machine with 1 mm Al inherent filtration and tungsten anode. The X-ray generator used for these measurements was a constant potential single phase high frequency generator (Model UF160/0 driven at 25 kHz, with no full well rectification and with a ripple factor less than 2%).

The sensor was operated under low levels of light sources. An offset correction was performed by averaging 100 irradiated frames and subtracting the dark image. The sensor was placed 120 cm from the X-ray source anode and perpendicularly to the beam direction.

After irradiations, the frames were automatically transferred to the PC to be analyzed using Matlab™. The total and the average digital numbers (DN) per averaged frame (at a particular kV) were obtained. Measurements were also performed with an ionization chamber.

5.4.1 Results

Figure 5.7 shows the response of the ionization chamber (μGy/s) as a function of the kilovoltage energies. The ionization chamber responds linearly over the range of kV energies. Figure 5.8 shows results of the response of the Vanilla sensor to the same beam for several integration times from about 40 ms to 1.03 s. A square-root relation observed between the sensor mean signal and the voltage shows that this nonlinearity increases slightly with the integration time, presumably, due to a dark current contribution. This square-root relation does not arise from the fact that the amount of radiation produced is approximately proportional to the KV squared, but to the response of the sensor itself. This is verified from figure 5.9 where the sensor was exposed to a constant kV energy and a varying tube current. The same behaviour is observed on the left hand side graph, while the graph obtained for 67.4 ms is almost linear with the tube current due to the low integration time and consequently a low dark current. From these results it can be concluded that the sensor nonlinearity discussed in Chapter 3 (V/V and V/e$^-$

nonlinearities), which arises at higher signal levels, is causing this over-response. However, PTC analysis allows the correction of this nonlinearity by converting the mean signal from DN to e^- units.
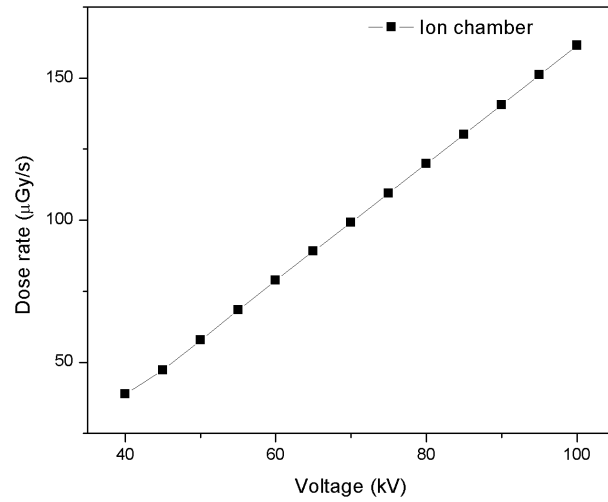
Figure 5.7: Dose rate in air measured with the ionization chamber at 120 cm from the anode for several kV energies at 1 mA.
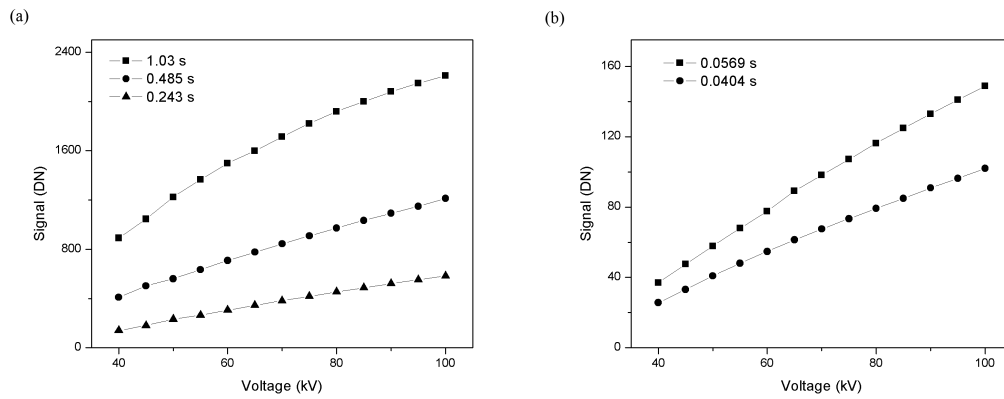
Figure 5.8: Sensor mean signal as a function of the kV energies at 1 mA.
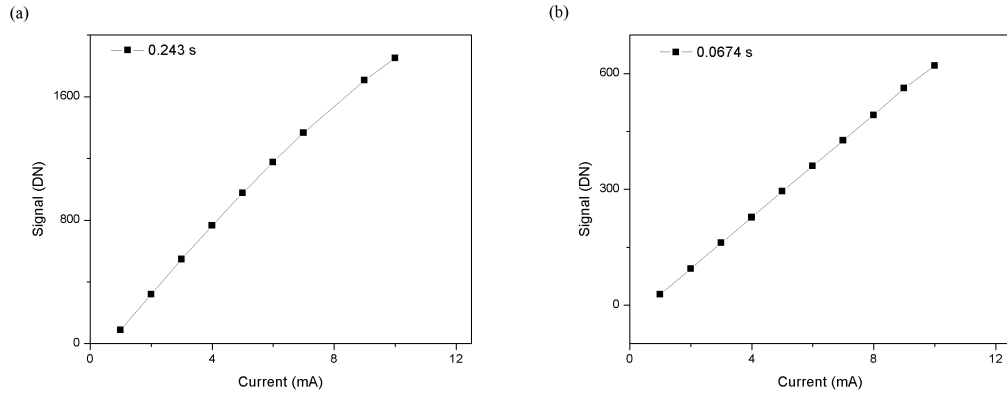
Figure 5.9: Sensor mean signal as a function of the current in the X-ray machine at a constant kilovoltage.

5.5 Dose rate dependence measurements

It is known that cumulative radiation damage to silicon semiconductor diode detectors can induce dose-rate-dependent sensitivity, a concern for the pulsed radiation of linear accelerators (Wilkins *et al.* 1997). It is important to characterize the dose-rate dependence of detectors because their response can vary with dose rate at different source-detector distance (SDD) (Saini and Zhu 2004).

The Varian Clinac 2100CD delivers pulsed radiation at a constant dose per pulse. The calibration of the machine was such that 100 MU/min corresponds to 1 cGy/MU at 5 cm deep (95-cm SSD) in water for a 10 cm square field. For dose rate dependence measurements a regular sequence of pulses was required to make sure that the sensor was irradiated at equal number of pulses during signal integration. The machine was operated at a constant dose rate of 100 MU/min. This value was a trade-off between dose rate and integration time to avoid sensor saturation.

Provided the source-surface distance is chosen to be large, the finite size of the radiation source of a linear accelerator becomes unimportant in relation to the variation of photon fluence with distance. Thus the dose rate can be considered to vary inversely as the square of the distance. The dose-rate dependence was measured by varying the source-to-surface distance (SSD), utilizing the inverse square law without modifying the linac running parameters. The detector was placed at the central axis of the beam at 100 cm and 200 cm from the source and

97

embedded in Perspex (1 cm thick). Slabs of Solid Water were placed on top (4 cm thick) to obtain a buildup of 5 cm to eliminate electron contamination. 10 cm of Solid Water was used for backscatter. Exposures of 100 MU/min were delivered with a 10×10 cm^2 field with a 6 MV beam. Measurements were made with a 0.6 cm^3 Farmer ionization chamber, at the same geometry, for comparison.

To quantify dose rate dependence the sensitivity of the Vanilla sensor was calculated at 100 and 200 cm. The sensitivity was defined as the charge collected in the sensitive layer of the sensor per corresponding unit dose to the ionization chamber (e$^-$/mGy). This charge was integrated during 19.5 ms and averaged over 500 frames.

5.5.1 Results

Table 5.1 provides measured results for the sensitivity of the Vanilla sensor at 100 and 200 cm from the source. The signal in DN was converted into e^-. The sensitivity was calculated with respect to dose to water, otherwise the result would be a constant value, which would not give information of dose rate dependence. From Table 5.1 it is seen that the ratio of dose measured with the ionization chamber at 100 and 200 cm is about 4.0 while the same result calculated from the Vanilla signal gave 3.8, which indicates that the sensor presents some dose rate dependence. This is also observed by comparing the sensitivities; the sensitivity increases by 5% with depth.

Table 5.1: Sensitivity of the Vanilla sensor defined as the signal in electrons per dose to water measured with a Farmer ionization chamber.

Distance (cm)	Signal (DN)	Signal (e^-)	Dose IC (mGy)	Sensitivity (e^-/mGy)
100	678	12243±1.5%	152	80±1.2%
200	180	3216±1.5%	38	84±1.3%

5.6 Discussion

Kernel computation

The kernels in figure 5.3 show the theoretical spatial response of the CMOS sensor. Due to the thin sensitive volume most of the energy deposited by an

incident spectrum perpendicular to the surface remains in the central axis. The results show that when the sensor is in water at 5 cm deep the energy drops by about 400 times at a distance of 250 μm from the central axis, but when the sensor is in air the energy at the same lateral distance drops by more than 10000 times. This is quite beneficial when measuring beam profiles because the broadening of the penumbra is negligible, therefore beam profile measurement with this sensor does not require the corrections mentioned earlier in this chapter. There is no need for extrapolation to zero size or the determination of detector size effect through deconvolution methods (Laub and Wong, García-Vicente *et al.* 2003, García-Vicente *et al.* 2005). It is interesting to see how the dose per energy fluence and per photon fluence are deposited across the sensor array. It is observed that most of the dose deposited in the sensor is due to the high-energy part of the photon spectrum. This result can be useful for optimization of sensor design.

Figure 5.5 shows that 94% of the total energy deposited in the sensor array is confined in nearly 0.6% of the total area of the sensor. However, these Monte Carlo results do not take into account the spread of electrons due to diffusion. Because the depletion region does not extend fully into the epitaxial layer, the electric field is negligible in the epitaxial layer meaning that electrons will not drift in it. Diffusion is the way charge is collected in CMOS image sensors; in other words, diffusion due to the potential wells created in the sensor volume will spread a little further the electrons created in the sensor after the interaction of radiation, which in turn will modify the actual spatial response of the sensor. Nevertheless, this results give a good insight of dose deposition across the sensor array.

Response in Perspex

The response of the sensor in Perspex investigated through PDD curves simulations in figure 5.6 suggests that the actual sensor is capable of measuring PDD or TPR (Tissue Phanton Ratio) curves and partially validates the accuracy of the Monte Carlo model of the sensor.

Response to kV energies

Figure 5.8 shows that the response of the sensor to kV energies is affected

by the inherent nonlinearities present in CMOS sensors (Janesick 2007). It is also seen that the larger the integration time, the higher the nonlinearitiy, which increases with signal as discussed in section 3.7.

Dose-rate dependence

In this work it has been assumed that if the accelerator output (dose/MU) does not vary with average dose rate, the sensor signal/MU should be a good indication of dose rate dependence. This was confirmed experimentally from Table 5.1 where it is shown that the ionization chamber measurements are independent on dose rate. However, results presented in this chapter suggest that the Vanilla sensor signal depends on dose rate. There is an increase in sensitivity by 5%, which is quite significant.

The main material in CMOS active pixel sensor is silicon. Inside CMOS sensors diodes are formed, as discussed in Chapter 3, which allows the application of the same theory used to explain charge collection by diode detectors. However, in CMOS sensors the sensitive layer is field free, the holes produced diffuse until they reach the p+ substrate, while the electrons diffuse until they reach a pixel's n+ diode resulting in a spread of particles (Matis *et al.* 2003).

Ionization damage is the dominant mechanism when energetic photons (γ and X-rays) interact with solid-state matter. The major concerns for CMOS sensors due to ionization damage are charge build-up in the gate dielectric, radiation-induced interface levels, and the displacement of lattice atoms in the bulk. The introduction of discrete energy levels at the Si–SiO$_2$ interface leads to increased generation rates and thus higher surface leakage currents. Similarly, displacement of lattice atoms in the bulk leads to modified minority carrier life-times and increased bulk-generated leakage currents. However, Padmakumar *et al.* (2008) did not find any significant threshold variations due to charge build-up nor radiation induced leakage currents when CMOS sensors were irradiated with γ-rays (1.17−1.33 MeV) with a dose rate of 75.9 Gy/min. Therefore, the increase in sensitivity observed in this work is not attributed to radiation damage. Nevertheless, as mentioned before the life-times of carries or generated electrons may play a role. Provided the epitaxial layer is made of very pure silicon, the carrier life-times are long enough to reach the depletion region. However, the epitaxial layer is not completely pure, which generates RG centres as discussed in section 2.5.4. Therefore, it is reasonable to think that there is signal loss at higher dose rates presumably due to recombination (Wilkins *et al.* , Padmakumar *et al.*

2008) which causes electron loss, thus reducing sensitivity. These results provide evidence for improving the design of CMOS sensors for dosimetry applications.

Chapter 6

Experimental validation of the phase-space files

6.1 Overview of chapter

The validation of the Monte Carlo beam model for small fields is presented in this chapter. The beam model is a set of publicly available phase-space files of a Varian Clinac iX. The MC-generated beams are validated against commissioning data of the Varian Clinac 2100CD used in this work; large field sizes are validated against commissioning data, film profile measurements are performed to validate the smallest MC-generated beam. Monte Carlo simulations in a water phantom provided information for additional validations. These results are compared to determine the suitability of the Monte Carlo small-field model to predict dosimetric properties of small photon fields.

6.2 Linear accelerator (linac)

A clinical linear accelerator model Varian 2100CD (Varian, Palo Alto, CA) was used for all experiments. This linac produces X-ray beams with energies of 6 and 10 MV. Figure 6.1 shows the linear accelerator used. In the head of the linac two pair of collimators (asymmetric jaws) at right angles provided square or rectangular fields. By adjusting these collimators field sizes from 0.5×0.5 to 25×25 cm^2 were produced.

The Varian 2100CD delivers pulsed radiation at a constant dose per pulse. The calibration of the machine was such that 100 MU/min corresponded to 1
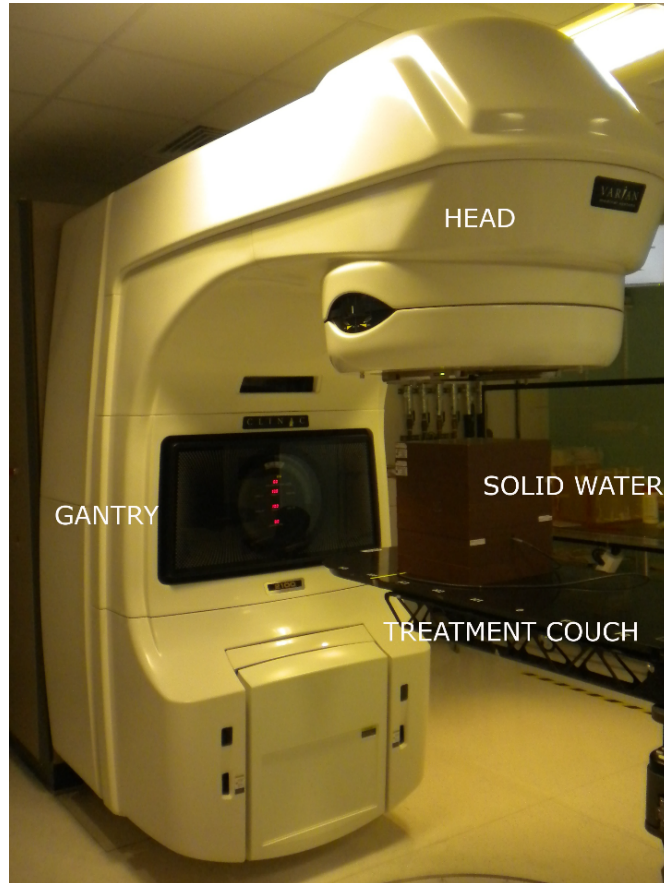
Figure 6.1: Linear accelerator Varian 2100CD at University College London Hospital.

cGy/MU at 5 cm (95 SSD) in water for a 10×10 cm^2 field. For the experiments presented in this work a regular sequence of pulses was required to make sure that the sensor was irradiated at equal number of pulses during integration. Using a continuous sequence of six pulses, a uniform frequency was obtained when the machine was operated between 100 and 600 MU/min. 100 MU/min was achieved by dropping 5 out of 6 pulses. At 600 MU/min the linac delivers 300 pps using a continuous sequence of 6 pulses per cycle.

6.3 Monte Carlo phase-space files

A phase-space file contains data with information related to position, direction, charge, and energy of all primary and secondary particles emerging from a linear accelerator. This description is collected for every particle crossing a scoring plane from the radiation source. This data is generated following a detailed Monte Carlo simulation of the linear accelerator head. The information required for such a

model must be obtained from manufacturers as blueprints.

A collection of 6 MV phase-space files for a Varian linear accelerator Clinac iX was downloaded from the IAEA NAPC Nuclear Data Section web site (http://www-nds.iaea.org/phsp/photon1/) and used as input for all simulations. These files were part of an IAEA project intended to establish a public database of phase-space data for clinical accelerators and ^{60}Co units used for radiotherapy applications (INDC 2005). The Monte Carlo simulation of these phase-space files are described in Hedin *et al.* (2010). The format of the files is standardized by the IAEA and follows the same philosophy used in BEAMnrc/EGSnrc simulations. A requirement of all files available on the IAEA web site is to use 10000 primary particles per unit area of interest to obtain an approximate 1% statistical uncertainty. At the isocentre plane a minimum of 2500 particles/mm^2 is guaranteed. These phase-space files were read using a Geant4 interface which is publicly distributed from the IAEA web site (Cortés-Giraldo 2009). The validation of the phase-space files was carried out against experimental measurements by the authors and it is detailed in Hedin *et al.* (2010).

The original Monte Carlo-generated PDD curves and beam profiles were provided by Emma Hedin (Sahlgrenska University Hospital, Gothenburg, Sweden) for comparison with the commissioning data of the linear accelerator used in this work. As mentioned above, the phase-space files were validated by their authors against commissioning data from the Varian Clinac iX at the Sahlgrenska University Hospital in Gothenburg, Sweden (Hedin *et al.* 2010).

6.4   The quality index: TPR$_{20/10}$

The first comparisons made for the phase-space file validation was the quality index of the machines (QI) or tissue phantom ratio at depths 20 cm and 10 cm TPR$_{20/10}$ measured for a 10 cm square field. Regular measurements of the quality index ensure that the energy of the radiation beam does not change significantly. By measuring the tissue-phantom ratio (TPR) it is possible to assess the photon beam quality. The quality index is dependent on beam energy, therefore it is a good dosimetric parameter to compare the beam energy of two different machines. This comparison was done from quality control data of four linear accelerators

available at UCLH and from the team that provided the phase-space files (in Gothenburg, Sweden).

6.5 Commissioning data

The commissioning data of the 6 MV energy beam Varian 2100CD linear accelerator consisted of PDD curves and beam profiles measured in a water tank. PDD curves were obtained for field sizes 4×4 and 10×10 cm^2, 100-cm SSD. This data was provided by the hospital staff as part of the commissioning performed on all linacs installed at the hospital. Beam profiles were obtained for field sizes 10×10 and 30×30 cm^2 measured between 1.5 to 25 cm deep, 90-cm SSD. These measurements were also performed by the hospital staff. Silicon detectors were used for all measurements.

Figure 6.2 shows 6 MV PDD curves from the linac commissioning data normalized to 5 cm deep. It is observed how the PDD curves are dependent on field size. As field size increases, the contribution of scattered radiation to the dose is greater, consequently the curve for 10×10 cm^2 field size shows greater doses with depth. Beam profiles for 10 and 30 cm square fields normalized to dose at central axis are shown in figures 6.3 and 6.4.
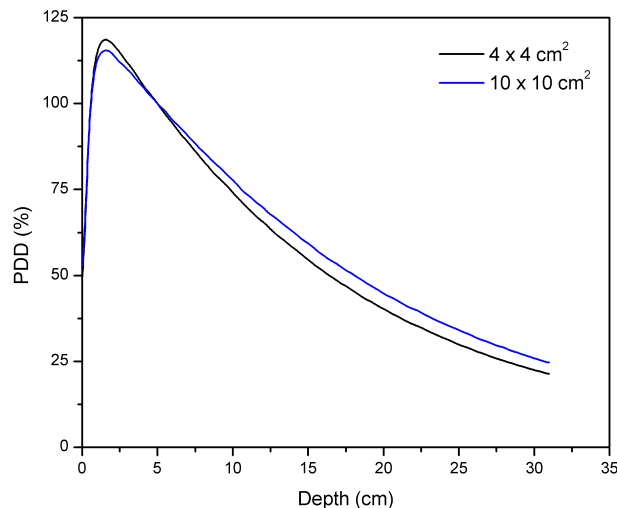
Figure 6.2: 6 MV commissioning PDD curves, 100-cm SSD, for 4×4 cm^2 and 10×10 cm^2 fields.
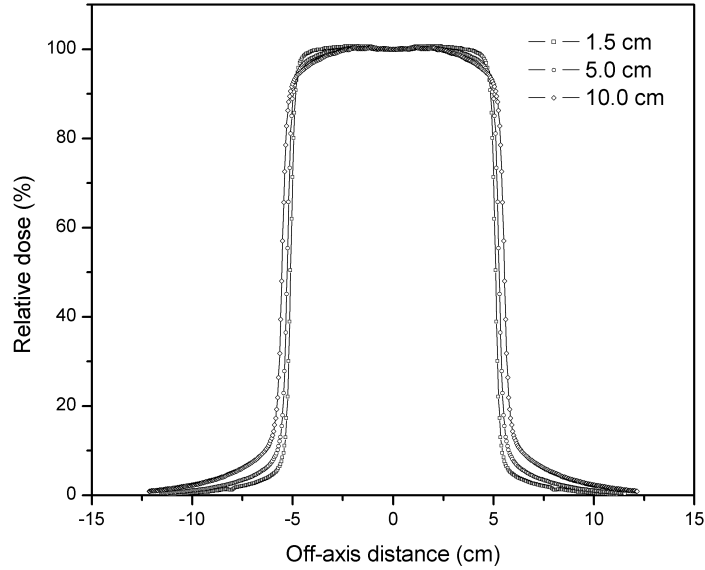
Figure 6.3: 6 MV commissioning beam profiles, 100-cm SSD at 1.5, 5.0 and 10.0 cm deep for a 10×10 cm^2 field.

6.6 Monte Carlo phase-space files validation

The Monte Carlo phase-space files were validated by comparing simulated PDD curves and cross-beam profiles against the commissioning data of the UCLH Varian 2100CD.

6.6.1 Results

Monte Carlo and commissioning PDD curves for 4×4 cm^2 and 10×10 cm^2 fields are compared in figures 6.5. It is seen that for both fields the commissioning PDD curves are slightly above the MC curves. This shows that the Varian Clinac iX MC modelled beam has a slightly lower effective energy than the UCLH Varian 2100CD. The MC PDD curves were interpolated from the depth-dose values of the commissioning curves using a cubic spline interpolation to calculate the percentage difference between MC-generated and measured PDD curves. An increasing relation of this percentage difference was observed with depth. The exact relation could not be determined, but up to about 4% and 5% difference was found for the 4×4 cm^2 and 10×10 cm^2 field PDD curves respectively.

Figure 6.6 shows the Monte Carlo and measured profiles for a 10×10 cm^2 field at depths 1.5 and 10.0 cm. The agreement is within the error bars except for
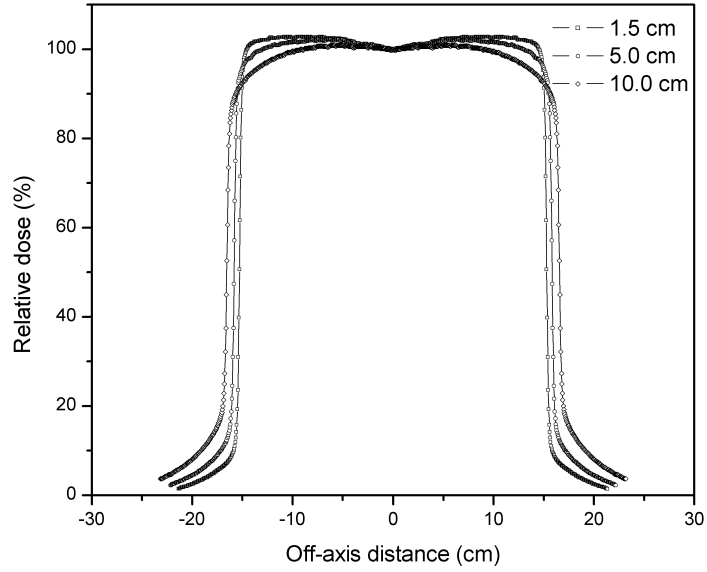
Figure 6.4: 6 MV commissioning beam profiles, 100-cm SSD at 1.5, 5.0 and 10.0 cm deep for a 30×30 cm^2 field.

the tails where the MC profiles are slightly above the measured values. The tails deviate more for larger fields. This is observed in figure 6.8 for a 30×30 cm^2 field. Figures 6.7 and 6.9 show the percentage difference between MC-generated and measured profiles for 10×10 cm^2 and 30×30 cm^2 fields respectively. As observed the differences in the horns and tails are smaller than 2%.
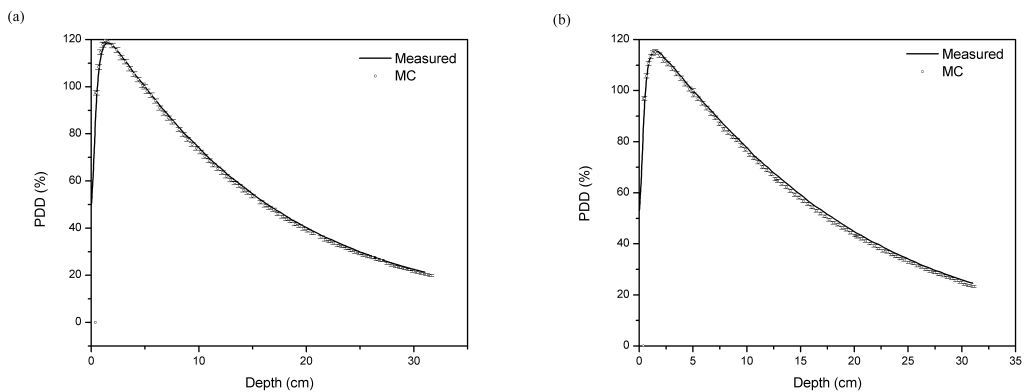
Figure 6.5: Comparison of Monte Carlo and commissioning PDD curves for 4×4 cm^2 (a) and 10×10 cm^2 (b) fields.
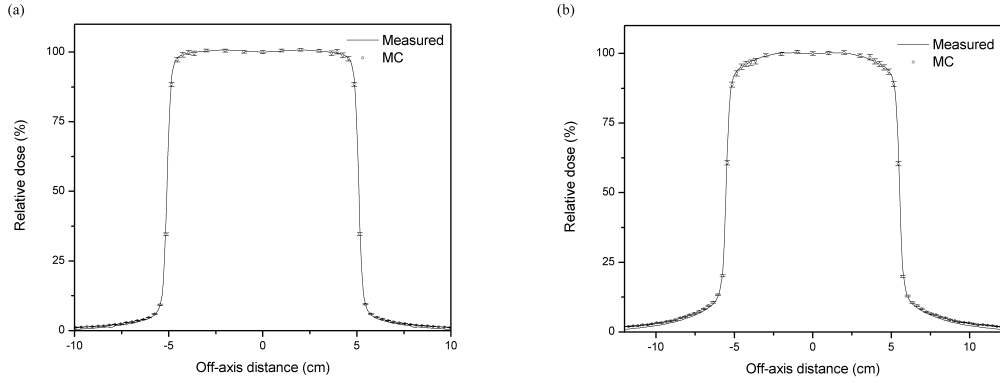
Figure 6.6: Comparison of MC-generated and commissioning 6 MV beam profiles for a 10 × 10 cm² field at 1.5 cm deep (a) and 10 cm deep (b).
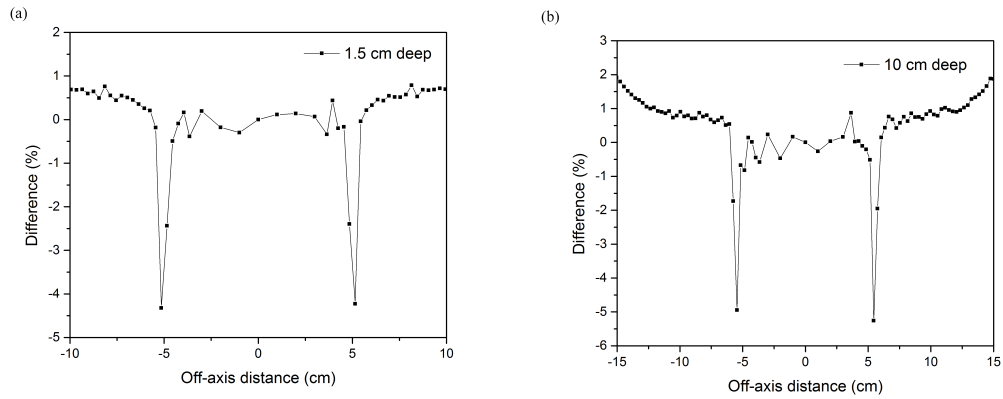
Figure 6.7: Percentage difference between MC-generated and commissioning 6 MV beam profiles for a 10 × 10 cm² field at 1.5 cm deep (a) and 10 cm deep (b).

The deviation in the horns is larger, which is possibly caused as the lower effective energies of the Monte Carlo modelled beams are more significant at off-axis distances due to the attenuation in the flattening filter or due to design differences between the modelled flattening filter in the MC simulation and the corresponding filter in the Varian 2100CD. Flattening filters change the beam energy distribution with off-axis distance due to their non-uniform shape and contribute to scatter dose. Consequently, the Monte Carlo-generated profiles are above the measured profiles in the horns for 30 cm square fields.

109
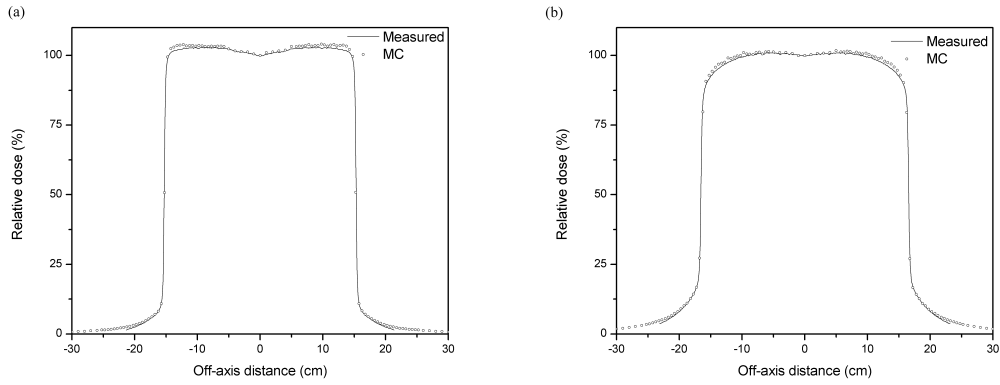
Figure 6.8: Comparison of Monte Carlo-generated and commissioning 6 MV beam profiles for a 30×30 cm^2 field at 1.5 cm deep (a) and 10 cm deep (b).
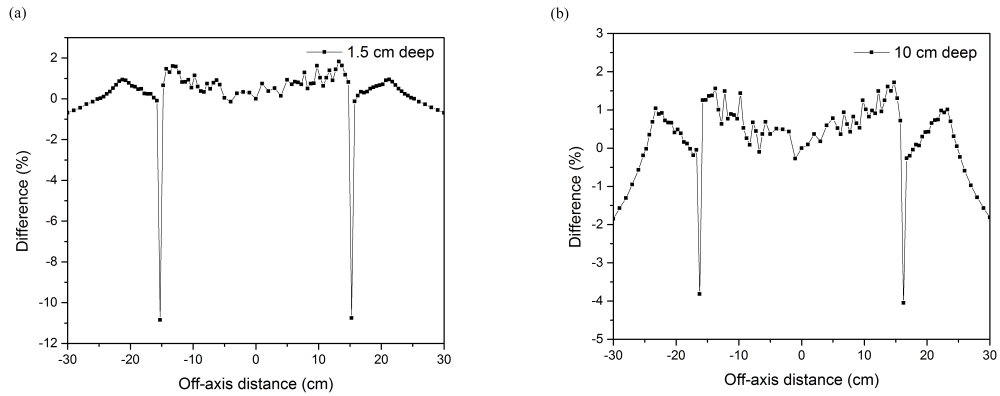
Figure 6.9: Percentage difference between MC-generated and commissioning 6 MV beam profiles for a 30×30 cm^2 field at 1.5 cm deep (a) and 10 cm deep (b).

6.7   Comparison of MC-generated and measured small-field profiles

The accuracy of the 0.5×0.5 cm^2 modelled beam from the MC phase-space files was investigated by performing a simulation of a beam profile in water and comparing it with experimental measurements of a 0.5×0.5 cm^2 beam of the Varian 2100CD with X-OMAT V film (Kodak Inc., Rochester, NY). Figure 6.10 depicts a section of the water scoring plane simulated. This plane consisted of 52 $\times$ 52 voxels of area 0.025×0.025 cm^2 and 0.1 cm thick. The dose was scored at 10 cm deep at the central axis of the water phantom, SSD 90 cm. The water phantom had dimensions $30 \times 30 \times 20$ cm^3. The beam direction was set along the negative vertical axis (y-axis).

110
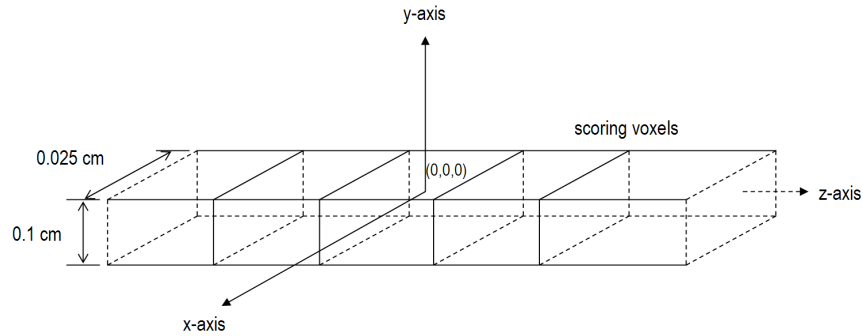
Figure 6.10: Section of the scoring plane used for profile simulation. The dose was scored in the voxels showed.

The particles emerging from the phase-space file were recycled 50 times to decrease the statistical uncertainty (i.e. each particle was used 50 times). The electron and photon cut-offs in water were 10 μm (100 eV) and 1 mm (2.93 keV) respectively. An output file with dose absorbed in each voxel along with their spatial coordinates was converted to a matrix using a developed Matlab (The MathWorks, Inc., Natick, MA) code. The profile was plotted by averaging 4 rows of voxels (1 mm). The resulting profile was then smoothed using a built-in Matlab function with a Savitzky-Golay smoothing filter with a third order polynomial.

The beam profile for the 0.5×0.5 cm^2 field was measured in a Solid Water phantom (Gammex, Inc., Middleton, WI) using Kodak X-OMAT V film. The Kodak X-OMAT is a low-speed film with emulsion coating on both sides of the plastic base (Pai *et al.* 2007). The film was oriented perpendicular to the X-ray beam at SSD 90 cm. Two slabs of 5 cm thick were used (10 cm) as backscatter material. Two additional slabs were placed on top of the film as buildup (10 cm). 50 MU were delivered to the film to ensure the film was used in the linear region of its response. A Vidar film digitizer (VXR-16, Vidar Systems Corp., Herndon, VA) was used to scan the film. The film scanner was operated with a resolution of 300 DPI and a depth of 12 bits.

6.7.1 Results

Figure 6.11 compares the simulated beam profile in water and that measured with film X-OMAT V for a 0.5×0.5 cm^2 field at 10 cm deep, SSD 90 cm. The agreement is good particularly in the tails in contrast to the comparison with
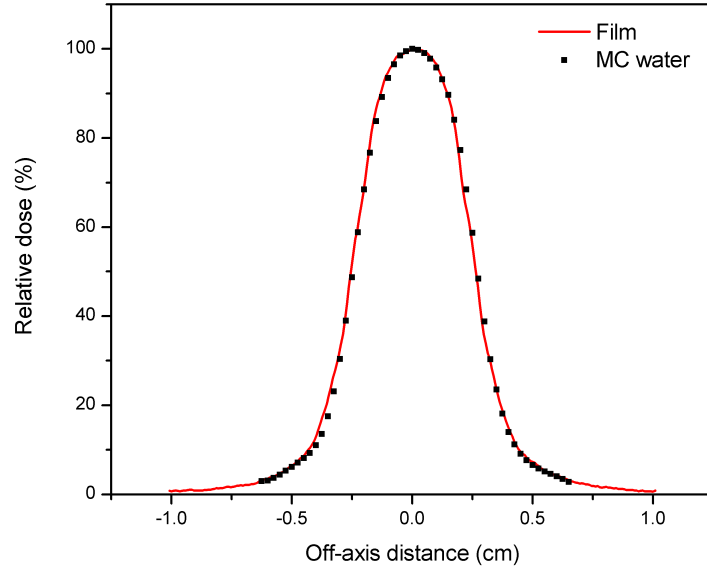
Figure 6.11: Comparison of Monte Carlo and measured beam profiles in water for a 0.5×0.5 cm^2 field. The profile was measured using Kodak X-OMAT V film in Solid Water.

larger fields in Section 6.6. Both profiles were interpolated to measure the field widths correctly. Field widths defined as the distance between the two points with 50% of the central axis dose measured at 10 cm deep for the Monte Carlo calculated small-field and measured profiles were in excellent agreement. For the Monte Carlo field width the result obtained was 0.51 ± 0.02 cm. The uncertainty represents the error associated with the voxel size used in the simulation. The corresponding field width measured with film was 0.51 ± 0.01 cm, with the uncertainty given by the resolution of the scanner. This comparison shows an excellent match between the Monte Carlo beam model for the smallest field and the experimental beam of the Varian 2100CD.

6.8   Discussion

The results presented in this chapter have shown that the Monte Carlo model of a Varian Clinac iX can be used for an accurate description of a small-field beam model for a Varian Varian 2100CD linear accelerator. This was done through PDD curves and cross-beam profiles comparisons.

The difference observed between the PDD curves in figure 6.5 is due to the

difference in electron energies between the MC phase-space model and the actual linac used in this work. The energy assumed by Hedin *et al.* (2010) for the electron beam hitting the target was 5.7 MeV, which is likely to be the cause of the observed discrepancy in the PDD curves with depth.

The Monte Carlo simulation of a beam model for small fields is complex and requires an accurate description of all linac components that contribute to the production of the radiation beam. The accuracy with which a Monte Carlo beam model can describe small-field dose distributions depends on the focal spot size assumed in the radiation source model. This focal spot width will affect the penumbra and beam profiles (Scott *et al.* 2008, Sham *et al.* 2008, Scott *et al.* 2009). Scott *et al.* (2008) showed that matching the penumbrae of accurately measured large-field beam profiles to those of a Monte Carlo model leads to accurate simulation for small fields. This methodology was employed for the profile comparisons shown in figures 6.6 and 6.8. The agreement was better for 10 cm square field profiles and in overall within 2%. For the larger profiles, deviations were significant even in the horns and tails. This is, presumably, due to differences between simulated and actual flattening filters and collimators respectively. It is known that the collimators and flattening filters in a linear accelerator affect the shape of the tails and horns of beam profiles (Khan 2003).

Even though the penumbral regions for the larger fields did not match accurately, the agreement was good when film-measured and MC-simulated small-field profiles were compared. The deviation in the horns and tails, however, seems not to affect small-field profiles as observed in figure 6.11.

The criterion used for small-field profiles comparison was the field size. The field width as well as tail region of the Monte Carlo beam matched well with experimental measurements using film. The results were in agreement within the experimental errors thus the Monte Carlo small-field model is accurate and comparable to the actual 0.5 cm square field of the Varian Clinac 2100CD.

According to results presented by Sham *et al.* (2008) the size of the radiation source (focal spot width) is the most important parameter that affects small-field profiles. The agreement presented here suggests that the focal spot width (FWHM of the gaussian distribution of the electron beam hitting the target) of

0.1 cm assumed by Hedin *et al.* (2010) is sufficient to produce realistic small-field profiles.

The quality index of the machines (QI) measured for a 10 cm square field at UCLH was 0.6644 ± 0.0015, while the ones simulated and measured by the team that provided the phase-space files (in Gothenburg, Sweden) where 0.6636 ± 0.0062 and 0.6682 (uncertainty in the fourth decimal place according to repetition of measurement) respectively. These values are in good agreement and within the statistical uncertainties, which is a first indication that both machines have equivalent beam quality. The simulated TPR (by the Gothenburg team) was sensitive to energy changes according to an approximate linear relation (between 5.2 and 6.4 MeV): TPR=0.02×E+0.53. This means that the difference observed between measured $TPR_{20/10}$ at UCLH and Gothenburg corresponds to a difference in energy of approximately 0.04 MeV, which is much smaller than the energy resolution available by the Gothenburg team when looking at depth dose curves for different energies and comparable to the resolution they had when comparing profiles for different energies. In this sense, the agreement between measured TPRs at UCLH and the ones simulated by the Gothenburg team is excellent (Hedin, email correspondence).

Chapter 7

The performance of CMOS APS for the dosimetry of small photon fields

7.1 Overview of chapter

In this chapter the performance of CMOS active pixel sensors to measure dosimetric parameters such as cross-beam profile, tissue-phantom ratio and output factor is presented. Results are compared to ionization chamber measurements and Monte Carlo simulations to asses the performance of the sensor. In addition, an investigation of Bragg-Gray cavity is also presented.

7.2 Beam profile measurements with CMOS sensors

The representation of dose variation across the field at a specified depth in a medium is known as the beam profile. Beam profile measurement in stereotactic radiosurgery (SRS) requires high spatial resolution (Das *et al.* 2007). Because of their small size diode detectors are used for beam profile measurements (McKerracher and Thwaites 1999). The effect of detector size on the accuracy of beam profiles was investigated by Dawson *et al.* (1986). It has been pointed out that with a detector size of 3.5 mm diameter, beam profiles of circular fields with diameters between 12.5 and 30.0 mm in diameter can be measured accurately to

within 1 mm (Rice *et al.* 1987). However, in SRS the target can be as small as 2 mm in diameter. This imposes the use of detectors with higher spatial resolution.

To study the performance of CMOS active pixel sensors for dose beam profile measurements, 6 and 10 MV small photon beams with fields of 0.5×0.5 cm^2 were imaged with the Vanilla sensor. Profiles were also measured with film X-OMAT V at 10 cm deep for comparison. A Vidar film digitizer (VXR-16, Vidar Systems Corp., Herndon, VA) was used to scan the film. The film scanner was operated with a resolution of 300 DPI and a depth of 12 bits.

The sensor was embedded in Perspex and sandwiched in Solid Water slabs at depths from 5 to 25 cm, but at a constant source-to-detector distance of 100 cm as in figure 7.1. Two slabs of Solid Water were placed as buildup material (10 cm). The linac was set at a dose rate of 100 MU/min to avoid sensor saturation.

The sensor was operated at 55 frames per second and an integration time of 18 ms. Image acquisition and control of the sensor were performed through a system based on a Memec Virtex-II ProTM 20FF1152 FPGA development board which generated the required control signal for the sensor. 100 frames were acquired per irradiation and transferred to a computer by a network cable at a rate of gigabits per second. This 100 frames were averaged to get a final image. These images were analyzed using Matlab and ImageJ to generate the beam profiles.
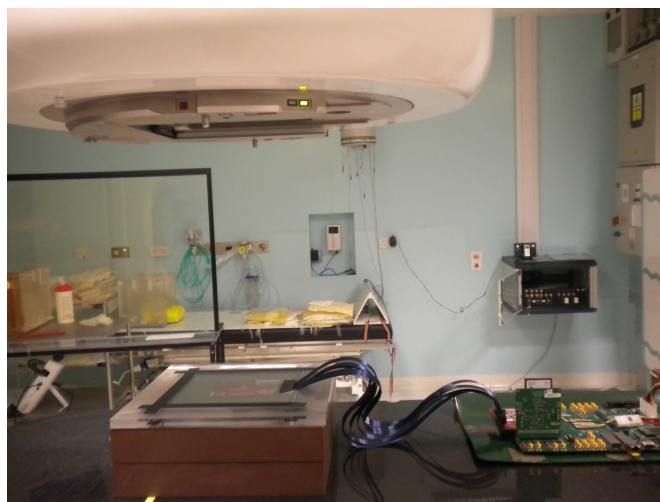
Figure 7.1: Setup used to measure dose profiles.

Beam profiles results

Figure 7.2 shows the cross-beam profiles measured with the CMOS sensor. These profiles were obtained by averaging 100 frames of the radiation beam and then plotting a row of pixels across the sensor array. The vertical axis represents the average gray levels or digital numbers (DN) in the pixels.
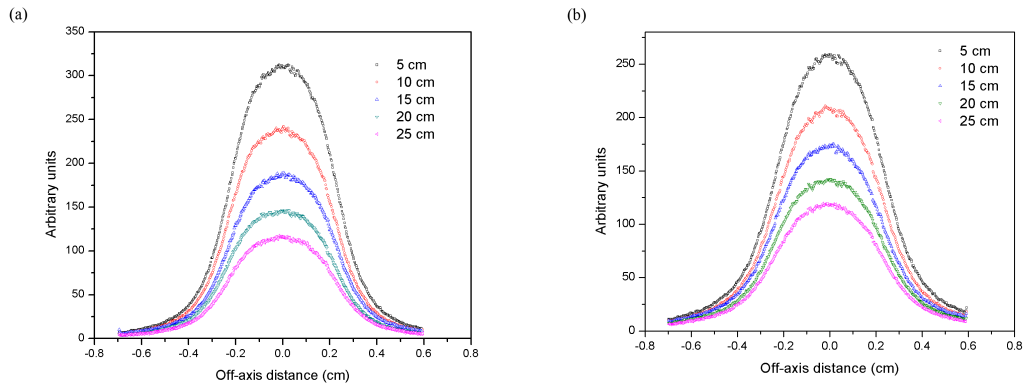
Figure 7.2: Profiles for a 0.5×0.5 cm^2 field at 6 MV (a) and 10 MV (b) measured with the CMOS sensor at different depths in Solid Water.
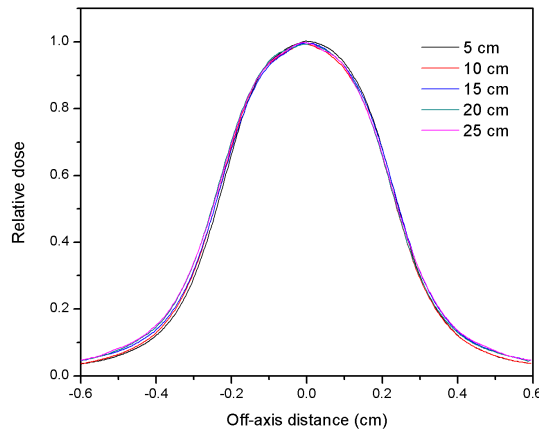
Figure 7.3: Profiles for a 0.5×0.5 cm^2 field at 6 MV, normalized to 1.0 at the central axis.

As expected, the sensor is capable of measuring profiles in Solid Water accurately. Variations with depth and energy are clearly seen by comparing both figures. Response non-uniformity and fixed pattern noise can be observed more clearly from the 10 MV profiles where the same features on the profiles were reproduced for all depths. This can, however, be corrected by applying a smoothing filter to the

profiles. Because the distance from the source to the detector was constant for all measurements, divergence of the beam was not expected. This is shown in figure 7.3 where the profiles for the 6 MV beam were smoothed for a better comparison. The small deviation among the profiles is due to the different scattering contribution with depth.

Figures 7.4 (a) and (b) compare images of the radiation field measured with film and the CMOS sensor for the 6 MV energy beam. The cross-beam profiles at 10 cm deep are shown in figures 7.5 (a) and (b). The agreement between these profiles was evaluated by comparing the 20%–80% penumbrae width and field width, defined as the distance between the two points with 50% of the central axis dose.
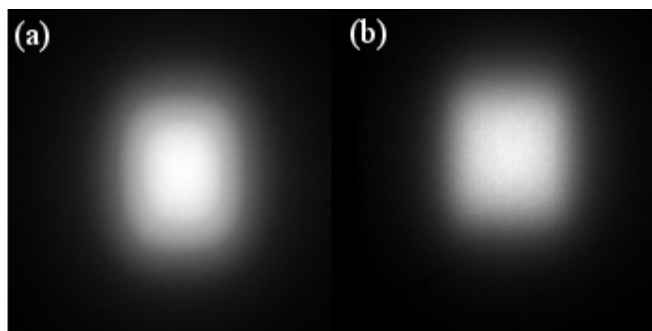
Figure 7.4: Radiation field imaged with film X-OMAT V (a) and the CMOS sensor (b) with the 0.5×0.5 cm^2 field for 6 MV beam.
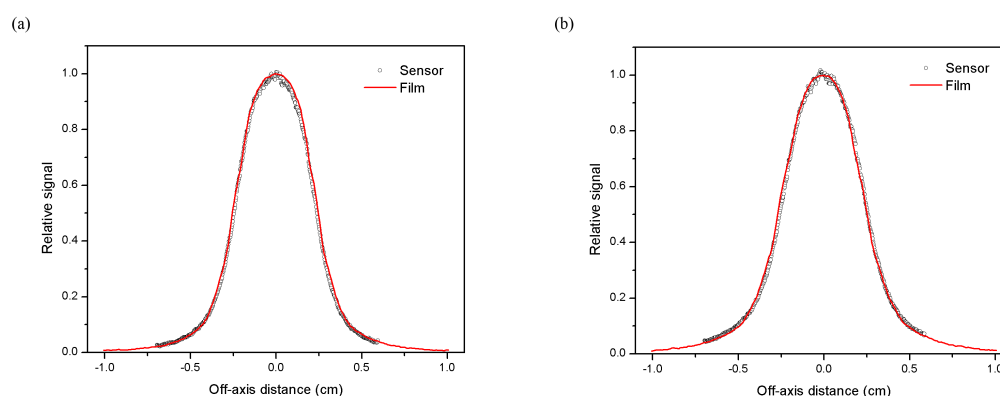
Figure 7.5: Comparison of measured profiles at 10 cm deep. Profiles for the 6 MV (a) and 10 MV beam (b).

Table 7.1 summarizes the results of 20%–80% penumbra width and field width measured with the sensor and film X-OMAT V. The percentage differences of the

Table 7.1: Comparison of field width and 20%–80% penumbrae measured with the CMOS sensor and film X-OMAT V for the 6 MV and 10 MV beams of the Varian Clinac 2100CD at 10 cm deep. The uncertainty of the film and sensor measurements is around 0.010 cm.

Energy (MV)	Field width (cm)		Penumbra width (cm)	
6.0	0.490	0.502	0.184	0.187
10.0	0.513	0.524	0.221	0.225

penumbrae measured with the sensor relative to film were 1.6 and 1.8% for 6 and 10 MV energy beams, respectively. The agreement for field width was within 2.4 and 2.1% for 6 and 10 MV energy beams respectively. There is an increase of field width and penumbra width at 10 MV as compared with 6 MV, which is due to the larger lateral range of the secondary electrons with energy.
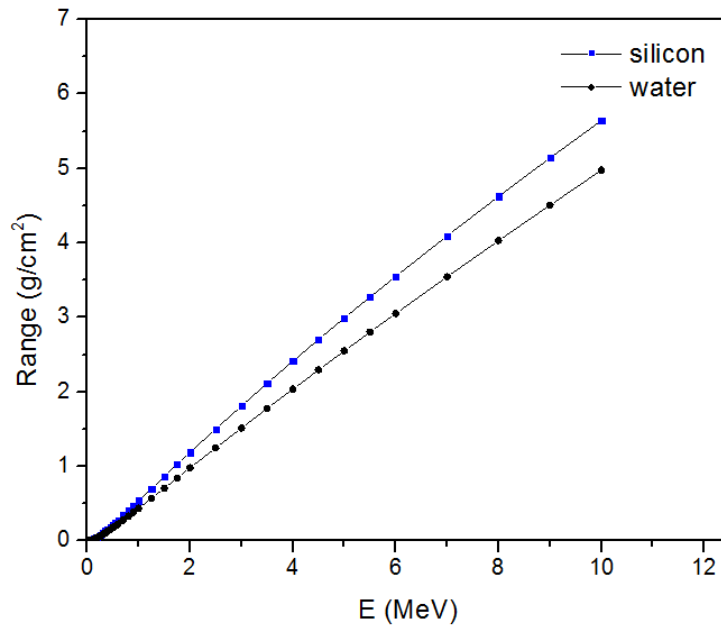
Figure 7.6: Comparison of CSDA electron ranges in silicon and water.

It is interesting to see that both field width and penumbra were shorter when measured with the CMOS sensor. Figure 7.6 shows the CSDA electron range for silicon and water as given by NIST data. As observed, the range in silicon is larger than in water, which at first sight does not account for the shorter field width and penumbra measured with the sensor. Additionally, film response is not significantly influenced by the off-axis variation of the energy spectrum due to scattered radiation (Pai *et al.* 2007), which is less likely to be the case for small

fields, so broadening of penumbra due to film can be discarded.

Because silicon is not water equivalent a change in electron transport is expected. The variation of transport properties between silicon and water as well as the change of the electron spectrum cause a reduction in the lateral range of the electrons compared to the range in water thereby sharpening the beam profile. As the photons, from the incident spectrum, pass through water set into motion electrons, mostly in the forward direction, that when reaching the silicon layer eject secondary electrons with ranges larger than those in the same equivalent layer of water (or film). Because of their larger ranges in silicon, these electrons will scatter less in the lateral direction thereby producing a sharper beam profile. As a consequence, field as well as penumbra widths are shorter. A similar effect (although explained from a different mechanism) reported to affect beam penumbra widths measured with diode detectors, is known as pseudo-sharpening of the beam profile (Beddar *et al.* 1994). This effect is, however, small and accounts for less than the percentage difference quoted above as the respective measurement uncertainties for the sensor and film are in the order of 5%. Nevertheless, the good agreement between film and the CMOS sensor suggests that the sensor can be used for accurate measurements in the penumbra region.

7.3   Tissue-phantom ratio measurements

The linear accelerator was set at a dose rate of 600 MU/min for ion chamber measurements. Before carrying out the measurements with the sensor a saturation level was determined by testing several combinations of integration times and dose rates. A dose rate of 100 MU/min with an integration time of 18 ms were found to give good results. To obtain this integration time the sensor was operated in digital mode. The sensor was embedded in a slab of Perspex of size $30 \times 30 \times 1$ cm^3. This slab was placed on 10 cm of solid water; additional solid water slabs were placed on top. The detectors were placed 100 cm from the radiation source at the isocentre. Measurements were carried out at a fixed 10 cm square field.

TPRs measured with the Vanilla sensor were defined as the signal in units of electrons, corrected for nonlinearity, in a region of interest (ROI) of 1 mm^2 at the centre of the sensor array normalized to the signal measured at 10 cm depth from

the ROI. The mean number of electrons was calculated by converting the average signal in the ROI to signal electrons through the ADC sensitivity $S(e-/DN)$ discussed in Chapter 3.
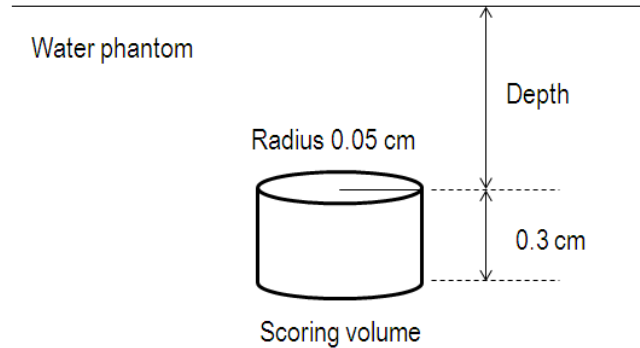
Figure 7.7: Monte Carlo setup for the simulation of TPR at 0.5×0.5 cm^2 field width.

TPRs were also measured using a Farmer ionization chamber for comparison with the Vanilla sensor. TPRs were defined as the dose at a specific depth on the central axis in the phantom normalized to the dose at a reference depth of 10 cm. Charge values were corrected for temperature and pressure before converting them to dose in Gray.

An additional set of TPRs was measured at 6 MV and a 0.5 cm square field. The procedure followed was the same as the one used to measure TPRs at 10 cm square field above.

Monte Carlo simulations in water were performed to calculate TPRs under similar conditions. The simulations were performed to validate experimental measurements with the sensor for 0.5 cm square field as the Farmer chamber is too big for small-field measurements. Figure 7.7 shows the setup of the MC simulation where the doses were scored in water at the same depths for comparison. These doses were calculated from the energy deposited in the scoring volume. The experimental setup was accurately modelled using GEANT4, where a cylinder of radius 0.05 cm and height 0.3 cm was used to score the dose at different depths. The incident spectrum was obtained from the phase-space files and the particles were recycled during the simulation to keep the statistical uncertainty below 2%.

TPR measurement results

A summary of the TPR results for 6 and 10 MV beams are shown in Tables 7.2, 7.3 and 7.4.

Table 7.2: Comparison of TPR measured with the sensor and the ion chamber for a 10×10 cm^2 field at 6 MV.

Depth (cm)	TPR (Sensor)	TPR (IC)	Diff. (%)
5.0	1.191 ± 0.005	1.188	-0.27
10.0	1.000 ± 0.005	1.000	0.00
15.0	0.815 ± 0.004	0.819	0.45
20.0	0.660 ± 0.002	0.665	0.75
25.0	0.540 ± 0.002	0.538	-0.37

Table 7.3: Comparison of TPR measured with the sensor and the ion chamber for a 10×10 cm^2 field at 10 MV.

Depth (cm)	TPR (Sensor)	TPR (IC)	Diff. (%)
5.0	1.142 ± 0.002	1.138	-0.33
10.0	1.000 ± 0.001	1.000	0.00
15.0	0.869 ± 0.006	0.862	0.91
20.0	0.739 ± 0.005	0.735	0.58
25.0	0.625 ± 0.001	0.626	-0.10

Table 7.4: Comparison of TPR measured with the sensor and MC-calculated in water for a 0.5×0.5 cm^2 field at 6 MV.

Depth (cm)	TPR (Sensor)	TPR (MC)	Diff. (%)
5.0	1.302 ± 0.003	1.299 ± 0.018	-0.23
10.0	1.000 ± 0.003	1.000 ± 0.009	0.00
15.0	0.780 ± 0.003	0.771 ± 0.005	-1.21
20.0	0.607 ± 0.002	0.616 ± 0.004	1.47
25.0	0.481 ± 0.001	0.477 ± 0.002	-0.85

The agreement between ion chamber and sensor measurements is very good for both energies and within 1.0%. These results are plotted in figure 7.8 for more clarity. TPR is dependent on depth, field width and radiation quality, so the good agreement between both detectors means that the change of the energy spectrum is small or negligible because silicon detectors are known to be energy dependent. However, a noticeable decrease of the TPRs for the 0.5 cm square field and 6 MV
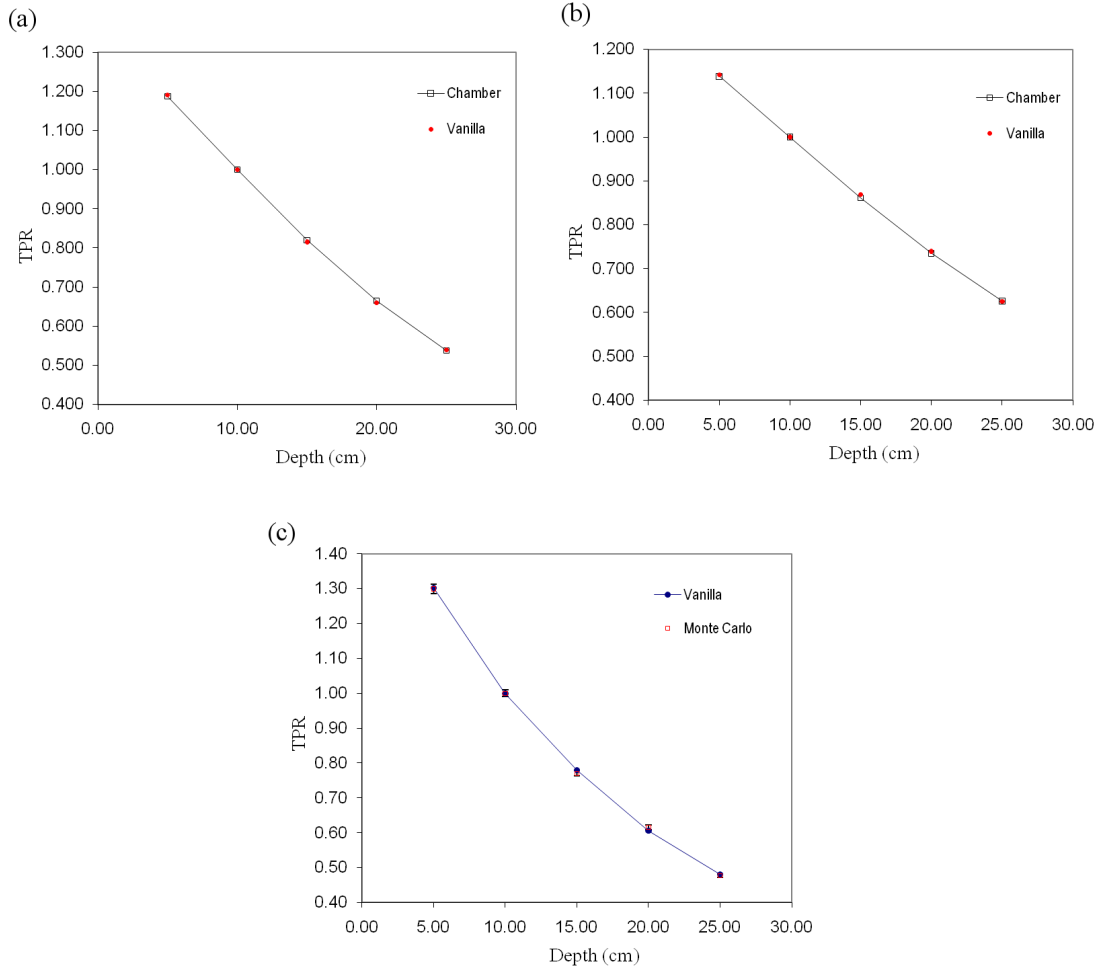
Figure 7.8: Comparison of TPRs measured with the Vanilla sensor and a Farmer ionization chamber for a 10 cm square field. TPRs measured at 6 MV (a) and 10 MV beam (b). Figure (c) shows a comparison of measured and simulated TPR in water for 0.5 cm square field, 6 MV. The error bars are smaller than the graph symbols.

in figure 7.8 shows its dependence on field width, while the sensor response varies accordingly. The agreement with MC calculations in water is better than 1.5%.

7.4 Output factor measurements

It is observed that the dose rate in air varies as a result of radiation scattered from the source and collimator. In general the dose rate in air varies with field width in a manner described by the output factor. The output factor is, therefore, incorporated into definitions of variables which describe the scattered radiation component to the total dose delivered (Ahuja *et al.* 1978).

In small fields the dose per monitor unit at d_{max} decreases as the field width is reduced because of the lack of lateral electronic equilibrium in phantom. This leads to a reduction in output with field width. As discussed by Duggan and Coffey (1998), when electronic disequilibrium exists at the centre of the field and the detector response depends on photon energy, the output will depend upon field width because the contribution of low energy scattered photons to the dose at the centre of the field decreases rapidly as the field width drops below a few centimetres.

To assess field width dependence, output factor were measured with the Vanilla sensor and compared with ionization chamber measurements. The output factors for 6 and 10 MV were measured relative to a reference depth of 10 cm in the phantom, SSD 90 cm and SAD 100 cm. The linac was adjusted to obtain square fields from 0.5 cm to 25 cm.

Output factors measured with the sensor were defined as the ratio of the sensor signal in units of electrons for a given field relative to a reference field of 10×10 cm^2. The signal was taken from the average over 100 frames in a ROI of 1 mm^2 and then corrected for sensor nonlinearity as mentioned earlier. The machine was operated at 100 MU/min for sensor measurements and 600 MU/min when measuring with the ionization chamber.

Monte Carlo simulations were performed to investigate the variation of the electron spectra set in motion at 10 cm deep in the water phantom for the 6 MV beam as a function of field width. The simulation setup was similar to that shown in figure 7.7 with SSD = 90 cm and SAD = 100 cm. The incident particles from the phase-space file were recycled 50 times. To make the simulation more efficient, cut-offs were set in the phantom and in the scoring volume separately for photons and electrons. The photon cut-offs in the phantom and the scoring volume were

2.92 keV which correspond to a range of 1 mm, while the electron cut-offs in the scoring volume and the phantom were 241.6 eV and 348.1 keV, which correspond to 1 μm and 1 mm respectively.

OF measurement results

OFs with the Farmer ionization chamber were measured down to 4 cm square field. OFs for smaller fields were not measured because is known that even small volume ionization chambers are not reliable for OF measurements in small fields (Metcalfe *et al.* 1992). OF comparisons are shown in figure 7.9. The agreement between OFs measured with the sensor and the Farmer chamber is better than 1.5% for 6 MV down to the 4×4 cm^2 field. For 10 MV beam the deviation is greater but smaller than 2%. It is difficult to observe a trend from these graphs to explain the discrepancies, but for both energy beams OFs deviate with field width.
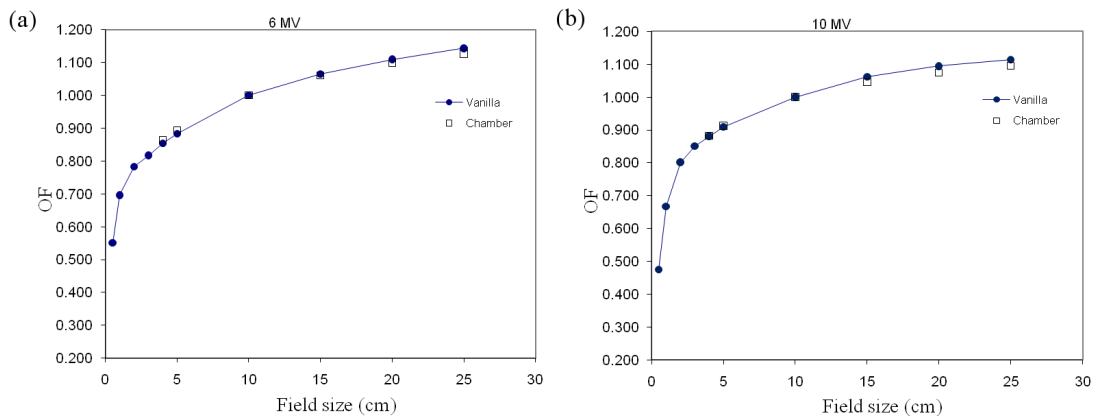
Figure 7.9: Comparison of OFs measured with the Vanilla sensor and a Farmer ion chamber at 6 MV (a) and 10 MV (b).

Results of the MC calculated electron spectra for the 6 MV beam and their variations with field width at the isocentre are shown in figure 7.10. The spectra are quite similar particularly at energies smaller than 4 MeV. The deviation observed for higher energies are produced by the reduced number of incident photons at high energies. Although the mean energy of smaller fields is expected to increase with depth (when compared with larger fields), as a result of a reduced scatter contribution producing harder spectra for smaller fields; this is no clearly appreciable from figure 7.10. This may be due to the fact that spectral variations

within small fields are less significant than variations with larger fields.
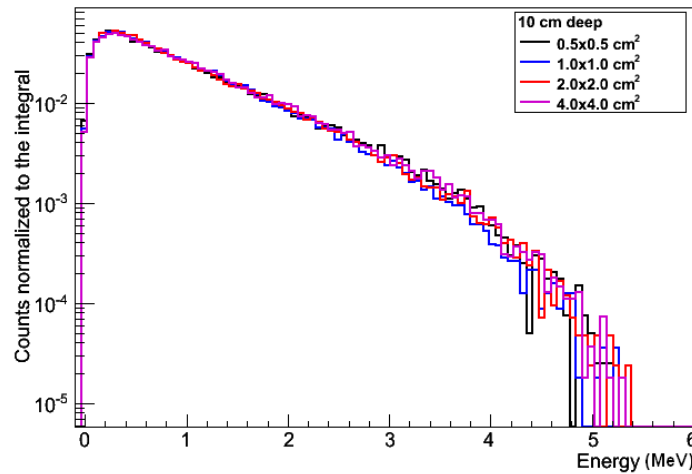
Figure 7.10: Electron spectra in water at 10 cm deep as a function of field width.

7.5 Investigation of the Vanilla sensor as a Bragg-Gray cavity

Small radiation fields measurements are more sensitive to the properties of the radiation detectors used (Scott *et al.* 2008). Fluence perturbations, loss of charged particle equilibrium and dose averaging effects are common problems encountered in small field dosimetry when using detectors with dimensions similar to the dimensions of the radiation field.

It is known that the introduction of a radiation dosimeter into a radiation field will disturb it. The disturbance is more significant when the composition of the detector is different to that of the medium. This will cause a change in the dosimeter response. Unless the perturbation is determined and the dosimeter response is corrected for, the dosimeter reading will not represent the dose in the medium.

Cavity theories are used to evaluate the perturbation factors introduced by the detector (Nahum 1996). The dose in the medium can be calculated as

$$D_{med} = f D_{det},\qquad(7.1)$$

where D_{med} is the dose in the medium, D_{det} is the dose measured in the sensitive

126

volume of the detector, and f is a factor which can be evaluated using cavity theories.

The application of cavity theories depends on the size of a detector's sensitive volume. For directly or indirectly absorbing radiation (e.g. electrons or photons) if the sensitive volume is small compared to the ranges of the charged particles the detector behaves as a Bragg-Gray cavity or electron detector and exact expression for f can be found. In this case the detector's energy response is dominated by stopping power ratios and the factor f is given by

$$f = [\bar{S}_{col}/\rho]_{med}/[\bar{S}_{col}/\rho]_{det} \qquad (7.2)$$

where the mass collision stopping power $\bar{S}_{col}/\rho$ is averaged over the electron fluence spectrum present in the uniform medium (Nahum 1996). The validity of equation 7.2 depends on the electron fluence present in the medium at the position of the detector, not being perturbed by the introduction of the detector.

In the case the medium and the detector have different atomic composition, density or both, a perturbation in the electron fluence is introduced. The correction of this perturbation can be done by the introduction of a perturbation factor p. In this case equation 7.2 is modified as

$$\bar{D}(z)_{med} = \bar{D}_{det} f p \qquad (7.3)$$

where $\bar{D}(z)_{med}$ is the dose in the medium at a position z, and $\bar{D}_{det}$ is the average dose over the sensitive volume of the detector.

The exact mathematical expression for p was given by Nahum (1996) and is

$$p = \frac{\int_\Delta (\Phi_E)^z_{med}(L_\Delta/\rho)_{det} dE + [\Phi(\Delta)^z_{med}(S(\Delta)/\rho)_{det}\Delta]}{\int_\Delta (\bar{\Phi}_E)^z_{det}(L_\Delta/\rho)_{det} dE + [\bar{\Phi}(\Delta)^z_{det}(S(\Delta)/\rho)_{det}\Delta]}. \qquad (7.4)$$

The meaning of each symbol in equation 7.4 is described in (Nahum 1996). It can be seen from equation 7.4 that if the electron fluence in the medium at z is equal to that averaged over the detector sensitive volume p becomes unity. On the other hand, if the difference is only in the magnitude and not in spectral shape then p

is

$$p = \frac{\Phi^z_{med}}{\bar{\Phi}_{det}}. \tag{7.5}$$

The factor p in equation 7.5 is the ratio of the detector dose that would result from ideal Bragg-Gray behaviour to the actual detector dose. The deviation of p from unity will indicate departure from Bragg-Gray cavity conditions. Silicon has a density of 2.33 g/cm^3 and an atomic number equal to 14 which introduces a significant perturbation in water (water has a density of 1 g/cm^3 and an effective atomic number of 7.42). However, if the sensitive volume of the detector is small enough such that the electron fluence over the volume remains undisturbed Bragg-Gray conditions may be met.
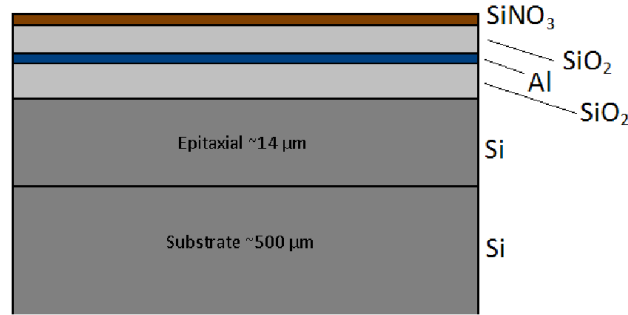
Figure 7.11: Cross section of the Vanilla sensor.

Figure 7.11 shows a cross section of the Vanilla sensor. The size and composition of all layers of the sensor are shown in Table 4.9. The perturbation introduced by these six layers are completely included in the factor p. This factor along with f can be estimated experimentally by a direct measurement of the dose over the detector's sensitive volume and the dose in the medium with an ionization chamber. For a theoretical verification of the detector behaving as a Bragg-Gray cavity Monte Carlo simulations can be performed to compare the electron fluence spectra in water and in silicon. This will be investigated in the next section.

7.5.1 Monte Carlo simulation of electron spectra in silicon and water

Monte Carlo simulations were performed to compare the electron spectra in the sensitive volume of the Vanilla sensor and in water at 10 cm deep. The radiation beam was a 6 MV photon spectrum from the phase-space files available at the IAEA NAPC Nuclear Data Section web site (http://www-nds.iaea.org/phsp/photon1/). A 4×4 cm^2 field width was selected.

The simulation setup was similar to that shown in figure 5.1, but using 10 cm of water as buildup material. Figure 7.12 compares the electron spectra in the sensitive layer of the sensor and that scored in the same volume, but with all layers replaced by water. The spectra are quite similar at larger energies except at energies lower than 0.6 MeV in which the electron spectrum in silicon is slightly higher than in water. A peak is seen in both spectra at the same energy, however, the peak in the water layer is higher.
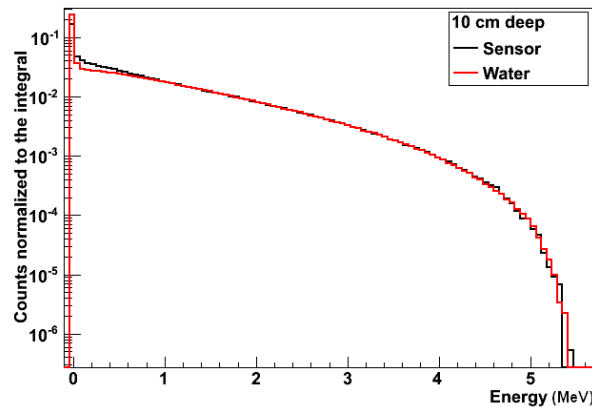
Figure 7.12: Comparison of electron spectra in water and in the sensor at 10 cm deep in a water phantom. The logarithmic scale in the vertical axis is for clarity.

To investigate further the resemblance of these spectra and to discard artefacts caused by limitations in the GEANT4 electron transport implementation (e.g. electron step size artefacts at interfaces) additional simulations were performed. The simulations consisted of scoring the electron spectra in a single layer of 14 μm of silicon and another layer of water, both in a water phantom at 10 cm depth. Two additional simulations were made inserting the Vanilla sensor in water at 10 cm depth, but with all layers made of silicon for one simulation while

made of water for the other one. Figure 7.13 compares the spectra. The results suggest that the electron spectrum is modified by artefacts caused, presumably, by an interface effect. This can be suggested because the spectra scored in a single layer (i.e. in red and purple) do not present the characteristic peak at lower energies. Moreover, the normalized counts are slightly above the corresponding to the spectra in the actual sensor simulation. As far as the Monte Carlo code is concerned there must not be any difference between a layer of water inserted in a water phantom and several layers of water surrounded by the same medium. In other words, these results suggest that the simulation of layered detectors (more than two contiguous layers) is not feasible demonstrating that problems with electron transport at interfaces may still be present in GEANT4 as reported in an earlier publication by Poon and Verhaegen (2005) and Poon *et al.* (2005).

The two spectra compared in figure 7.13 (right) show that the 14 μm layer of silicon has a similar response to that of an equivalent thickness of water. However, the 6 μm of material on top of the epitaxial layer and the 500 μm thick substrate may change the response of the sensor.
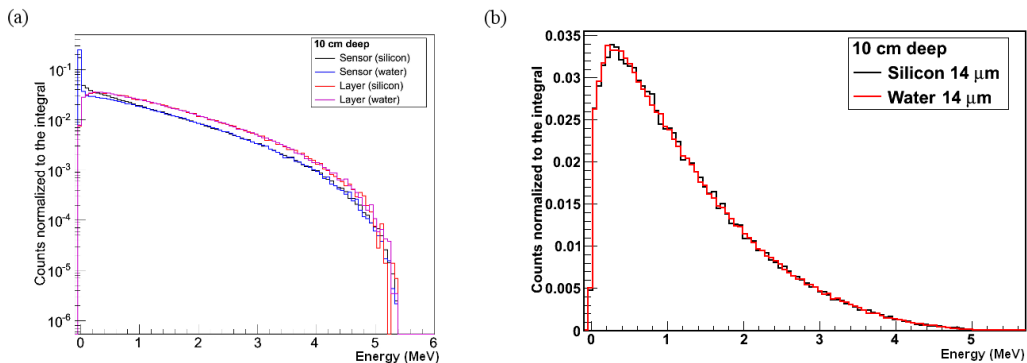
Figure 7.13: (a): Comparison of electron spectra in the actual sensor and the same sensor with its materials replaced by water. These two spectra are compared with the spectra scored in a layer of silicon and water at 10 cm deep in water. (b): Spectra scored in the 14 μm layers of silicon and water plotted in linear scale.

7.5.2 Experimental investigation of Bragg-Gray behaviour

To investigate whether the CMOS sensor behaves as a Brag-Gray cavity, dose measurements were carried out in a Solid Water phantom. The sensor and the ionization chamber were placed in phantom at the isocentre from 5 to 25 cm depth and a SAD = 100 cm. The 6 MV beam was adjusted at 10 cm square field because

the calibration of the ionization chamber is not valid for small fields. Dose rates of 100 and 600 MU/min were set for the sensor and chamber respectively. Results are shown in Table 7.5. Dose to silicon was calculated from

$$D = \frac{1.6 \times 10^{-19} J/eV \times S\, w}{m} \tag{7.6}$$

where S is the mean signal per pixel in unit of electrons corrected for nonlinearity, w is the mean energy required to generate an electron-hole pair in silicon and equal to 3.6 eV, and m is the mass of one pixel, which is about 2.04×10^{-11} kg. The signal per pixel was averaged over 1600 pixels in a 1×1 mm^2 on the array.

Table 7.5: Dose values measured with a Farmer chamber and the silicon sensor at 5 cm deep in a Solid Water phantom at the isocentre. The ionization chamber reading is given in Coulomb (C) and the sensor signal in electrons (e^-). The time is seconds is the integration time for measurements. The error quoted is the standard error on the mean of three consecutive measurements.

Detector	Reading	Dose (Gy)	Error (%)	Dose rate (MU/min)	Time (s)
Ion chamber	2.187×10^{-8}	0.987	0.1	600	10.20
Silicon sensor	9216	0.00026	0.2	100	0.018

To compare results shown in Table 7.5 the dose to water measured with the ionization chamber had to be recalculated for the integration time set to the silicon sensor (0.018 s). This is

$$D_{\text{water}} = \frac{(0.987 \text{ Gy})(0.018 \text{ s})}{10.2 \text{ s}} \times (100/600)$$
$$= 2.90 \times 10^{-4} Gy$$

where it is assumed that the ion chamber and sensor response are dose-rate independent. From these results the factor to convert dose to silicon into dose to water can be calculated as

$$D_{water/silicon} = \frac{2.90 \times 10^{-4}}{2.60 \times 10^{-4}}$$
$$= 1.11.$$

This factor gives a dose to water 11% higher than the corresponding dose to silicon, which is expected as the stopping power in silicon is smaller than that in water. This is observed in figure 7.14, where the stopping power ratio (water to silicon) is compared with the stopping power ratio corresponding to water to air.
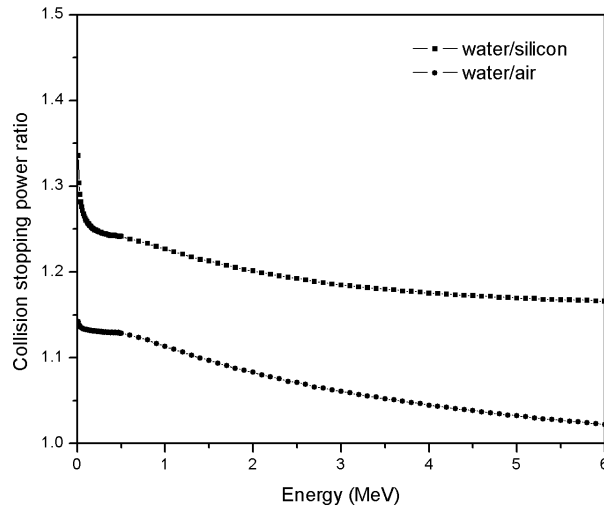
Figure 7.14: Stopping power ratios for water to silicon and water to air.

Table 7.6: Dose to water and dose to silicon ratios as a function of depth in the phantom for 6 MV and 10 MV energy beams.

Depth (cm)	6 MV	10 MV
5	1.115 ± 0.011	1.126 ± 0.011
10	1.118 ± 0.011	1.130 ± 0.011
15	1.123 ± 0.011	1.119 ± 0.011
20	1.126 ± 0.011	1.123 ± 0.011
25	1.114 ± 0.011	1.131 ± 0.011

Table 7.6 shows dose to water and dose to silicon ratios as a function of depth in phantom for 6 MV and 10 MV energy beams. From equation 7.3 the perturbation factor can be defined as

$$p = \frac{\bar{D}(z)_{med}/\bar{D}_{det}}{f}, \qquad (7.7)$$

where f is the stopping power ratio $s_{med,det}$. The stopping power ratio in equation 7.7 has to be evaluated over the electron spectra in water and silicon. If the

electron spectra are identical in shape and magnitude $f = 1$ and p is equal to the ratios in Table 7.6; however in Section 7.5.1 was concluded that although the electron spectra in a 14-μm silicon layer is identical in shape to that in water, interface artefacts affect the electron spectrum scored in the modelled detector and as a consequence the perturbation factors would not be correct. To recalculate the perturbation factors it would be necessary to use a different Monte Carlo code (e.g. EGSnrc).

7.6 Discussion

The purpose of this study was the investigation of the performance of CMOS active pixel sensors and the determination of an accurate dosimetry technique for radiotherapy applications where small fields are used (e.g. radiosurgery). An important aim of this investigation was to determine the feasibility of CMOS sensor technology as an alternative in small-field dosimetry.

It is known that uncertainties in small-field measurements can lead to inaccuracy in the calculation of patient doses (García-Vicente *et al.* 2005). Therefore, it is widely recognized the need for accurate radiation dosimetry and measurement techniques to guarantee the correct dose delivery (Das *et al.* 2008). Confident knowledge of small-field radiotherapy treatments is limited by the dosimetric accuracy achieved, which is strongly dependent on accurate radiation detectors. Therefore, the characterization of detectors for small-field dosimetry is very important.

7.6.1 Beam profile measurements

Beam profiles are required as input to the treatment planning systems before dose delivery can be performed. It has been pointed out that beam profile measurement accuracy is crucial for the tight conformation of the planned dose to the planning target volume (PTV) and the overall success of a treatment (Pappas *et al.* 2008). In particular, penumbra broadening due to the finite size of detectors is the most important parameter (Dawson *et al.* 1984, Beddar *et al.* 1994). One of the reasons is because radiosurgery is a technique that delivers high doses in one single fraction, which puts stringent requirements in the accuracy of dose delivery.

Volume averaging and, consequently, broadening of penumbra is caused by the limited spatial resolution of detectors employed to measure beam profiles. The direct effect on treatment outcomes is the over-irradiation of organs at risk.

Beam profiles measured with the Vanilla sensor shown in figure 7.2 and compared with film in figure 7.5 are in good agreement. The penumbrae widths agree to within 1.6 to 1.8% for both energies while the agreement for field width is better than 2.5%. The disagreement represents about a tenth of a millimitre for field width and much less for penumbra at 6 MV. This shows no volume averaging when measuring with the CMOS sensor. The small size and thickness of the pixel provide a resolution comparable to film. Moreover, the capability offered by imaging sensors to perform two-dimensional measurements is an advantage over other detectors because it is possible to image, in two dimensions, the radiation field by a single measurement. Because pixels can be considered as individual detector elements beam profile can be measured accurately as demonstrated.

7.6.2 Tissue phantom ratio measurements

Tissue phantom ratio is another dosimetric parameter which is required to be measured for commissioning, quality assurance or as an input of treatment planning systems for the calculation of absorbed dose in a patient. However, TPR data hardly exist in the literature of small fields (Sauer and Wilbert 2009). It has some advantages over PDD because it does not depend on source-to-surface distance (SSD), which makes it suitable for isocentric techniques.

The TPRs measured with the Vanilla sensor in Tables 7.2 and 7.3 are in good agreement with those measured with the ionization chamber and within 1.0%. The comparison between measured and simulated TPRs for the small field agree to within 1.5%. The variation with scatter contribution seems to be insignificant at 6 MV. Heydarian *et al.* (1996) measured tissue maximum ratios (TMR: TPR normalized at the depth of dose maximum) for a silicon diode, a diamond detector and film. Their results compared to Monte Carlo calculations showed a significant dose rate dependence of diamond and diode even though diamond detectors are energy independent.

Because silicon has a relative high atomic number compared to water (Z =

14) an over-response is expected to lower-energy and to a lesser extent to the higher-energy component of the photon spectrum due to the photoelectric and pair production effects, respectively. When the energy absorption coefficient ratios for silicon and water are compared, a factor slightly above 7 (at 30 keV) is found. However, it seems that this has no significant effect on the detector response to spectral changes with depth. This is because the small low-energy photon component in the spectrum is attenuated and partially removed and the dominance of the Compton effect (Heydarian *et al.* 1996). Therefore, the differences observed between TPRs measured with the Vanilla sensor and ionization chamber arise from the nonequivalence of the sensor to water and the variations of the collision stopping power ratio (water to silicon) as shown in figure 7.14.

7.6.3 Output factor measurement

The agreement between the CMOS sensor and the Farmer chamber for output factor measurements was within 1.5% for 6 MV and 2% for 10 MV. As shown in figure 7.9 this comparison was only done down to a 4 cm square field. Monte Carlo simulations could not be performed due to complications to properly read the phase-space files. Nevertheless, an uncertainty of 1.5% (1 SD) is according to IAEA (2000) the overall uncertainty of clinical absorbed dose measurements. A 1.5% error means that at a dose delivery of 100 MU/min we have a discrepancy of 1.5 MU per 100 MU, or 1.5 cGy, which is clinically acceptable. This however, shows that smaller discrepancies may be achieved if the sensor is optimize by reducing noise sources and design. Moreover, at smaller fields the sensor would behave better because narrower beams show hardening of the primary beam, as the result of the reduced low-energy scatter contribution, this may decrease any energy dependence of the response of the sensor.

7.6.4 Bragg-Gray investigation

Bragg-Gray condition is important because the conversion from dose measured by a detector introduced into a medium to that in the medium is reduced to a simple conversion factor. If the sensitive volume of the detector is small compared to the range of secondary electrons in the medium, Bragg-Gray condition may be met. The findings of this thesis show that dose to silicon deviates about 11–12%

from that measured with ionization chambers. However, the perturbation factors could not be calculated with the MC code because interface artefacts were found to affect the electron spectrum in the modelled detector giving rise to an incorrect evaluation of the stopping power ratio over the electron spectrum. Nevertheless, it has been verified that GEANT4 does not simulate electron transport correctly between interfaces. In addition, the result shown on the right side of figure 7.13 suggests that the spectrum in a silicon layer of 14 μm thick has the same shape as the spectrum calculated in water, which is encouraging and gives evidence that CMOS sensors could behave as a detector that departs slightly from a Bragg-Gray cavity. Further investigations have to be made to study the perturbation introduced by the layers on top of the sensitive volume. This would provide a better insight into the behaviour of the detector in a Solid Water phantom.

Chapter 8

Conclusions

This work has presented an experimental and Monte Carlo investigation of the performance of CMOS active pixel sensors for the dosimetry of small-photon beams. As reviewed in this work the dosimetry of small-photon beams presents complexities due to the characteristics of the radiation beam and the limitation of current detectors to accurately measure dose under disequilibrium conditions. It is known that when the radiation field is small compared to the range of the electrons set into motion in the medium standard dosimetric protocols to calculate dose are unreliable, thereby introducing uncertainties. These uncertainties have a direct impact on the clinical outcome of treatments performed with small beams. This is only overcome by using tissue-equivalent detectors with high spatial resolution to not disturb the radiation field. Accurate determination of dosimetric data as cross-beam profiles, TPRs and OFs are of great importance for the correct dose delivery in treatment techniques as SRS.

8.1 Cross-beam profiles

Beam profiles are very important in stereotactic radiosurgery because the high doses delivered in one single fraction put strict limits on the geometric accuracy of the dose delivery. Detectors with high resolution are of primary importance, and in this regard CMOS active pixel sensors have been shown as promising detectors for dose measurement. In particular, this work has demonstrated that CMOS APS can accurately measure profiles of fields as small as $0.5{\times}0.5$ cm^2. The agreement with film measurements of penumbrae for 6 and 10 MV beams was within 1.6 and 1.8% respectively. Field width results agreed to within 2.1

and 2.4%. However, the discrepancy in field size and penumbra width was as small as a tenth of a millimetre. These deviations are of no clinical significance. In this respect, the Vanilla sensor provides an excellent performance for beam profile measurements. In contrast, ionization chambers fail to measure beam profiles accurately (González-Castaño *et al.* 2007), while diode detectors produce a sharper penumbra (Beddar *et al.* 1994), which is nearly negligible for CMOS sensors.

It has been shown that Monte Carlo radiation techniques can be used as reliable references for dosimetry of very small photon beams, especially as an alternative to ionization chambers whose response is severely affected by lack of lateral electronic equilibrium and volume averaging. The findings of this study have demonstrated that matching the penumbrae of accurately measured large-field beam profiles to those of a Monte Carlo model leads to accurate simulation for small fields. It was also found that deviations in the horns and tails of large compared fields did not affect small-field profiles. The results presented in this work suggests that a focal spot width of 0.1 cm is good enough to produce realistic small-field profiles.

8.2 TPR measurements

Tissue phantom ratios were also in good agreement with both Monte Carlo calculations and ionization chamber measurements. Deviations smaller than 1.0% with respect to the ionization chamber measurements and about 1.5% with the Monte Carlo result are quite satisfactory. In particular the GEANT4 Monte Carlo code is accurate within 1.5% therefore the observed discrepancy are quite acceptable. Taking into account the uncertainties introduced by the sensor nonlinearities, signal loss due to recombination and the sources of noise that affect CMOS sensors signals an agreement within 1.0% is indeed acceptable. The signals measured with the CMOS sensor used in this work are accurate within 0.2%, however systematic errors can be introduced when correcting for nonlinearity because the method itself is very sensitive to an accurate estimation of the photon flux incident on the pixel array and the lowest detected signal for calibration through photon transfer (Jiménez 2009).

8.3 Output factors

Output factors results, although presented showing higher discrepancies with experimental measurements, were within clinical acceptance. However, the performance of output factor measurements with the Vanilla sensor compared to other detectors or Monte Carlo simulations currently restricts routine clinical implementation of CMOS sensors. More investigation has to be carried out.

8.4 Dose rate dependence

It was found that the Vanilla sensor presents dose rate dependence. This was measured through the calculation of the sensor sensitivity. A sensitivity increase as high as 5% was measured. A literature investigation to account for possible causes revealed that the increase in sensitivity is likely to be caused by signal loss due to recombination in the sensor. This, however, should not affect isocentric measurements such as TPRs, beam profiles and output factors.

8.5 Summary of contributions

The results of this work have shown for the first time the clinical potential of CMOS active pixel sensors for small-field measurements. CMOS sensors offer high spatial resolution, speed and sensitivity to measure dose under conditions where ionization chambers fail. In this work the performance of CMOS sensors was investigated to measure beam profiles of very small fields. It was found that CMOS sensors can accurately measure beam parameters. The agreement with film measurement and Monte Carlo simulations was acceptable.

Experimental measurements showed that the Vanilla sensor provides a spatial response that is suitable for small field measurements. In particular, a very thin detector like the Vanilla sensor overcomes volume averaging effects, as well as broadening and sharpening of beam penumbrae. It was found that at the energies and the small field investigated in this work the off-axis variations of the sensor response with spectral changes across the field are small and do not limit penumbrae measurements, although field size dependence was found for larger fields. The dependence of the Vanilla response with depth was also assessed by TPR measurements. Experimental and Monte Carlo results showed that the response

of the sensor agree to within 1.0% when compared with ionizations chambers.

These results are encouraging and show that CMOS active pixel sensors have the potential to attract the interest for dosimetric applications in radiation therapy.

The main conclusions of this work can be summarize as follows:

(i) The first application of CMOS active pixel sensors has been demonstrated for radiation therapy dosimetry and in particular for small-fields.

(ii) The clinical performance of CMOS sensors for small-field measurements was assessed in this work. The findings of this study are encouraging.

(iii) It has been demonstrated that CMOS active pixel sensors can measure accurately tissue phantom ratios, and field and penumbra widths under lateral electronic disequilibrium. These results are clinically acceptable.

(iv) It has been demonstrated that CMOS active pixel sensors can be used to measured absorbed dose after a proper calibration through photon transfer technique.

(v) Findings of this study have demonstrated that CMOS active pixel sensors have a great potential for accurate beam data measurement.

8.6 Future research

Because the aims of this work were to investigate the potential of CMOS active pixel sensors to overcome the limitations of current detectors in small-field dosimetry and to provide evidence for future developments, future work is necessary to get a better understanding of all features and limitations of CMOS sensor for dosimetric applications. Some future work is presented below:

(i) The dose rate dependence observed in section 5.5 deserves a more detailed study. A literature review suggested that the possible reason for the sensitivity increase observed was caused, presumably, due to signal loss arising from a recombination process, however a complete theoretical and experimental study should be carried out to characterize and quantify the suggested explanation.

(ii) Output factors measurements down to 0.5 cm square field were performed, but comparisons with a detector calibrated for field sizes smaller than 4 cm square fields are required.

(iii) Additional work has to be done to investigate whether the Vanilla sensor behaves as a Bragg-Gray cavity and in that case to calculate the perturbation factors. As it was found, GEANT4 did not properly simulate the electron spectra for layered detector due to artefacts associated to interface which distort the electron spectrum in the sensor sensitive layer. Monte Carlo simulations with EGSnrc would provide a better insight of the correct electron spectrum in the Vanilla sensor.

Glossary

Beam profile A representation of the dose variation across the field at a specified depth.

CMOS Complementary metalŰoxideŰsemiconductor.

CPE Charged particle equilibrium. *Charged particle equilibrium exists with respect to volume V if each charged particle of a given type and energy leaving V is replaced by an identical particle of the same energy entering, in terms of expectation values.* Here the volume V represents, for instance, the cavity of an ionization chamber or the sensitive volume of a solid state detector.

CSDA Continuous slowing down approximation refers to the electron range calculated from stopping power.

Field size The projection, on a plane perpendicular to the beam axis, of the distal end of the collimator as seen from the front centre of the source.

FF The Fill-Factor is the ratio of light-sensitive area to the pixel's total size.

Focal spot The focal spot is the size of the target area of an X-ray machine from which the X-rays are emitted.

Horns High-dose regions in the beam profile produced by the flattening filters which are designed to give a gradually increasing radial intensity.

IMRT Intensity-Modulated Radiation Therapy is a treatment technique that uses different directions with beams of nonuniform fluences, which have been optimized to deliver a high dose to the target volume while limiting the dose to the surrounding tissues to a minimum.

LCPE Lateral charged particle equilibrium is CPE in the lateral direction.

Penumbral region The region, at the edge of a radiation beam, over which the dose rate changes rapidly as a function of distance from the beam axis.

OF The output factor is defined as the ratio of dose per monitor unit at the depth of maximum dose d_{max} for a given field size to that for the reference field size.

PDD Percentage Depth Dose is the quotient, expressed as a percentage, of the absorbed dose at any depth d to the absorbed dose at a reference depth d_0

PTV The planning target volume is the volume that includes clinical target volume (CTV) with an internal margin (IM) as well as a set-up margin (SM) for patient movement and set-up uncertainties.

RMS Root mean square.

SAD Source-axis distance: distance from the radiation source to the isocentre.

SD Standard deviation.

SDD Source-detector distance: distance from the radiation source to the detector.

SRS Stereotactic radiosurgery.

SRT Stereotactic radiotherapy.

SSD Source-surface distance: distance from the radiation source to the surface of a water phantom.

Tails The tails of a dose beam profile is the low-dose part of the beam which extends to the sides.

TPR Tissue-phantom ratio is defined as the ratio of the dose at a given point in phantom to the dose at the same point at a fixed SDD and field size.

TPS Treatment planning system is a computerized system used in external beam radiotherapy that relies on beam and patient data acquisition to generate beam shapes and dose distributions with the intent to maximize tumour control and minimize normal tissue complications.

Bibliography

Ahuja, A. S., Dubuque, G. L. and Hendee, W. R. 1978. Output factors and scatter ratios for radiotherapy units. *Physics in Medicine and Biology*, 23, p. 968.

Alfonso, R., Andreo, P., Capote, R. *et al.* 2008. A new formalism for reference dosimetry of small and nonstandard fields. *Medical Physics Letter*, 35(11), pp. 5179–5186.

Al-Najjar, W. H., Guru Prasad, S., Parthasaradhi *et al.* 1998. Dosimetric aspects of small circular fields of 10 MV photon beam. *Medical Dosimetry*, 23, pp. 39–42.

Allinson N. *et al.* 2009. The Multidimensional integrated intelligent imaging project (MI-3). *Nuclear Instruments and Methods in Physics Research A*, 604(1-2), pp. 197–198.

Amako, K., Guatelli, S., Ivanchenko, V. *et al.* 2004. Validation of Geant4 electromagnetic physics versus protocol data. [online]. Available from: `http://www.ge.infn.it/geant4/papers/2004/nss2004/validation.pdf` [Accessed 15 December 2011].

Andreo, P. 1991. Monte Carlo techniques is medical radiation physics. *Physics in Medicine and Biology*, 36, pp. 861–920.

Andreo, P., and Brahme, A. 1986. Stopping power data for high energy photon beams. *Physics in Medicine and Biology*, 31, pp. 839–858.

Apostolakis, J. Bagulya, A., Elles *et al.* 2008. The performance of the Geant4 Standard EM package for LHC and other applications. *Journal of Physics: Conference Series*, 119(3), pp. 1–9 [online]. Available from: http://iopscience.iop.org/1742-6596/119/3/032004 [Accessed 14 March 2011].

Attix, F. H. 1983. Energy imparted, energy transferred and net energy transferred. *Physics in Medice and Biology*, 28(12), pp. 1385–1390.

Bai, Y., Bajaj, J., Beletic, J. W. 2008. Teledyne Imaging Sensors: silicon CMOS imaging technologies for x-ray, UV, visible, and near infrared. *Proceedings of the SPIE Conference on Astronomical Instrumentation*, 7021, 702102; doi:10.1117/12.792316.

Baldock, C., Murry, P., and Kron, T. 1999. Uncertainty analysis in polymer gel dosimetry. *Physics in Medice and Biology*, 44, pp. N243–N246.

Baldock, C., De Deene, Y., Doran, S. *et al.* 2010. Polymerer gel dosimetry. *Physics in Medicine and Biology*, 55, pp. R1–R63.

Beddar, A. S., Mason, D. J., and O'Brien, P. F. 1994. Absorbed dose perturbation caused by diodes for small field photon dosimetry. *Medical Physics*, 21, pp. 1075–1079.

Bedford, J.L., Childs,P. J., Nordmark Hansen, V. *et al.* 2003. Commissioning and quality assurance of the Pinnacle[3] radiotherapy treatment planning system for external beam photons. *The British Journal of Radiology*, 76, pp. 163–176.

Bellerive, M. R., Kooy, H. M., and Loeffler, J. S. 1998. Linac radiosurgery at the Joint Center for Radiation Therapy. *Medical Dosimetry*, 23(3), pp. 187–199.

Berger, M. J. 1963. Monte Carlo calculation of the penetration and diffusion of fast charged particles. In: B. Alder, S. Fernbach and M. Rotenberg (eds.), *Methods in Computational Physics*. New York: Academic.

Bigas, M., Cabruja, E., Forest, J. *et al.* 2006. Review of CMOS image sensors. *Microelectronic Journal*, 37, pp. 433–451.

Bielajew, A. F., and Rogers, D.W.O. 1986. Presta: The parameter reduced electron-step transport algorithm for electron monte carlo transport. *Nuclear Instruments and Methods in Physics Research Section B*, 18(1-6), pp. 165–181.

Blomgren, H., Lax, I. and Naslund, I. 1995. Stereotactic high dose fraction radiation therapy of extracranial tumors using an accelerator: Clinical experience of the first thirty-one patients. *Acta Oncologica*, 34, pp. 861–870.

Bohndiek S.E. 2008 Active Pixel Sensors for breast biopsy analysis using X-ray Diffraction. Thesis (PhD), University College London.

Brahme, A. 1984. Dosimetric precision requirements in radiation therapy. *Acta Radiologica Oncology*, 23, pp. 379–391.

Cabello J., Bailey A., Kitchen I., *et al.* 2007 Digital Autoradiography Using

Room Temperature CCD and CMOS Imaging Technology. *Physics in Medicine and Biology*, 52, pp. 4993-p5011.

Carlsson, G. A. 1981. Absorbed dose equations. On the derivations of a general absorbed dose equation and equations valid for different kinds of radiation equilibrium. *Radiation Research*, 85, pp. 219–237.

Carlsson, G. A. 1985. Absorbed dose and transport theory: comment on an absorbed dose equation in ICRU Report 35 on electron dosimetry. *Radiation Research*, 104, pp. 455–460.

Chen, Z. 2007. Principles and requirements of external beam dosimetry. *Radiation Measurements*, 41, pp. S2–S21.

Cirrone, G.A.P., Cuttonea, G., Di Rosaa, F. *et al.* 2010. Validation of the Geant4 electromagnetic photon cross-sections for elements and compounds. *Nuclear Instruments and Methods in Physics Research Section A: Accelerators, Spectrometers, Detectors and Associated Equipment*, 618(1–3), pp. 315–322.

Cortés-Giraldo, M. A., Quesada, J. M., Gallardo, M. I. *et al.* 14 December 2009. Geant4 interface to work with IAEA phase-space files. [online]. Available from: `http://www-nds.iaea.org/phsp/Geant4/G4IAEAphsp_HowTo.pdf` [Accessed 20 April 2011].

Crop, F., Reynaert, N., Pittomvils, G. *et al.* 2009. The influence of small field sizes, penumbra, spot size and measurement depth on perturbation factors for microionization chambers. *Physics in Medicine and Biology*, 54, pp. 2951–2969.

Das, I. J., Downes, M. B., Kassaee, A., and Tochner, Z. 2000. Choice of Radiation Detector in Dosimetry of Stereotactic Radiosurgery-Radiotherapy. *Journal of Radiosurgery*, 3(4), pp. 177–186.

Das, I. J., Ding G. X., and Ahnesjö, A. 2008 Small fields: nonequilibrium radiation dosimetry. *Medical Physics*, 35, pp. 206–215.

Dawson, D. J., Schroeder, N. J., and Hoya, J. D. 1986. Penumbral measurements in water for high-energy x-rays. *Medical Physics*, 13, pp. 101–104.

De Angelis, C., Onori, S., Pacilio, M. *et al.* 2002. An investigation of the operating characteristics of two PTW diamond detectors in photon and electrom beams. *Medical Physics*, 29, pp. 248–254.

De Deene, Y. 2004. Fundamentals of MRI measurements for gel dosimetry.

Journal of Physics: Conference Series, 3, pp. 87–114.

De Deene, Y., Hanselaer, P., De Wagter, C. *et al.* 2000. An investigation of the chemical stability of a monomer/polymer gel dosimeter. *Physics in Medicine and Biology*, 45, pp. 859–878.

Deptuch, G., Berst, J. D., Claus, G. *et al.* 2002. Design and testing of monolithic active pixel sensors for charged particle tracking. *IEEE Transactions on Nuclear Science*, 49, pp. 601–610.

Duggan, D. M. and Coffey, C. W. 1998. Small photon field dosimetry for stereotactic radiosurgery. *Medical Dosimetry*, 23(3), pp. 153–159.

Dutreix, J., and Dutreix, A. 1969. Film dosimetry of high-energy electrons. *Annals of the New York Academy of Sciences*, 161, pp. 33–43.

Eid, E. -S., Chan, T. Y., Fossurn, E. R., *et al.* 2001. Design and characterization of ionizing radiation-tolerant CMOS APS image sensors up to 30 Mrd (Si) total dose. *IEEE Transactions on Nuclear Science*, 48(6), pp. 1796–1806.

El Gamal, A., Fowler, B., Min, H. *et al.* 1998. Modeling and estimation of FPN components in CMOS image sensors. *Proc. SPIE*, 3301, pp. 168–177.

Engström, P. E., Haraldsson, P., Landberg, T. *et al.* 2005. In vivo dose verification of IMRT treated head and neck cancer patients. *Acta Oncologica*, 44, pp. 572–578.

Eklund, K., and Ahnesjö, A. 2010. Modeling silicon diode dose response factors for small photon fields. *Physics in Medicing and Biology*, 22(24), pp. 7411–7423.

Faddegon, B. A., Kawrakow, I., Kubyshin, Y. *et al.* L. 2009. The accuracy of EGSnrc, Geant4 and PENELOPE Monte Carlo systems for the simulation of electron scatter in external beam radiotherapy. *Physics in Medicine and Biology*, 54, pp. 6151–6163.

Fergional, H. M., Lambert, G. D., and Harrison, R. M. 1997. Automated TLD system for tumor dose estimation from exit dose measurements in external beam radiotherapy. *International Journal of Radiation Oncology: Biology, Physics*, 38, pp. 899–905.

Fernández-Varea, J. M., Mayol, R., Baró, J. *et al.* 1992. On the theory and simulation of multiple elastic scattering of electrons. *Nuclear Instruments and*

Methods in Physics Research, B73, pp. 447–473.

Flickinger, J., Kondziolka, D. and Lunsford, L. 1995. Radiosurgery of benign lesions. *Seminars in Radiation Oncology*,5, pp. 220–224.

Fossum, R. R. 1997. CMOS image sensors: electronic camera-on-a-chip. *IEEE Transactions on Electron Devices*, 44, pp. 1689–1698.

Fossum, R. R. 2003. Charge Transfer Noise and Lag in CMOS Active Pixel Sensors. Proceedings of 2003 IEEE Workshop on Charge-Coupled Devices and Advanced Image Sensors.

Fu, W., Dai, J. and Hu, Y. 2004. The influence of lateral electronic disequilibrium on the radiation treatment planning for lung cancer irradiation. *Bio-Medical Materials and Engineering*, 14, pp. 123–126.

García-Garduño, O. A., Lárraga-Gutiérrez, J., Rodríguez-Villafuerte, M. *et al.* 2009. Small photon beam measurements using radiochromic film and Monte Carlo simulations in a water phantom. *Radiotherapy and Oncology*, 96, pp. 250–253.

García-Vicente, F., Bejar, M., Pérez, L., and Torres, J. 2005. Clinical impact of the detector size effect in 3D-CRT. *Radiotherapy and Oncology*, 74, pp. 315–322.

García-Vicente, F., Delgado, J. M., and Rodríguez, C. 2000. Exact analytical solution of the convolution integral equation for a general profile fitting function and Gaussian detector kernel. *Physics in Medicine and Biology*, 45, pp. 645–650.

García-Vicente, F., Delgado, J. M., and Peraza, C. 1997. Experimental determination of the convolution kernel for the study of the spatial response of a detector. *Medical Physics*, 25(2), pp. 202–207.

Geant4 Collaboration. December 2010. Physics Reference Manual. [online] Available from: http://www.geant4.org/geant4/support/userdocuments.shtml [Accessed 14 March 2011].

Gibbs, F. A., Buechler, D., Leavitt, D. D. *et al.* 1992. Measurement of mechanical accuracy of isocenter in conventional linear-accelerator-based radiosurgery. *International Journal of Radiation Oncology: Biology, Physics*, 25, pp. 117–122.

González-Castaño, D., Pena, J., Sánchez-Doblado, F. *et al.* 2007. The change

of response of ionization chambers in the penumbra and transmission regions: impact for IMRT verification. *Medical and Biological Engineering and Computing*, 46, pp. 373–380.

Gore, J. C., Ranade, M., Maryanski, M. J. *et al.* 1996. Radiation dose distributions in three dimensions from tomographic optical density scanning of polymer gels: I. Development of an optical scanner. *Physics in Medicine and Biology*, 41, pp. 2695–2704.

Grusell, E., and Rikner, G. Evaluation of temperature effects in p-type silicon detectors. *Physics in Medicine and Biology*, 31, 527.

Haus, A. G. 2001. Advances in Film Processing Systems Technology and Quality Control in Medical Imaging. *Medical Physics*, 28, 1813.

Hedin, E. (emma.hedin@radfys.gu.se) 21 April 2011. "TPR(20/10)_10x10 - Your measured value compared to our simulated value." E-mail to F. Jimenez (fjimenez@medphys.ucl.ac.uk).

Hedin, E., Bäck, A., Swanpalmer, J. *et al.* 2010. [online] Available from: `http://www-nds.iaea.org/phsp/photon1/VarianClinaciX_6MV_PHSPdoc_Gothenburg.pdf` [accessed 20 April 2011].

Heydarian, A., Hoban, P., and Beddoe, A. 1996. A comparison of dosimetry techniques in stereotactic radiosurgery. *Physics in Medicine and Biology*, 41, pp. 93–110.

Higgins, P., Alaei, P., Gerbi, B. *et al.* 2003. In vivo diode dosimetry for routine quality assurance in IMRT. *Medical Physics*, 30, pp. 3118–3123.

Hoban, P. W., Heydarian, M., Beckham, W. A., and Beddoe, A. H. 1994. Dose rate dependence of a PTW diamond detector in the dosimetry of a 6 MV photon beam. *Physics in Medicine and Biology*, 39, pp. 1219–1229.

Horowitz, Y. S. 1981. The theoretical, and microdosimetric basis of thermoluminescence and applications to dosimetry. *Physics in Medicine and Biology*, 26(5), pp. 765.

Hussein, S., and Kennelly, G. M. 1996. Lung compensation in total body irradiation: A radiographic method. *Medical Physics*, 23, pp. 357–360.

International Atomic Energy Agency (IAEA). 2000. Absorbed dose determination in external beam radiotherapy. [online]. Code of practice for high energy

photon beams. TRS-398. Available from: `http://www-pub.iaea.org/mtcd/publications/pdf/trs398_scr.pdf` [Accessed 20 April 2011].

INDC International Nuclear Data Committee. January 2006. Phase-space database for external beam radiotherapy. [online]. Available from: http://www-nds.iaea.org/phsp/documents/indc-nds-0484.pdf [Accessed 20 April 2011].

International Comission on Radiaiton Units and Measurements. 1980. ICRU, Report No. 33: Radiation quantities and units. Washington, DC.

Janesick J 2007 *Photon Transfer DN → λ* (Washington: SPIE Press) p. 163.

Jensen, A., Brown, P., Pollock, B., *et al.* . 2005, Gamma knife radiosurgery of radiation-induced intracranial tumors: Local control, outcomes, and complications. *International Journal of Radiation Oncology, Biology, Physics*, 62, pp. 32-Ű37.

Jiménez, F. 2009. Monte Carlo simulation of a thin CMOS active pixel sensor. PhD transfer report, UCL.

Kalos, M. H., and Whitlock, P. A. 2008. Monte Carlo methods. Weinheim: Wiley-VCH Verlag GmbH & Co.

Kawrakow, I. 2000. Accurate condensed-history Monte Carlo simulation of electron transport: I. EGSnrc, the new EGS4 version. *Medical Physics*, 27, pp. 485–498.

Kleinfelder, S., Lim, S., Liu, X., and El Gamal, A. 2001. A 10000 Frames/s CMOS Digital Pixel Sensor. *IEEE JOURNAL OF SOLID-STATE CIRCUITS*, 36(12), pp. 2049–2059.

Kleinfelder, S., Bichsel, H., Bieser, F. *et al.* 2002. Integrated X-ray and charged particle active pixel CMOS sensor arrays using an epitaxial silicon sensitive region. [online]. Available from: http://repositories.cdlib.org/lbnl/LBNL-51417 [Accessed 20 April 2011].

Kleinfelder, S., Li, S., Bieser, F. *et al.* 2006. A proposed STAR microvertex detector using Active Pixel Sensors with some relevant studies on APS performance. *Nuclear Instruments and Methods in Physics Research A*, 565, pp. 132–138.

Khan F M 2003 *The Physics of Radiation Therapy* (Philadelphia: Lippincott Williams & Wilkins) p 387.

Knoll, G. F. 2000 Radiation Detection and Measurement. 3rd ed. John Wiley & Sons.

Kron, T. 1999. Applications of Thermoluminescence Dosimetry in Medicine. *Radiation Protection Dosimetry*, 85, pp. 333–340.

Larsen, E. W. 1992. A theoretical derivation of the Condensed History Algorithm. *Annals of Nuclear Energy*, 19 (10–12), pp. 701–714.

Laub, W. U., and Wong, T. 2003. The volume effect of detectors in the dosimetry of small fields used in IMRT. *Medical Physics*, 30, pp. 341–347.

Laub W. U., Kaulich T. and Nusslin F. 1999. A diamond detector in the dosimetry of high-energy electron and photon beams. *Physics in Medicine and Biology*, 44, pp. 2183–92.

Lewis, H. W. 1950. Multiple scattering in an infinite medium. *Physics Review*, 78, pp. 526–529.

Li, J. S., and Ma, C-M. 2008. A method to reduce the statistical uncertainty caused by high-energy cutoffs in Monte Carlo treatment planning. *Journal of Physics: Conference Series.* [online]. 102 (012015).

Loukianova, N., Folkerts, H. O., Maas, J. *et al.* 2003. Leakage Current Modeling of Test Structures for Characterization of Dark Current in CMOS Image Sensors. *IEEE Transactions on Electron Devices*, 50(1), pp. 77–83.

Lutz, W., Winston, K., and Maleki, N. 1988. A system for stereotactic radiosurgery with a linear accelerator. *International Journal of Radiation Oncology: Biology, Physics*, 14, pp. 373–381.

Magnan, P. 2003. Detection of visible photons in CCD and CMOS: A comparative view. *Nuclear Instruments and Methods in Physics Research A* 504, pp. 199-ï£¡212.

Martens, C., DeWagter, C., and DeNeve, W. 2000. The value of the PinPoint ion chamber for characterization of small field segments used in intensity-modulated radiation therapy. *Physics in Medicine and Biology*, 45, pp. 2519–2530.

Matis, H. S., Bieser, F., and Kleinfelder, S. *et al.* 2003. Charged Particle Detection using a CMOS Active Pixel Sensor. *Transactions on Nuclear Science*, 50(4), pp. 1020–1025.

McKerracher, C., and Thwaites, D. I. 1999. Assessment of new small-field detectors against standard-field detectors for practical stereotactic beam data acquisition. *Physics in Medicine and Biology*, 44, pp. 2143–2160.

Meigooni, A. S., Mishra, V., Panth, H. *et al.* 1995. Instrumentation and dosimeter-size artifacts in quantitative thermoluminescence dosimetry of low-dose fields. *Medical Physics*, 22, pp. 555–561.

Metcalfe, P. Kron, T., Elliott, A. *et al.* 1993. Dosimetry of 6-MV x-ray beam penumbra. *Medical Physics*, 20(5), pp. 1439–1445.

Muench, P. J., Meigooni, A. S., and Nath, R. 1991. Photon energy dependence of the sensitivity of radiochromic film and comparison with silver halide film and LiF TLDs used for brachytherapy dosimetry. *Medical Physics*, 18, pp. 769–775.

Nahum, A. E. 1996. Perturbation effects in dosimetry: Part I. Kilovoltage X-rays and electrons. *Physics in Medicine and Biology*, 41, pp. 1531–1580.

Niroomand-Rad, A., Blackwell, C. R., Coursey, B. M. *et al.* 1998. Radiochromic film dosimetry: Recommendations of AAPM Radiation Therapy Committee Task Group 55. *Medical Physics*, 25(11), pp. 2093–2115.

Pai, S. Das, I., Dempsey, J. F. *et al.* 2007. TG-69: Radiographic film for megavoltage beam dosimetry. *Medical Physics*, 34(6), pp. 2228–2258

Pappas, E., Maris, T. G., Zacharopoulou, F. *et al.* 2006. Experimental determination of the effect of detector size on profile measurements in narrow photon beams. *Medical Physics*, 33(10), pp. 3700–3710.

Pappas, E., Maris, T. G., Zacharopoulou, F. *et al.* 2008. Small SRS photon field profile dosimetry performed using a PinPoint air ion chamber, a diamond detector, a novel silicon-diode array (DOSI), and polymer gel dosimetry. Analysis and intercomparison. *Medical Physics*, 35(10), pp. 4640–4648.

Paskalev, K. A., Seuntjens, J. P., Patrocinio, H. J. *et al.* 2003. Physical aspects of dynamic stereotactic radiosurgery with very small photon beams (1.5 and 3 mm in diameter). *Medical Physics*, 30(2), pp. 111–117.

Pike, B., Podgorsak, E. B., Peters, T. M. *et al.* 1987. Dose distributions in dynamic stereotactic radiosurgery. *Medical Physics*, 14, pp. 780–789.

Podgorsak, E. B. ed. 2005. Radiation oncology physics: a handbook for

teachers and students. Vienna: IAEA publications.

Podgorsak, E. B., Oliver, A., Pla, M. *et al.* 1988. Dynamic stereotacric radiosurgery. *International Journal of Radiation Oncology*, 14, pp. 115–126.

Poon, E. and Verhaegen, F. 2005. Accuracy of the photon and electron physics in GEANT4 for radiotherapy applications. *Medical Physics*, 32 (6), pp. 1696–1711.

Poon, E., Seuntjens, J. and Verhaegen, F. 2005. Consistency test of the electron transport algorithm in the GEANT4 Monte Carlo code. *Physics in Medicine and Biology*, 50, pp. 681–694.

Ramani, R., Lightstone, A. W., Mason, D. L. D. *et al.* 1994. The use of radiochromic film in treatment verification of stereotactic radiosurgery. *Medical Physics*, 21, pp. 389–392.

Rao, P. R., Wang, X., and Theuwissen, A. J. P. 2008. Degradation of CMOS image sensors in deep-submicron thechnology due to γ-irradiation. *Solid-State Electronics*, 52, pp. 1407–1413.

Rice, K. R., Hansen, J. L., Svensson, G. K. *et al.* . 1987. Measurement of dose distribution in small beams of 6 MV x-rays. *Physics in Medicine and Biology*, 32, pp. 1097–1099.

Rogers, D. W. O. 1984. Low energy electron transport with EGS. *Nuclear Instruments and Methods in Physics Research*, 227, pp. 535–548.

Rogers, D. W. O., Faddegon, B. A., Ding, G. X. *et al.* 1995. BEAM: a Monte Carlo code to simulate radiotherapy treatment units. *Medical Physics*, 22, pp. 503–524.

Rogers, D. W. O. and Kawrakow, I. 2003. Monte Carlo calculated correction factors for primary standards of air kerma. *Medical Physics*, 30, pp. 521–543.

Roman, D. and Sperduto, P. 1995. Neuropsychological effects of cranial radiation: Current knowledge and future directions. *International Journal of Radiation Oncology, Biology, Physics*, 31, pp. 983-998.

Rosenfeld, A. B. 2007. Electronic dosimetry in radiation therapy. *Radiation Measurements*, 41, pp. S134–S153.

Ruden, B. I., and Bengtsson, L. G. 1977. Accuracy of megavolt radiation dosimetry using thermoluminescent lithium fluoride. *Acta Radiologica: Therapy,*

Physics, Biology, 16, pp. 157–176.

Salama, K., and El Gamal, A. 2003. Analysis of Active Pixel Sensor Readout Circuit. *IEEE Transactions on Circuits and Systems I: Fundamental Theory and Applications*, 50, pp. 941–944.

Salvat, F., Fernández-Varea, J. M. and Sempau, J. July 2006. PENELOPE-A Code System for Monte Carlo Simulation of Electron and Photon Transport. [online] Available from: `http://www.oecd-nea.org/science/pubs/2006/nea6222-penelope.pdf` [Accessed 11 March 2011].

Sánchez-Doblado, F., Andreo, P., Capote, R. *et al.* 2003. Ionization chamber dosimetry of small photon fields: a Monte Carlo study on stopping-power ratios for radiosurgery and IMRT beams. *Physics in Medicine and Biology*, 48, pp. 2081–2099.

Sauer, O. A., and Wilbert, J. 2007. Measurement of output factors for small photon beams. *Medical Physics*, 34(6), pp. 1983–1988.

Sauer, O. A., and Wilbert, J. 2009. Functional representation of tissue phantom ratios for photon fields. *Medical Physics*, 36(12), pp. 5444–5450.

Scott, A. J. D., Nahum, A. E., and Fenwick, J. D. 2008. Using a Monte Carlo model to predict dosimetric properties of small radiotherapy photon fields. *Medical Physics*, 35(10), pp. 4671–4684.

Sempau, J., Acosta, E., Baró, J. *et al.* 1997. An algorithm for Monte Carlo simulation of coupled electron-photon transport. *Nuclear Instruments Methods B*, 132, pp. 377–390.

Sham, E., Seuntjens, J., Devic, S. *et al.* 2008. Influence of focal spot on characteristics of very small diameter radiosurgical beams. *Medical Physics*, 35(7), pp. 3317–3330.

Shcherback, I., Belenky, A. and Yadid-Pecht, O. 2002. Empirical dark current modeling for complementary metal oxide semiconductor active pixel sensor. *Optical Emgineering*, 41(6), pp. 1216–1219.

Sibata, C. H., Mota, H. C., Beddar, A. S. *et al.* 1991. Influence of detector size in photon beam profile measurements. *Physics in Medicine and Biology*, 36(5), pp. 621–631.

Sims, E., Doughty, D., Macaulay, E. *et al.* 1999. Stereotactically delivered

cranial radiation therapy: a ten-year experience of linac-based radiosurgery in the UK. *Clinical Oncology*, 11, pp. 303–320.

Taylor, M. L., Kron, T., and Franich, R. D. 2011. A contemporary review of stereotactic radiotherapy: Inherent dosimetric complexities and the potential for detriment. *Acta Oncologica*, Review Article.

TG-42. 1995. American Association of Physicists in Medicine Radiation Therapy Committee Report No. 54. Stereotactic Radiosurgery (AIP, Woodbury, NY).

Tian, H., Fowler, B., and El Gamal, A. 2001. Analysis of temporal noise in CMOS photodiode active pixel sensor. *IEEE Journal of Solid-State Circuits*, 36(1), pp. 92–101.

Tsai, J.-S., Wazer, D. E., Ling, M. N. *et al.* 1998. Dosimetric verification of the dynamic intensity-modulated radiation therapy of 92 patients. *International Journal of Radiation Oncology: Biology, Physics*, 40, pp. 1213–1230.

Turchetta, R., Berst, J. D., Casadei, B. *et al.* 2001. A monolithic active pixel sensor for charged particle tracking and imaging using standard VLSI CMOS technology. *Nuclear Instruments and Methods in Physics Research Section A*, 458, pp. 677–689.

Turchetta, R., French, M., Manolopoulos, S. *et al.* 2003. Monolithic active pixel sensors (MAPS) in a VLSI CMOS technology. *Nuclear Instruments and Methods in Physics Research A*, 501, pp. 251–259.

Urgošík, D., Vymazal, J., Vladyka, V. *et al.* 2000. Treatment of postherpetic trigeminal neuralgia with the Leksell gamma knife. *Journal of radiosurgery*, 93(3), pp. 165–168.

Verhaegen, F., Das, I., and Palmans, H. 1998. Monte Carlo dosimetry study of a 6 MV stereotactic unit. *Physics in Medicine and Biology*, 43, pp. 2755–2768.

Wang, L. L. W., and Leszczynski, K. 2007a. Estimation of the focal spot size and shape for a medical linear accelerator by Monte Carlo simulation. *Medical Physics*, 34, pp. 485–488.

Wang, L. L. W., and Rogers, D. W. O. 2007b. Monte Carlo study of Si diode response in electron beams. *Medical Physics*, 34(5), pp. 1734–1742.

Weaver, R. D., Berbi, B. J., and Dusenbery, K. E. 1995. Evaluation of dose

variation during total skin electron irradiation using thermoluminescent dosimeters. *International Journal of Radiation Oncology: Biology, Physics*, 33, pp. 475–478.

Williamson, J., Khan, F. M., and Sharma, S. S. 1981. Film dosimetry of megavoltage photon beam: a practical method of isodensity-to-isodose curve conversion. *Medical Physics*, 8, pp. 94–98.

Wilkins, D., Li, X., Cygler, J. *et al.* 1997. The effect of dose rate dependence of p-type silicon detectors on linac relative dosimetry. *Medical Physics*, 24, pp. 879–881.

Wong, C. J., Ackerly, T., He, C., Patterson, W. *et al.* 2009. Small field size dose-profile measurements using gel dosimeters, gafchromic films and micro-thermoluminescent dosimeters. *Radiaton Measurements*, 44, pp. 249–256.

Yin, FF. 1995. Physical penumbra change of beam profile due to film digitization. *Medical Physics*, 22(6), pp. :803–805.

Yu, C., and Luxton, G. 1999. TLD dose measurement: A simplified accurate technique for the dose range from 0.5 cGy to 1000 cGy. *Medical Physics*, 26(6), pp. 1010–1016.

Zhu, T. C. 2010. Small Field: dosimetry in electron disequilibrium region. *Journal of Physics: Conference Series 250 012056.*